Design and Synthesis of Covalent Organic Frameworks for Carbon Dioxide Capture

Zhai Lipeng

Doctor of Philosophy

Department of Structural Molecular Science
School of Physical Sciences
SOKENDAI (The Graduate University for Advanced Studies)

June 2017

Table of Contents

Chapter 1

General Introduction

1.1 Covalent Organic Frameworks

The field of nanoporous materials has grown quickly in the last several decades. This is because nanoprous materials have outstanding properties and widely applications. The applications are as following: catalyst, gas storage and separation, super-hydrophobic interfaces, optoelectronics, energy storage and conversion, semiconductors and photovoltaics.[1,2] Even though organic researcher workers have found different synthetic method to construct a widely porous materials, the reported research works demonstrated that it is difficult to form organic polymer frameworks with unique pore channels before the reticular chemistry emerges. Reticular Chemistry, which uses strong covalent organic bonds to linked molecular building blocks for constructing crystalline frameworks, has significantly broadened the family of useful materials and chemical compounds.

Typically, metal-organic frameworks (MOFs) were synthesised from metal-containing groups and organic building units, which was the first family of porous materials formed via reticular chemistry.[3] Through changing the combination of available metal ions and organic building blocks, which can create variety possibilities with desired framework composition and structure. Topology design principle was used to form porous polymer frameworks with strong covalent organic bonds. This case was the first successful instance for the filed of covalent organic frameworks (COFs).[4] COFs, materials that is new crystalline porous materials. COFs materials, whose atoms of frameworks could be precisely designed into building blocks with periodicity. COFs materials have developed as a novel platform, which advanced organic materials could be designed with periodic structures. Using reticular chemistry, structures and skeleton of COFs materials can be predesigned and experimentally synthesized through reversible condensation reactions. Since this landmark paper, great progresses have been achieved in the chemical synthesis of COFs. Moreover, COFs exhibited potential applications for functional exploration such as catalyst, gas molecules storage, optoelectronics, semiconductors, photovoltaics and sensors.[5]

COFs materials are constructed with organic building units to obtain two- and three-dimensional crystalline open organic frameworks with frameworks structures. Light elements (B, C, N, O, H) were introduced into the frameworks through strong organic chemical bonds. Thus, COFs materials have robust architectures with highly porosity and thermal and chemical stability in the atmosphere. To date, COFs materials could be divided into three- (3D) or two-dimensional (2D) COFs materials according to the building blocks dimension.[6] Layered eclipsed structure was formed through 2D COFs material stacking. Periodically aligned columns were found within 2D COFs materials. The aligned columns are hard to be built with traditional noncovalent or covalent approaches. Moreover, due to variety of available building blocks, 2D COFs can be easily designed and synthesised for different functional applications. Unlike 2D COFs, 3D COFs materials extend this framework into three-dimensional via building blocks design with an sp^3 carbon or nitrogen or silane atom in the frameworks. Compared with 2D COFs, 3D COFs usually possess high specific surface areas (4210 $m^2 g^{-1}$), low densities (0.17 g cm^{-3}) and widely open sites. These unique properties make 2D and 3D COFs materials as ideal candidates for gas storage and separation.[7] In this chapter, I focused on COFs materials' design and formation, skeletons, pore structures, and functional explorations of this emerging material.

1.1.1 Design and Synthesis

1.1.1.1 Reversible chemistry

Generally, reactions with kinetically-controlled play an essential role in making porous materials. The formed covalent bonds during these reactions are irreversible. In addition, using irreversible reaction is difficult to obtain crystalline organic polymers. On the contrary, dynamic covalent chemistry (DCC) was used to form covalent organic bonds reversibly. During this process, covalent organic bonds can be formed, broken, and reparied.[8] It is different from traditional covalent organic bonds' construction. DCC chemistry method is controllable thermodynamically. Reversible reaction including "proof-reading" and "error checking" properties was offered. As a result, this method could construct the thermodynamically stable materials structures.

DCC method was used to form COFs materials; the skeleton of COFs materials could be formed with crystallization process. At the same time, the incidence of structural defects could be reduced by self-healing feedback. Also self-healing feedback could promote the formation of COFs materials with long ordered structure. Therefore, the final COFs products possess the ordered crystalline structures with the highest thermodynamic stability.

Two key factors must be taken into account for COFs materials. These issues should achieve controllable thermodynamic reaction in reversible reactions. The building blocks' structure is the first factor; Synthetic method such as the reaction media and reaction conditions (temperature and pressure) is the last factor.

1.1.1.2 Building Blocks

In order to build crystalline COFs materials, two requirements of the building blocks' structure should be taken into consideration. 1) a reversible reaction should be used for the COFs materials formation; 2) building units' geometry should be kept properly within COFs materials.[6] As for the first requirement, the building units should have reactive functional groups. These reaction functional groups could be

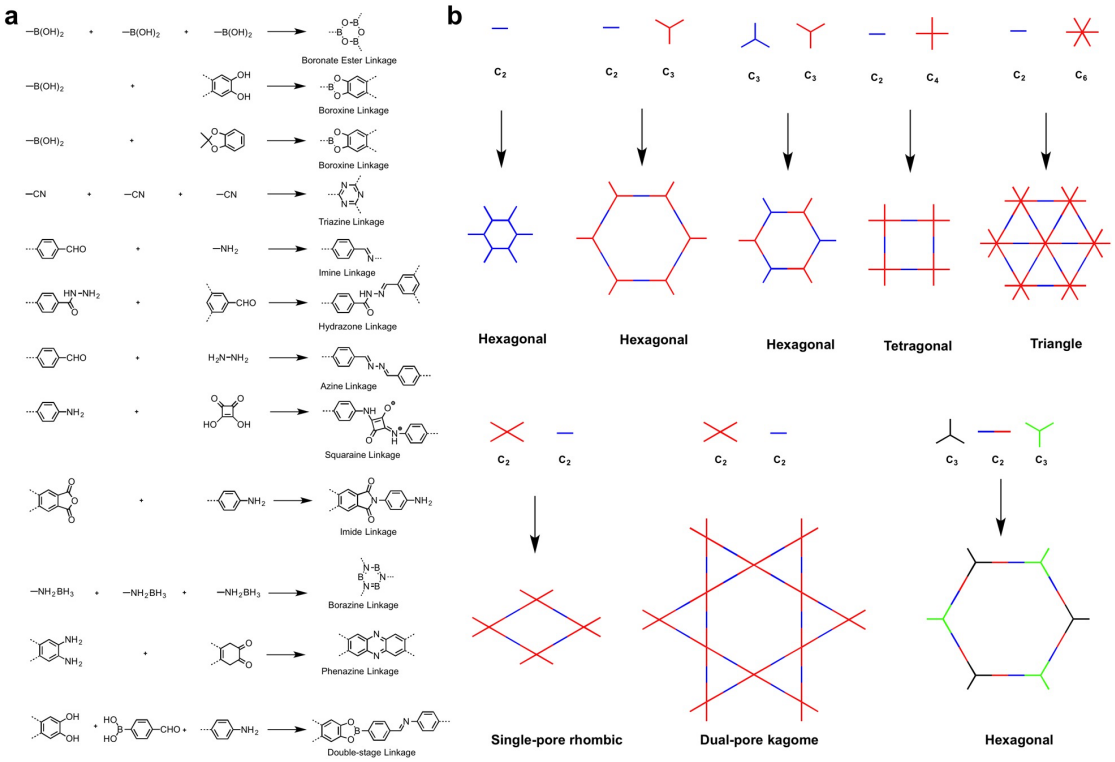

Figure 1. a) The dynamic chemical reactions for preparing COFs. **b)** 2D COFs' design principle.

covalent organic bond formation with dynamic condition as following: 1) without irreversible side reactions existing within the COFs' formation process. And *2*) only monomers, oligomers exist in the COFs materials synthetic system under thermodynamic control reaction. When it refers the second requirement, the organic building units ought to be structure with rigid. The covalent bonds' formation should be unique in this reaction system. To date, widely reversible reactions have been developed to meet the first successful COFs synthesis's requirement (Figure 1a). Majority of the reported COFs materials were constructed based on boron chemistry, imine chemistry, and azine chemistry. Boronic acids could be self-condensed and polycondensed with dialcohols. These reactions could be used to consturct COFs materials with boroxine linked (PPy-COF) and boronate ester linked COFs (TP-COF) (Figure 2).

Acetonide-protected catechols not dialcohols could be reacted with boronic acids using Lewis acid $BF_3{\cdot}OEt_2$ as catalyst to form COFs materials (Figure 1a). The *in-situ organic* deprotection principle offers a practical strategy. This strategy could avoid the monomer oxidation issue. Also the monomer solubility problems within the

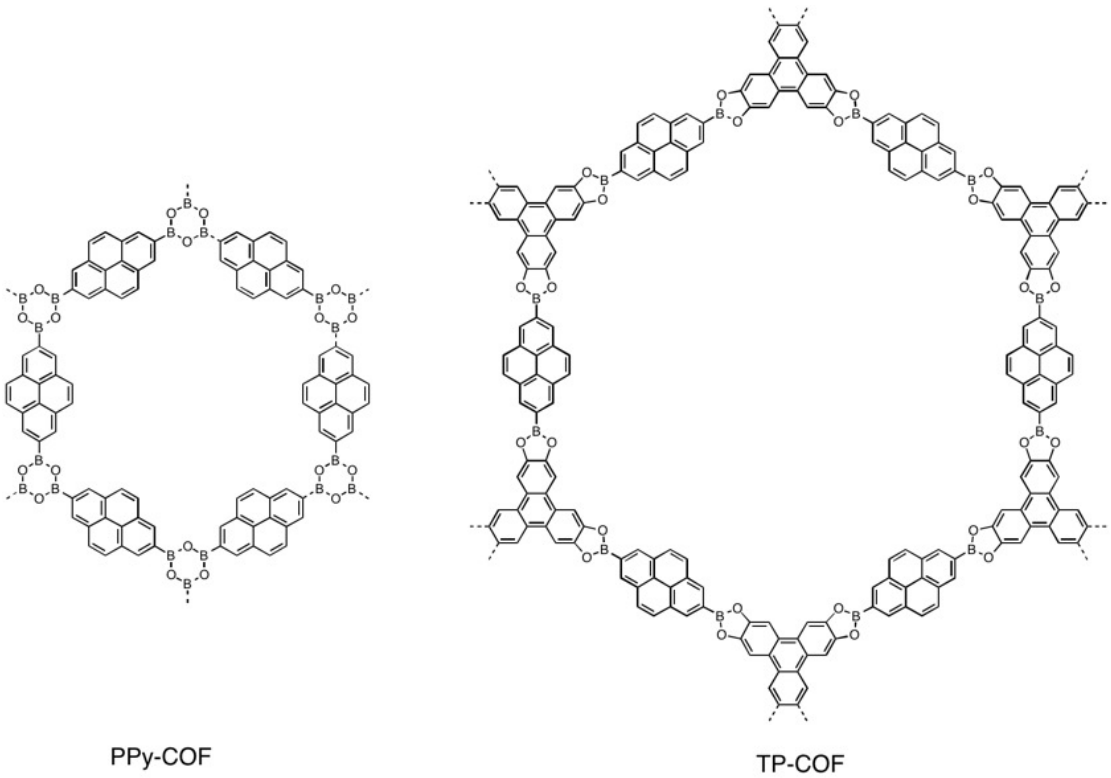

Figure 2. Boronate ester linked COFs

organic building units could be avoided. Borosilicate linkage has the similar property with the boroxine and boronate esters' reaction system. Borosilicate linkage also has been applied to syntehsis COFs materials. Borosilicate linked COFs materials were formed with tetraboronic acid and tert-butylsilanetriol polycondensation (Figure 1a).[9]

Although boron-based COFs materials are usually thermally robust and they are susceptible to be attacked and are even hydrolysed by water vapours toward air atomsphere.[10] As a consequence, novel connection chemistries of COFs materials was explored by Yaghi's group. Dynamic pH-control, reversible polycondensation that form imine[11,12] and hydrazone linkage[13] have been developed. Especially, compared with boron-based COFs, imine-linked COFs exhibited better chemical stability toward water and organic solvent and thermal stability. Our group explored another class of COFs based on azine linkage via hydrazine with rigid aldehyde monomers in 2013 (Figure 3).[14] In 2008, via the cyano groups' trimerization under ionothermal conditions, covalent triazine-based frameworks (CTFs) were formed (Figure 3).[15,16] A high degree of conjugation skeleton with high chemical, thermal, and mechanical stabilities could be obtained for CTFs materials. These properties are different from COFs materials; however, typically, they have poor crystallinity because of the bad reversibility of this trimerization reaction.

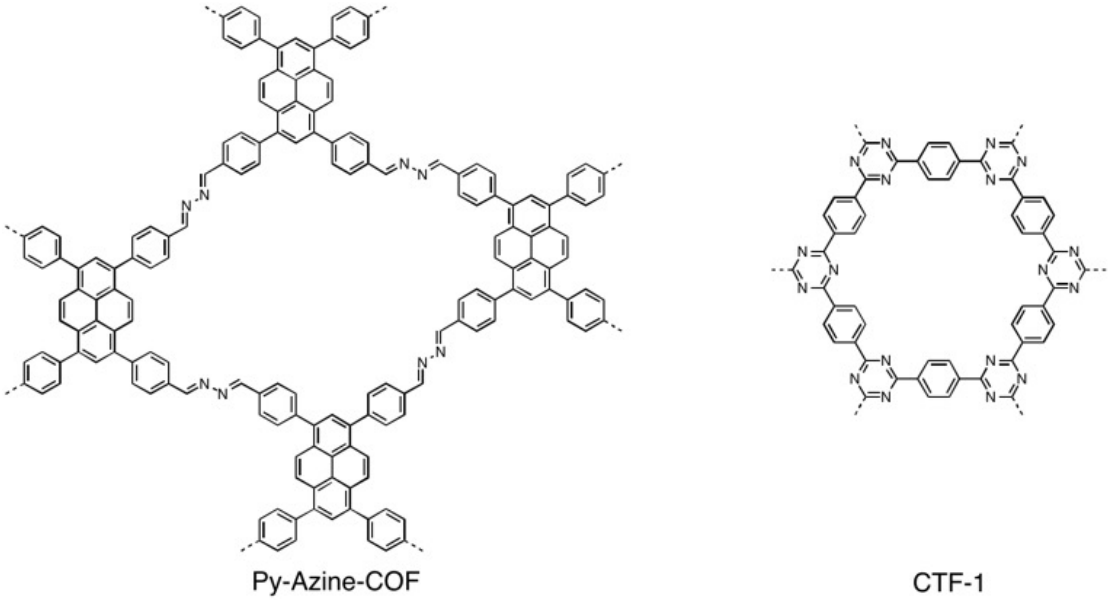

Figure 3. Azine and triazine linked COFs

1.1.2 Structural Study

X-ray diffraction (XRD) patterns are the distinct property for highly crystalline polymers COFs. PXRD data could be used for the simulation of 2D and 3D COFs' crystalline structure. The COFs materials' theoretical simulation method provides an essential way in exhibiting COFs materials' stacking structures. Moreover, COFs' linkages, terminal functional groups, and compositions were evaluated by widely methods.

1.1.2.1 Structure of 2D COFs

1.1.2.1.1 Topology

Extended frameworks with tetragonal and hexagonal topologies could be produced within 2D COFs materials through the organic building units' polycondensation (Figure 1b). 2D COFs with hexagonal topology have been constructed via combining the C_2 or C_3 blocks with either 2D-C_3 building blocks. Hexagonal COFs could be formed with the C_2 or C_3 building blocks' self-condensation. The hexagonal COFs' structure is an **hca** type framework. According to 2D layers' different stacking, its framework has two main exiting forms mode. The **bnn** topology alngside frameworks' lattice, which is first one. However, the COFs' layer structures stacked layer by layer. The **gra** framework that stacks layers is the second case. In this case the layer stack to each other with a half unit cell. Moreover, COFs materials with tetragonal topology have been formed through using C_4 blocks with either C_2 or C_4 organic blocks units. These 2D COFs with tetragonal

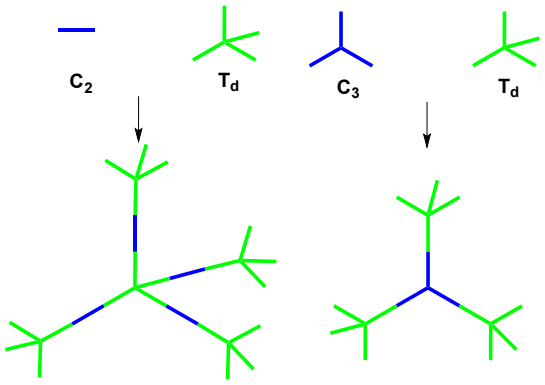

Figure 4. Different building blocks' geometries to design 3D COFs

topology (an **scu** network) using the C_4 building blocks as the vertices. The C_2 units were applied as the frameworks' edges.

1.1.2.1.2 Structure of 3D COFs

Secondary building blocks' geometry and their connection ways control the 3D COFs' topology excepting the organic building block used for 3D-T_d geometric structure, (Figure 4). Joining triangular (2D-C_3) and tetrahedral (3D-T_d) nodes can give two different networks analogue to **bor.** Yaghi have showed that tetrahedral monomer tetra(4-dihydroxyborylphenyl)methane's (TBPM) self-condensation and its' silane analog (TBPS) induce to **ctn** COFs (COF-103 and COF-102). However, polycondensation of triangular monomer HHTP with TBPM or TBPS induced into two totally different nets, **ctn** type (COF-105) and **bor** type (COF-108).[7] However, The reason that determines one structure type would be preferred over the other one was still remains unclear. Compared with ctn type, **Bor** type has 15% less dense and larger pores. This is interesting and notable differences. In addition, by connecting T_d symmetry monomers using C_2 linkers would lead to the formation of **dia** network. Schiff-based COF-300 is the representative of **dia** topology with a multiply interpenetrated structure.[11]

To date, the 3D imine-linked COF-300 has the smallest pore size (0.8 nm). Boronate ester-linked COF-108 has a largest diameter of 3.1 nm. Nitrogen sorption isotherm at 77K was used to check the BET surface area of COFs materials. The lowest COFs materials' BET are 1360 for COF-300. The highest one is 4210 $m^2 g^{-1}$ for COF-103. A synthetic strategy was used to functionalize the 3D COFs' pore channel. They used truncated trigonal organic building units as substrates to lock different functional organic functional groups. These groups like alkyl and allyl chains induced into COFs' pore channels.[17] Even the 3D COFs materials have high truncated building blocks loading levels. However, the original 3D COFs materials' crystallinity and porosity could be kept. Because limitation of thermodynamic construction of COFs materials were highlight. Therefore, this method is essential and interesting.

1.1.2.1.3 Layers' alignment

2D COFs materials' planar structures could be stacked to form layer and layer structures. 2D COFs materials are extended planar and have parallel-layered structures indicted by STEM.[18,19]. Using XRD analysis method to simulate the layers' alignment in tetragonal and hexagonal topology frameworks networks is still remaining difficult for scientists. Using energy optimization to build the single layer structure and layered networks is a powerful way to analysing the layer structure *ab initio* methodology. The layers' distance and horizontal offset could be predicted. This offers insights the 2D COF layers' unique structures between layers.

2D COFs stacking energy lattices were calculated with DFT-B. Similar PXRD curves were predicted for this lattice type. The observed patterns are same with calculated mode. However, according to the offsets, the COFs' stacking energies are different from the calculated energy. COFs with AB stacking structures have the lower energy compared with COFs with AA stacking structures. The offset values' difference could produce a profile for the offset distance and formation energy. As a result, the highest stability was found within COFs' layered structure with slight offset. In the armchair and zigzag directions, layers' distance of 1.4 Å is most preferred. Therefore, AA stacking has the more attractive Coulomb interlayer interactions compared with AA stacking. Therefore, lower stacking energy could stabilize COFs materials to some extent. Recently, molecular mechanisms was applied to define the offset between HHTP-DPB COFs' layers.[7] With DFT methods, offset between 1.7-1.8 Å was found within the HHTP-DPB COF' adjacent layers.

According to above calculation results, COFs materials' structure calculation according to the PXRD curves was performed. Also, the corresponding PXRD pattern was predicted with each space group's unit cell. The calculated and experimentally observed PXRD patterns' difference was used to determine each space group' suitability. Commonly, the AB stacking mode yielded XRD pattern via, which is widely different compared with experimental PXRD curve. Therefore, the result obviously excludes AB stacking possibility in 2D COFs materials. However, similar XRD patterns could be produced with AA stacking or slightly slipped AA stacking

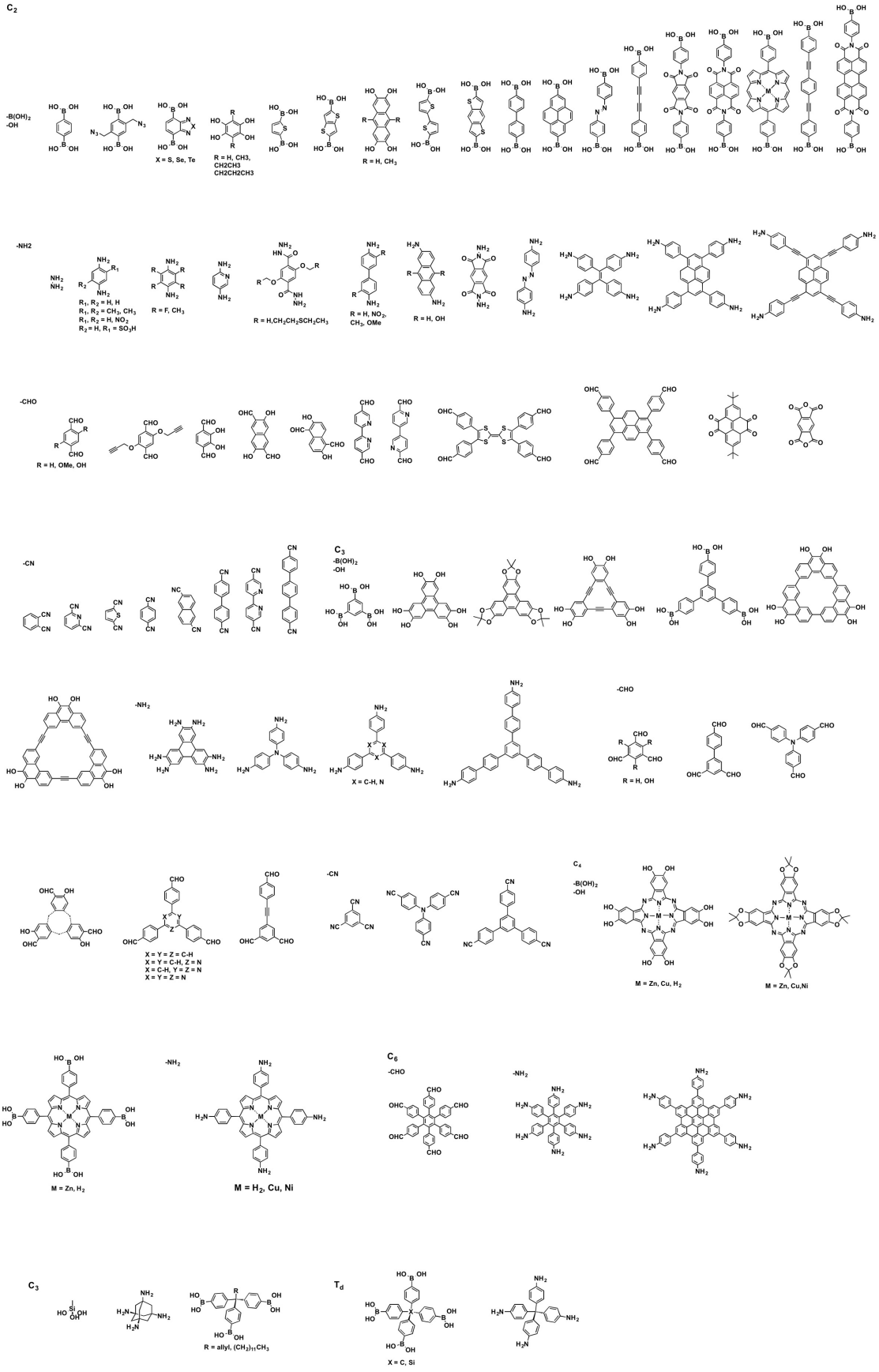

Figure 5. Typical building blocks used to form boron-, imine-, hydrazone-, azine-, squaraine- and phenazine-linked COFs.

modes. Moreover, no obvious differences were observed in the simulated XRD patterns unless they have different stacking energies.

1.1.3 Synthetic Method

During covalent bond formation, thermodynamic equilibrium is important to construct covalent frameworks with highly orders. Especially, the reaction conditions (temperature and pressure) should be considered to synthesis porous crystalline frameworks with thermodynamically stable structures. For COFs' synthesis, different solvent mixtures were developed as solvothermal commonly. Also, to quickly synthesize COFs, microwave reactions method were used to form COFs materials. Substrates (metal surfaces) have been developed for preparing COF monolayers or films, which is different from bulky synthesis methods.

1.1.3.1 Solvothermal Synthesis

Since Yaghi and coworkers used solvothermal synthesis method to prepare the fist COF, this method was employed for construction of most COFs.[20-22] Solvothermal synthesis is defined as when a 10-cm^3 pyrex tube was added with different monomers and solvents and removed oxygen with freeze-pump-thaw. COFs' growth will happen after sealing the tube and this process usually takes about 3 to 7 days and requires heating between 85-150 ^oC. In addition, the solvent selected for COFs synthesis is essential since the solvent would affect the solubility of reactant, reaction rate, self-healing, crystal nucleation and growth rate during the condensation reaction.

Generally, the good solvent and poor solvent are used together as mixed solvent with different ratios to prepare highly crystalline COFs. Good solvents such as DMAc THF, dioxane, o-dichlorobenzene were used to synthesis COFs. For the poor solvent, mesitylene, butanol, methanol and toluene have been used to prepare COFs. For example, our group reported that using monomer (2,3,9,10,16,17,23,24-Octahydroxyphthalocyaninato)nickel(II) ($(OH)_8NiPc$) and 1,4-benzene diboronic acid with a mixture of dioxane and mesitylene as solvent to synthesis amorphous materials. While highly crystalline COF could be formed when the mixed solvent of DMAc and o-dichlorobenzene (v/v=2:1) used as the reaction

solvent.[23] Therefore, a choice of solvent is essential and necessary for synthesis COFs with highly crystalline.

1.1.3.2 Microwave Synthesis

Owing to accelerated reaction times, high yields and cleaner products, microwave reaction is popular for organic chemistry.[24] Recently, Cooper ad coworkers firstly introduced microwave reaction to synthesis COFs.[25] According to their research, microwave synthesis has some inherent merits compared with solvothermal synthesis. First, this method provide a fast way to produce COFs as this method is 200 times faster than solvothermal synthesis in their case. Furthermore, the porosity of COF obtained is better than solvothermal synthesis. Hence, microwave synthesis offers a possibility for production and application of COFs in large scale.

1.1.3.3 Ionothermal Synthesis

Ionothermal synthesis was firstly employed to prepare CTFs by Thomas and coworkers in 2008.[15] To date, many cases of CTFs was synthesized through this method. The cyclotrimerization of aromatic building blocks usually happens in molten $ZnCl_2$ at a temperature higher than 400 ^{o}C to obtain crystalline CTFs. In this reaction system, the molten $ZnCl_2$ were used as solvent and catalyst as well for the partially reversible trimerization chemical reaction. The harsh reaction condition limit this method's further application in synthesis crystalline CTFs.

1.1.3.4 Mechanochemical synthesis

Recently, mechanochmesitry (MC) has been employed to prepare various organic and inorganic transformations and construction of metal-organic frameworks. Rahul and co-workers have applied this method to constructed a series of thermally and chemically stable COFs materials.[26] Compared with solvothermal synthesis method, MC synthesis method provided several advantages such as solvent-free, rapid and room temperature synthesis. However, using MC synthesis method to prepare COFs is still a challenge since COFs crystallization basically requires reversibility.

1.1.3.5 Surface-supported synthesis

COFs are typically obtained as powders through solvothermal synthesis and are difficult to be fabricated into films for practical devices. Herein, using substrate to prepare COF thin films attract wide scientific interest and have a technological importance. In addition, growing thin COFs films with certain film thickness, crystalline, and morphology is highly necessary for the further diverse applications. Recently, many groups attempted to grow COF films on different substrates and have already yielded promising results.

Single layer grapheme (SLG) was exploited to produce COF-5 thin films. X-ray diffraction analysis was used to investigate the higher crystallinity of films than powder samples.[27] The thickness is 195 ± 20 nm, which was determined by scanning electron microscopy (SEM) (Figure 6). Also, Some researchers prepared COF monolayers on a metal surface such as Ag (111), Ag (100) and Au (111), which were observed by scanning tunneling microscopy (STM). The STM confirmed that a series of pores exist on the metal surface. Thomas and coworkers employed vapor-assisted conversion to synthesis different 2D COF films with different thickness. On glass substrates, this thickness increases from a few hundred nanometres to several microns. This method provides a powerful method to utilization of COF films in diverse applications. Although surface-supported synthesis has been proved to be an efficient approach toward COF materials, scalability, morphology and yield still remain a foremost challenge for scientists.

1.1.4 Channel structure

2D COFs materials constitute one dimensional pore channels and their pore size is mainly relied on the building blocks' length and topology skeleton design. In the past decades, a variety of pore size in COFs system ranging from micropore to mesoporous was developed for different applications. In addition, post-synthetic modification of pore channels for COFs systems provide an effective way to introduce functional groups within COFs' topology. The structure and environment of pores could be modified. All these methods have been proved to be powerful strategy for designing COFs materials with special applications.

For COFs in two dimensions, microporous COF-1 has smallest pore size around 0.86 nm via BPDA's self-condensation.[4] On the other hand, mesoporous HHTP-DPB COF has the largest pore size around 4.7 nm. Monomer HHTP and monomer 4,4'-diphenylbutadiynebis(boronic acid) were used to form (DPB) HHTP-DPB COF.[7] Moreover, COFs materials with different pore size ranging from micropore 0.86 nm to mesopore 4.7 nm via tuning the size of building blocks.[7,28-30] In addition, the highest BET surface area for 2D COFs is TpBD-Me_2 with 3109 m^2 g^{-1} and the pore size for this COF is 2.3 nm. According to the results, there is no direct relationship between BET and pore size.

In order to improve COF-18 Å' stability toward water or air, alkyl chain substituted organic building blocks were used to synthesis COFs with boronate ester linkage.[31] Through alkyl chains' changing into the pore channels, COF-18 Å has a pore size of 1.8nm. The pore size of COF-16 Å is 1.6nm. The diameter of COF-14 Å is 1.4nm. COF-11 Å has a pore size of 1.1nm (Figure 7). As a consequence, after introducing different chain length, the S_{BET} changed between 1263 and 105 m^2 g^{-1}. These results demonstrated that pore channels' microenvironment could be changed by incorporating the alkyl chains within the of COFs materials. Therefore, this method could enhance gas adsorption properties and stability.

In 2011, our group used a simple strategy to functionalize 2D COFs' pore and introduce different functional groups into the pore surface (Figure 8).[32] Using organic

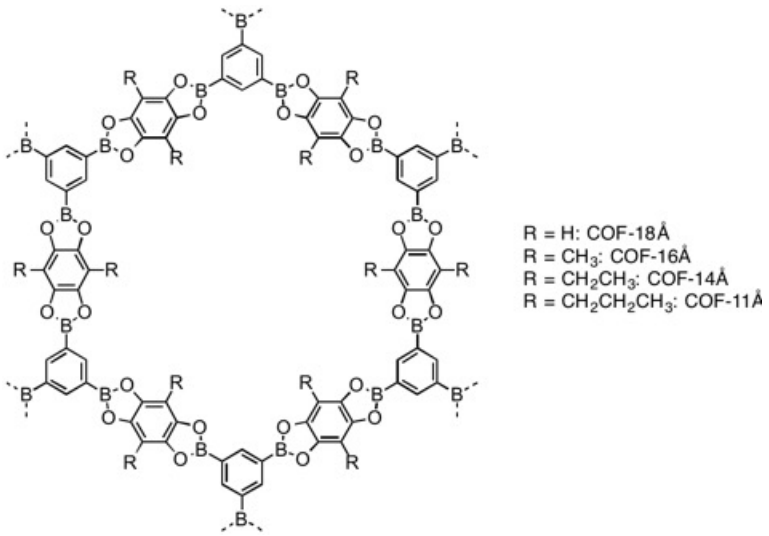

Figure 7. COFs with different alkyl chains within pore channel

building blocks with azide group to form COFs materials. In this respect, the anchored content of azide units could be designed. Via click reaction, these azide units could react with differential alkynes groups. Preferred densities or desired groups could be introduces in pore channels. Moreover, the crystallinity and porosity of COF-5 could be kept after introducing different functional groups. In 2015, our group developed a powerful strategy to introducing different polar functional groups through ring-opening reaction and click reaction, which have strong interaction with CO_2 gas molecule. These methods convert the COFs materials into outstanding materials for CO_2 capture and separation. Also, the tailor-made pore channel surface showed a powerful way to introduce desired compositions, components, and functionalities into COFs' skeleton.

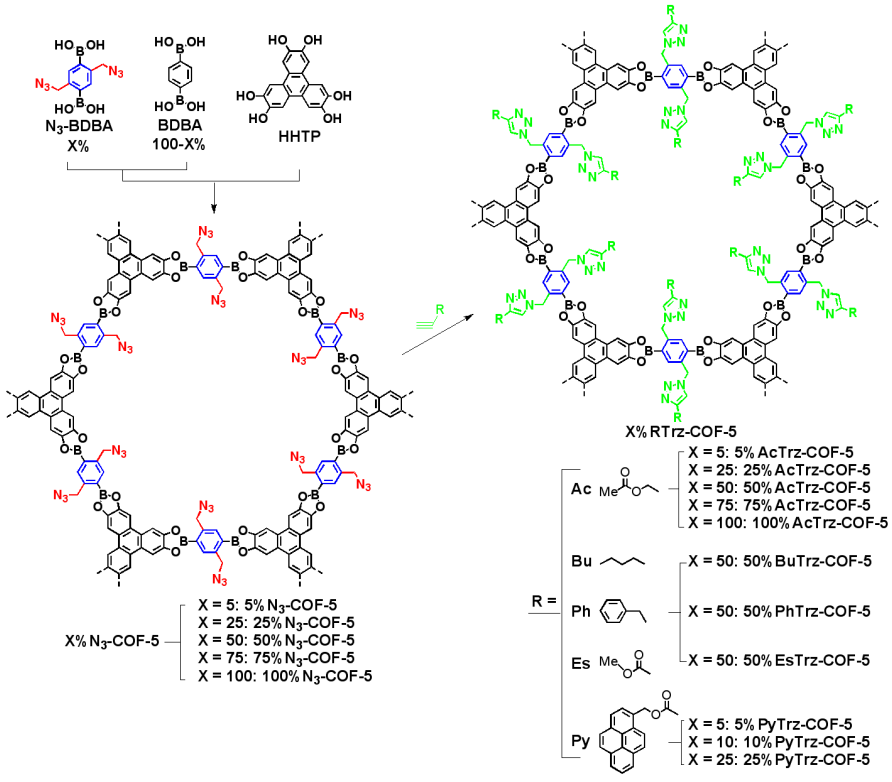

Figure 8. Surface engineering of hexagonal COF-5

1.1.5 Function Exploration

COFs' function is clear related with building units, porosity, and pore channel environment. Via building blocks design such as introducing chiral building blocks into COFs skeleton or coordinating metal nanoparticles into the COFs skeleton, COFs

showed potential application in wide field. COFs materials have columnar arrays throughout their building blocks, which traditional supramolecular and conventional porous material methods do not have. Therefore, COFs materials is attractive in semiconducting and photoconducting filed. As aforementioned advantages of COFs materials, COFs showed unique advantage within gas molecule capture and separation field over last decades.

1.1.5.1 Heterogeneous Catalysis

Asymmetric catalysis is quite essential for chemical transformations since it provide a straightforward method to synthesis a variety of chiral intermediates and medicines. Heterogeneous asymmetric catalysts always showed easy separation from the reaction systems and outstanding cycle performance, which play a unique role in chemical process. In 2015, our group developed a robust catalytic system since the chemical stability of COFs is critical for catalytic system.[33] In this respect, incorporating methoxy groups to the phenyl linker of the imine bonds trigger resonance effects that soften the C=N bonds' polarization. Methoxy groups could reduce the charge repulsions between the layers as well. The resulting TPB-DMTP-COF has high porosity (S_{BET} = 2105 m^2 g^{-1}) with pore size 3.26 nm. In addition, TPB-DMTP-COF exhibited outstanding stability in organic solvents and strong acid and base. Based on this stable skeleton structure, a series of chiral [(S)-Py]x-TPB-DMTP-COFs (Figure 9) were constructed via the integration of chiral pyrrolidine units onto the pore walls pore using click reaction. The functionalize [(S)-Pyr]x-TPB-DMTP-COFs could keep their crystallinity, porosity, and chemical stability after introducing the chiral catalytic sites, which enable the chiral COFs with exceptional activity in the heterogeneous catalysis of asymmetric Michael addition reactions. The $[(S)\text{-}Py]_x$-TPB-DMTP-COF with 17% [(S)-Py] content showed 100% conversion within 12 h and an e.e. value of 92% in water at room temperature. Due to the concentration effect of the nanopores, this $[(S)\text{-}Py]_{0.17}$-TPB-DMTP-COF is more active compared to the molecular catalysts. After improving the content density of catalytic sites on the pore walls, the catalytic activity shows a decreasing tendency

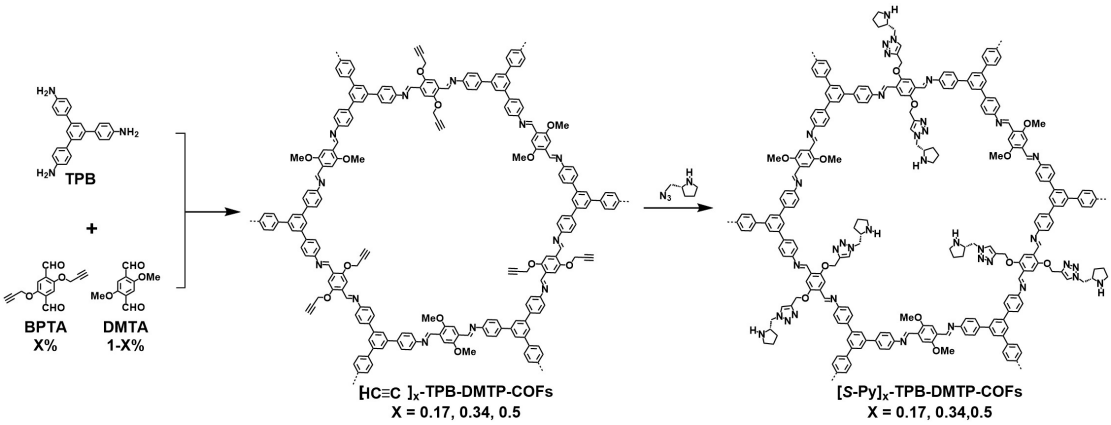

Figure 9. Integrate chiral catalytic sites into 2D COFs using surface engineering

because of the limited space in the pore channels. Remarkably, the $[(S)\text{-Py}]_{0.17}$-TPB-DMTP-COF can be reused at least five cycles without significant loss of its structural integrity and catalytic performance.

COFs materials provide a confined nanospace to coordinate metal species that can be further used as catalysts. For example, Pd(II) ions can coordinate to the imine bonds in the imine-linked COF- LZU1 (Figure 10) that serves as a catalyst for Suzuki-Miyaura coupling reaction.[34] Interestingly, COF walls' Pd ions could access the substrate and the reactant. Moreover, the Pd ions form a heterogeneous catalytic system and these ions are catalytically active forming. This catalyst system is suitable to many reactants and show outstanding cycle performance for catalysis.

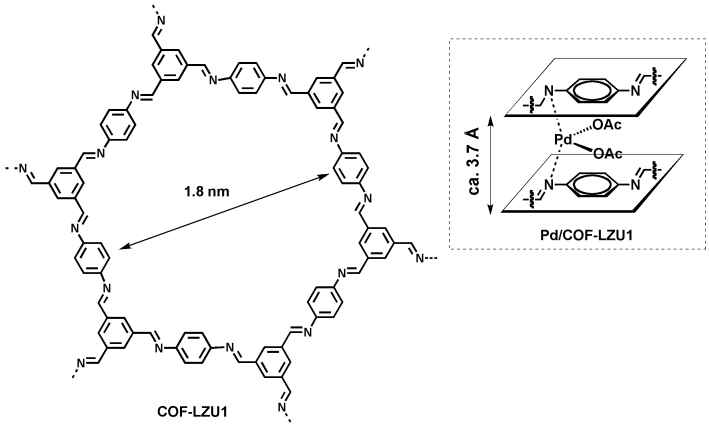

Figure 10. Synthesis and design of COF-LZU1 and Pd/COF-LZU1

1.1.5.2 Semiconduction and Photoconduction

1.1.5.2.1 Semiconduction

In 2008, using COFs materials for the construction of optoelectronic and electronic materials was demonstrated. Monomer pyrene-2,7-diboronic acid (PDBA) were used. Monomer HTTP molecules were used as the vertices to forme π-electronic hexagonal TP-COF (Figure 11).[35] TP-COF's structure is belt-shaped and the width of belt is around 300 nm (SEM images) while the thickness TP-COF is about 100 nm in microns. Simulations exhibited that TP-COF applied AA stacking mode according to the calculated and observed experimental PXRD patterns. Interestingly, the luminescence of TP-COF is strong blue due to the pyrene-building units' excitation. Therefore, triphenylene's excitation energy could transfer to different pyrene units within networks as well. As a consequence, a wide range photons could be harvested for TP-COF material from the ultraviolet to the visible regions. TP-COF's π-electronic components' AA stacking structure make TP-COF semiconducting material. Therefore, hole transport though COF skeleton could be obtained by TP-COF. Electric currents On off switching properties were confirmed with the *I-V* curve measurements.

1.1.5.2.2 Photoconduction

PDBA's self-condensation could construct photoconductive COF named PPy-COF, which is the first instance for COFs filed (Figure 2).[35] The shape of PPy-COF is cubic shape. And the length, width, and thickness of PPy-COF are in the micrometer range. The luminescence of PPy-COF is blue due to the pyrene monomer. PPy-COF fluorescence has an anisotropy of only 0.001. TP-COF's anisotropy is 0.017. This is because the building units within TP-COF and PPy-COF are different. The PPy-COF's excitons could come through the COFs' sheet. And PPy-COF's excitons could come through across the layers. PPy-COF have a quick response upon light irradiation.

1.1.5.3 Gas capture and separation

1.1.5.3.1 Gas storage

Recently, using COFs materials for removing and separating small gas molecule. Over last decades, many COFs have exhibited selective adsorption behaviour for

small gas molecules, and some COFs have been investigated for the separation of mixed gases by breakthrough experiments as well. In addition, modification of the structures and channel wall properties of COFs at the molecular level is an efficient way to tune their selective adsorption and separation performance. Apart from increasing the pore volume, BET, and adjusting appropriate pore size, introducing functional polar sites within COFs materials could improve the interactions between the adsorbent and gas molecules.

Table 1. Typical examples of COFs for carbon dioxide capture.

COFs	**Linkage**	S_{BET} ($m^2 g^{-1}$)	**Pore width (nm)**	**Pore volume** ($cm^3 g^{-1}$)	**CO_2 uptake** (mg g^{-1})		**CO_2/ N_2**	**Qst** ($kJmol^{-1}$)
					273 K	298 K		
COF-1	Boroxine	750	0.9	0.3	102	230[a]		
COF-5	Boronate ester	1670	2.7	1.07	62	870[a]		
COF-6	Boronate ester	750	0.9	0.32	170	310[a]		
COF-8	Boronate ester	1350	1.6	0.69	66	630[a]		
COF-10	Boronate ester	1760	3.2	1.44	54	1010[a]		
COF-102	Boroxine	3620	1.2	1.55	68	1200[a]		
COF-103	Boroxine	3530	1.2	1.54	76	1190[a]		
APTES-COF-1	Boroxine	490			46			
ILCOF-1	Imine	2723	2.3	1.21	62	35		
TpPa-1	Imine	535	1.3		160			

TpPa-2	Imine	339	1.4		126			
TpPa-NO_2	Imine	129	1.4		146			
TpPa-F_4	Imine	438	1.4		70			
TpBD	Imine	537	1.7		80			
TpBD-Me_2	Imine	468	1.4		74			
TpBD-$(OMe)_2$	Imine	330	1.4		54			
TpBD-$(NO_2)_2$	Imine	195	1.7		104			
TpPa-COF (Microwave)	Imine	725	1.3	1.1	218	87	32	34.1
TAPB-TFPB	Imine	229	4.4		40			
*i*PrTAPB-TFPB	Imine	390.6	5.0		31			
TAPB-TFP	Imine	567	2.6		180			
*i*PrTAPB-TFP	Imine	756	3.4		105			
N-COF	Imine	1700	1.1	0.84	122.4	64.8		
TH-COF-1	Imine	684	1.1	0.74	128	97	19	31
TRITER-1	Imine	716	1.7	0.32	589[b]	137[b]		
3D-Py-COF	Imine	1290	0.59	0.72	156		22.2	17.4
$[HO]_{25\%}$-H_2P-COF	Imine	1054	2.5	0.89	54	31		32.2
$[HO]_{50\%}$-H_2P-C	Imine	1089	2.5	0.91	46	34		29.4

OF								
$[HO]_{75\%}$-H_2P-COF	Imine	1153	2.5	0.96	52	32		31.5
$[HO]_{100\%}$-H_2P-COF	Imine	1284	2.5	1.02	63	35	8	36.4
$[HO_2C]_{25\%}$-H_2P-COF	Imine	786	2.2	0.78	96	58		38.2
$[HO_2C]_{50\%}$-H_2P-COF	Imine	673	1.9	0.66	134	67		39.6
$[HO_2C]_{75\%}$-H_2P-COF	Imine	482	1.7	0.54	157	72		41.2
$[HO_2C]_{100\%}$-H_2P-COF	Imine	364	1.4	0.43	174	76	77	43.5
$[HC\equiv C]_0$-H_2P-COF	Imine	1474	2.5		72	38		17.2
$[HC\equiv C]_{25}$-H_2P-COF	Imine	1431	2.3		54	29		16.8
$[HC\equiv C]_{50}$-H_2P-COF	Imine	962	2.1		48	26		16.5
$[HC\equiv C]_{75}$-H_2P-COF	Imine	683	1.9		43	24		15.7
$[HC\equiv C]_{100}$-H_2P-COF	Imine	426	1.6		39	20		15.3
$[Et]_{25}$-H_2P-COF	Imine	1326	2.2		55	29		15.5
$[Et]_{50}$-H_2P-COF	Imine	821	1.9		46	25		15.3
$[Et]_{75}$-H_2P-COF	Imine	485	1.6		41	23		15.6
$[Et]_{100}$-H_2P-COF	Imine	187	1.5		38	21		15.3
$[MeOAc]_{25}$-H_2	Imine	1238	2.1		84	42		16.4

P-COF								
$[MeOAc]_{50}$-H_2 P-COF	Imine	754	1.8		88	47		17.1
$[MeOAc]_{75}$-H_2 P-COF	Imine	472	1.5		82	42		16.7
$[MeOAc]_{100}$-H_2 P-COF	Imine	156	1.1		65	34		17.8
$[AcOH]_{25}$-H_2P-COF	Imine	1252	2.2		94	50		17.7
$[AcOH]_{50}$-H_2P-COF	Imine	866	1.8		117	64		17.8
$[AcOH]_{75}$-H_2P-COF	Imine	402	1.5		109	58		18.3
$[AcOH]_{100}$-H_2P-COF	Imine	186	1.3		96	50		18.8
$[EtOH]_{25}$-H_2P-COF	Imine	1248	2.2		92	50		18.2
$[EtOH]_{50}$-H_2P-COF	Imine	784	1.9		124	71		19.7
$[EtOH]_{75}$-H_2P-COF	Imine	486	1.6		117	63		19.2
$[EtOH]_{100}$-H_2P-COF	Imine	214	1.4		84	44		19.3
$[EtNH_2]_{25}$-H_2P-COF	Imine	1402	2.2		116	60		20.4
$[EtNH_2]_{50}$-H_2P-COF	Imine	1044	1.9		157	82		20.9
$[EtNH_2]_{75}$-H_2P-COF	Imine	568	1.6		133	67		20.8

$[EtNH_2]_{100}$-H_2P-COF	Imine	382	1.3		97	52		20.9
$[HO]_{25\%}$-TAPH-COF	Imine	927	2.0	0.75	58	32	15	30.9
$[HO]_{50\%}$-TAPH-COF	Imine	930	2.0	0.89	56	37	13	28.2
$[HO]_{75\%}$-TAPH-COF	Imine	944	2.0	0.99	61	38	14	28.3
$[HO]_{100\%}$-TAPH-COF	Imine	1056	2.0	1.02	62	38	16	31.1
$[N=N]_{25\%}$-TAPH-COF	Imine	702	1.7	0.72	207	115	78	43.4
$[N=N]_{50\%}$-TAPH-COF	Imine	560	1.4	0.64	112	67	49	36
$[N=N]_{75\%}$-TAPH-COF	Imine	320	1.3	0.59	77	44	48	31
$[N=N]_{100\%}$-TAPH-COFs	Imine	250	1.2	0.54	60	39	57	30.7
$[C=C]_{25\%}$-TAPH-COF	Imine	680	1.7	0.70	61	40	18	30.3
$[C=C]_{50\%}$-TAPH-COF	Imine	460	1.6	0.66	63	41	16	29
$[C=C]_{75\%}$-TAPH-COF	Imine	390	1.3	0.55	55	34	22	28.7
$[C=C]_{100\%}$-TAPH-COF	Imine	310	1.2	0.51	51	34	27	28.5
$[HO]_{25\%}$-Py-COF	Imine	1977	2.2	2.16	91.7	72.4		16.9
$[HO]_{50\%}$-Py-CO	Imine	2153	2.2	2.72	11	68		17.3

F					4.2	.6		
$[Et_4NBr]_{25\%}$-Py -COF	Imine	1014	2.0	1.05	119.6	80.9		22.9
$[Et_4NBr]_{25\%}$-Py -COF	Imine	879	1.6	0.99	164.6	87.3		28.7
ACOF-1	Azine	1176	0.94	0.91	177	90	40	27.6
COF-JLU2	Azine	410	0.96	0.56	217	165	77	31
HEX-COF1	Azine	1214	1.1	0.62	200	120		42
NTU-COF-2	Imine/Boronate ester	1619	2.5	0.86	104			27.0

CO_2 uptake at 1 bar except [a]55 bar and [b]5 bar

1.1.5.3.2 Carbon Dioxide storage and separation

Because of the human's activities, the global climate is changing induced by the increasing green house gas CO_2 concentration in the atmosphere. This issue has become an urgent and important challenge facing humanity.[36,37] A global integrated measure, namely CO_2 capture and sequestration (CCS) was launched to tackle this problem. Therefore, various CO_2 capture technologies have been proposed in the past several decades to slow down the greenhouse effect. Due to the precise structural design and chemical stability, COFs have been demonstrated great potential as host materials for CO_2 storage and separation in the last few years (Table 1). Recent research works exhibited the influence of S_{BET} surface areas, pore size, and pore volume on the amount of CO_2 adsorbed, as well as different functional groups' effect on the CO_2 capture capacity.

In 2015, 1,3,5-triformylphloroglucinol and hydrazine hydrate (N_2H_4) were used to form azine-linked COF named COF-JLU2. [38] The BET of COF-JLU2 is 415 m^2g^{-1} with a dominant pore diameter of 0.96 nm. This COF (COF-JLU2) could adsorb 217

mg g^{-1} CO_2 at 273k and 1bar and the CO_2/N_2 selectivity is 77. The highest storage capacity for COF-JLU2 among the COFs was mainly ascribed to the its small pore sizes. Furthermore, the same group use 1,3,5-triformylbenzene and hydrazine hydrate (N_2H_4) to poly-synthsis another azine-linked ACOF-1, in 2014.[38,39] The BET surface area ACOF-1 is 1176 m^2g^{-1} and the pore size is 0.94 nm. ACOF-1 could absorb 177 mgg^{-1} of CO_2 at 273K and 1bar. According to the adsorption isotherms at 273K and 298K and at zero coverage, the CO_2 isosteric heat of adsorption (Q_{st}) of ACOF-1 is around 27.6 kJ mol^{-1}. Moreover, CO_2/N_2 selectivity was 40 at 273k. A more recent report showd that the CO_2 capture properties could be improved by azine linked COFs as well. The average pore size of HEX-COF1 (Figure 11) is 1nm The BET surface area is around 1200 m^2g^{-1} for HEX-COF1. HEX-COF1 could uptake 200 mg g^{-1} CO_2 at 273k and 1atm with the Q_{st} of 42 kJ mol^{-1}.[40] These studies demonstrated that introducing active heteroatoms in the skeleton could be a effective strategy for improving the CO_2 capture capacity.

In 2015, our group used a traditional imine-based 2D COF as a platform with phenol group on the pore walls surface and porphyrin at the vertices for CO_2 storage and capture (Figure 12).[41] In this work, the authors used a ring opening reaction between phenol units and succinic anhydride. Therefore, different content carboxylic acid organic units were introduced to functionalize the pore channel surface Also, the carboxylic acid contents can be changed from 25% to 50%, 75% and 100% via changing the phenol group contents. The functionalized COFs exhibited enhanced CO_2 capture capacity and the 100% carboxylic acid functionalized COF showed the best CO_2 adsorption properties (180 mg g^{-1} at 273k and 1atm) among these functionalized COFs with Q_{st} of 43.5 kJ mol^{-1}. The CO_2 capture capacity of $[HO_2C]_{X\%}$-H_2P-COFs and Q_{st} enahced with increasing content of carboxylic acid functional groups. Moreover, the breakthrough time of $[HO_2C]_{100\%}$-H_2P-COF is 50. The breakthrough time of $[HO]_{100\%}$-H_2P-COF is 15. Longer breakthrough times are desirable and important for effecitent CO_2 capture and separation. In addition, as for the cycling performance, no significant decrease was observed in $[HO_2C]_{100\%}$-H_2P-COFs after ten cycles.

In the same year, our group used the ethynyl-appended building units to synthesis 2D COFs with walls where the designable content of ethynyl units is anchored.[42] We have synthesized 20 different COFs in which the channel surface was functionalized with different functional groups (Figure 13). Interestingly, all these functional groups range from hydrophilic to hydrophobic and from acidic to basic. In addition, amino functionalized COF $[EtNH_2]_{50}$-H_2P-COF exhibited the best adsorption capacity (160 mgg^{-1} at 273K and 1bar) and highest Q_{st} values (20.9 kJ mol^{-1}) among these functionalized COFs. The breakthrough simulation exhibited that the breakthrough time is 15.

In a more recent study, another group reported that the 4-phenyl-azobenzoyl (PhAzo) functional groups and 4-stilbenecarbonyl chloride (PhSti) feature were introduced into the pore walls via acylation reaction to improve the CO_2 capture capacity.[43] Among all the functionalized COFs, $[N{=}N]_{25\%}$-TAPH-COFs exhibited the highest CO_2 uptake capacity of 207 mgg^{-1} at 273K, which is 3-fold higher than $[HO]_{25\%}$-TAPH-COFs. Moreover, Williamson ether reaction was used to introduce different content of ionic liquids for functionalizing COFs' pore surface to enhance CO_2 adsorb ability. $[Et_4NBr]_{50\%}$-Py-COFs can adsorb 164.6 mgg^{-1} CO_2 at

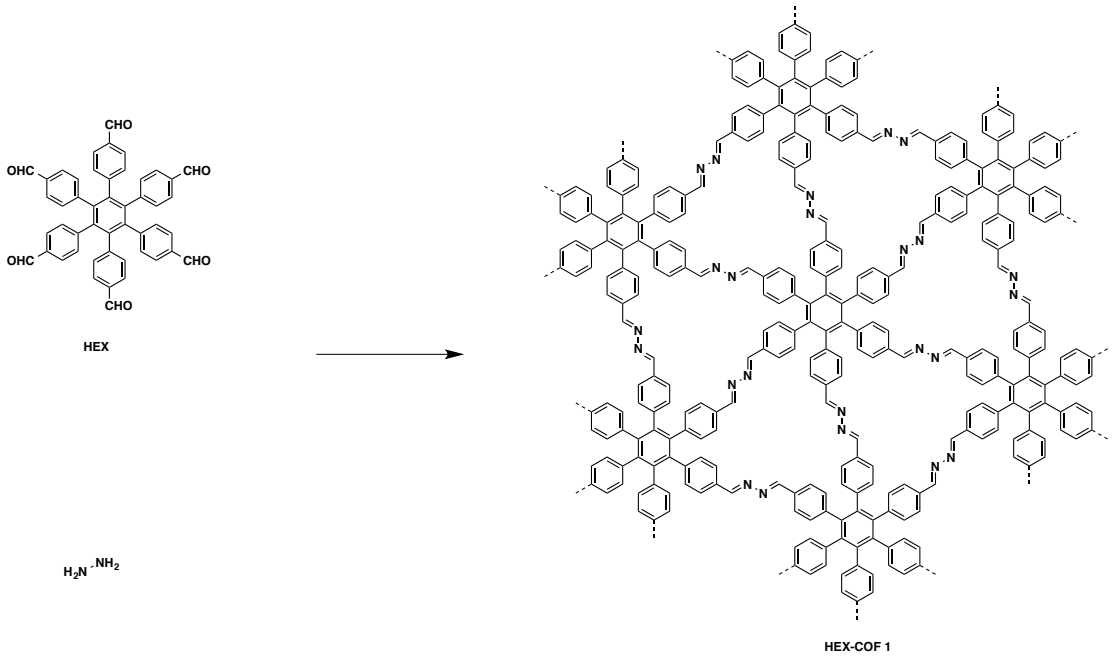

Figure 11. HEX-COF1 syntehsis process

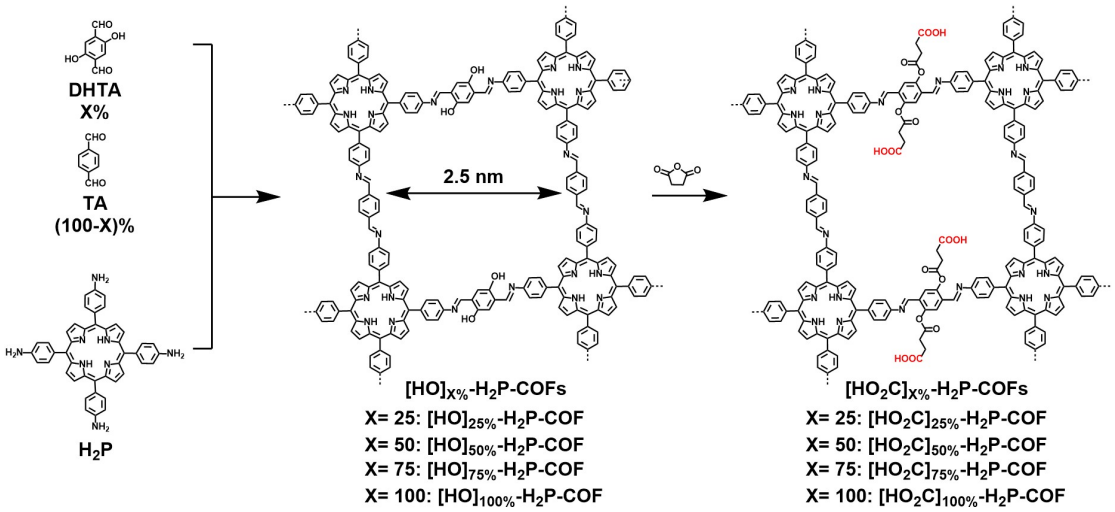

Figure 12. Pore wall functionalization of porphyrin COFs to integrate carboxylic acid groups for efficient CO_2 capture.

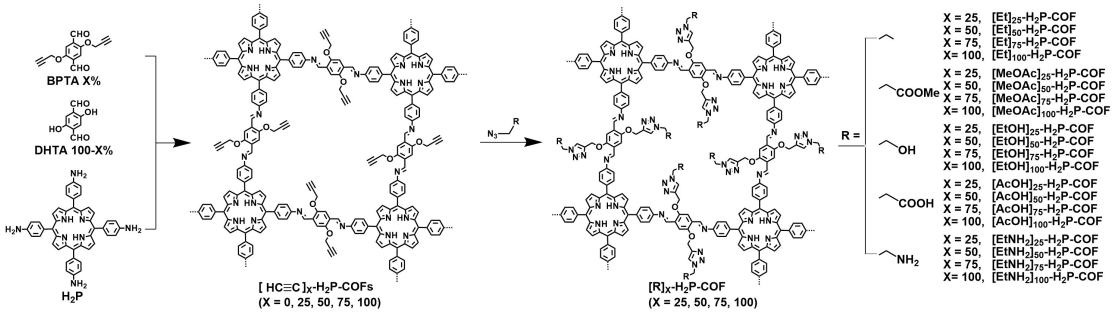

Figure 13. Pore surface engineering strategy to integrate various functional groups onto the pore time of $[EtNH_2]_{50}$-H_2P-COF (25) is longer than $[HC{\equiv}C]_{50}$-H_2P-COFs (7).

273K and 1bar with the Q_{st} of 28.7 kJmol-1, which is highest uptake amount among the ionic liquids functionalized COFs.[44] Therefore, the precise pore channel modification is powerful way to enhance the CO_2 uptake capacity.

1.1.5.3.3 Hydrogen storage

Owing to the neither air pollution nor greenhouse-gas emissions after H2 burning, Hydrogen is regarded as a promising candidate for the replacement of present carbon-based energy source.[45,46] Therefore, developing efficient technology and materials for storage and transportation of abundant H_2 energy source is essential and urgent task for humanity. In this respect, porous materials are valuable and expectable for tapping enormous amounts of hydrogen due to their outstanding porosity, which have attracted much attention in recent years.

Owing to comparable surface area and low density, COFs materials exhibit high hydrogen captures capacity under the same condition compared with other porous materials. In 2008, 3D COFs' hydrogen capture capacity is 2.5-3 times was predicted higher than 2D COFs' hydrogen capture capacity. 3D COFs has larger surface area and volume, compared with 2D COFs.[47] The recent experimental results exhibited that the prediction was confirmed. The BET surface area of 3D COF-102 is around 3620 m^2g^{-1} and pore size about 1.2 nm. Under 35 bar and 77 k, this COF has highest hydrogen uptake capacity of 7.2 wt%. As for 2D COFs, COF-10 exhibits 3.92 wt% hydrogen adsorption ability at the same condition, which is the highest hydrogen uptake capacity among the 2D COFs. Also, some researchers attempted to explore porous materials to capture H_2 at low pressure since using low pressure could reduce the cost compared with higher pressure. In 2012, monomer 1,4-benzenediboronic acid (BDBA) and cyclotricatechylene (CTC) were used to form CTC-COF.[48] The BET of CTC-COF is 1710 m^2g^{-1} and the pore size is 2.26 nm. CTC-COF can capture 1.12wt% H_2 at 800 mmHg. In 2013, Kaderi and coworkers reported that TDCOF-5 shows 1.6 wt% H_2 uptake capacity at 1bar and 77k, which is the highest value among all the known 2D COFs in this condition.[49] In 2015, COF-JLU2 exhibited 1.6wt% H_2 uptake at the same condition, which is comparable to TDCOF-5.[38]

1.1.5.3.4 Methane storage

Methane (CH_4) is the main component of natural gas and constitutes around two-thirds of the fossil fuels on earth. Due to the high heat of combustion, methane is recognized as an alternative source of clean energy. Because of high storage capacity at room temperature and moderate pressures, novel porous materials would to be attractive and promising candidates for storage and separation of CH_4.

Among COFs library, 3D COFs are superior to 2D COFs in CH_4 adsorption since 3D COFs have smaller pore size and higher BET surface area. For instance, 3D COF-102 could capture 187 mgg^{-1} CH_4 at 35 bar and 298 k, which is the highest value among COFs.[47] The CH_4 uptake value of 3D COF-103 is 175 mg g^{-1} at the same condition. On the contrary, 2D COF-5 showed 89 mgg^{-1} capture amount of CH_4 at the same condition, which is largest value among 2D COFs. Moreover, some researchers

try to use imine-based 2D COFs as platform for methane adsorption in recent years. In 2014, 1LCOF-1 showed 0.9 wt% uptake amount at 273K and 1bar with the Q_{st} values of 13.7 kJ mol^{-1}.[50] 1LCOF-1 could capture 22 wt% CH_4 at 298K and 40 bar as well. In 2014, the methane adsorbed of ACOF-1 was 1.15 wt% CH_4. In addition, the CH_4 uptake of COF-JLU2 reached 3.8 wt% at the same condition with the Q_{st} value of 20.5 kJ mol-1, which is highest among imine liked 2D COFs.

1.1.5.3.5 Ammonia storage

Because ammonia (NH_3) is toxic, corrosive and difficult to handle transported. Therefore, ammonia is compressed as liquid for industrial applications.[51] Therefore, efficiently storage and transport of ammonia gas is essential and urgent. In this respect, boronate-ester linked COFs are suitable for the storage and release of ammonia. This is because boron sites within COFs materials have a improved interaction toward ammonia. In 2010, a boronate-ester linked COF, named COF-10. Under 298k and 1bar, this COF has the highest ammonia capture capacity of 15 mol kg^{-1} among the porous polymers[52] In this case, ammonia can be released and generated back to free ammonia. There is no significant decrease and the structural integrity can be maintained after several cycles of adsorption and desorption as well.

1.1.5.3.6 Membranes

Gas molecules' different diffusion rates within the membranes are a kinetically controllable process. An alternative route for introducing COFs materials into membrane-based applications is to incorporate COFs particles into different polymers to prepare mixed-matrix membranes (MMMs). Compared with other porous solids such as MOFs and zeolites be used in MMMs, COFs have two distinct advantages: (1) COFs with different structures and compositions could be synthesized; and (2) the building blocks provide attractive platform for surface modifications, which could enhance their interaction toward to polymer matrices.

Herein, NUS-2 and NUS-3 COFs were synthesized and exfoliated into nanosheets. NUS-2 and NUS-3 COFs' nanosheets were used as COF fillers to prepare MMMs.[53] The BET surface area of NUS-2 is abpout 415 m^2g^{-1}. The pore diameter of

NUS-2 is 0.9 nm. The BET of NUS-3 is 757 m^2g^{-1} and the pore size is 2.1nm. In addition, NUS-2 and NUS-3 can capture 154 and 66 mgg^{-1} CO_2 gas molecule at 273K and 1bar, respectively. For NUS-2 and NUS-3 COFs, The uptake amount of CO_2 is much higher than that other gases molecules (CH_4, H_2) uptake under the same conditions for these two COFs. According to the the single gas isotherms, the binary CO_2/CH_4 and CO_2/H_2 selectivities for NUS-2 were calculated to be 58.8 and 116.8 at 273 k, respectively. Unlike NUS-2, The NUS-3 showed that this COF has IAST CO_2/CH_4 and CO_2/H_2 of NUS-3 around 29.3 and 22.0 at the same condition. Therefore, compared with NUS-3, NUS-2 is the more effective porous COF fillers in preparing MMMS for H_2/CO_2 separation due to the higher CO_2/H_2 selectivity itself. Different MMMs such as NUS-2/NUS-3@PBI and NUS-2/NUS-3@Ultem (poly (ether imide)) and (polybenzimidazole) were prepared as well. These MMMs have a thickness around 50−100μm. The COF loading amount in membranes was calculated based on the weight of COFs, which was divided by the total weight of COFs materials fillers and polymers substrates. In order to evaluate the gas barrier performance of MMMs, different single gas barriere measurement were performed under different pressures (2, 3.5, and 5bar, respectively). According to the literature, incorporating lower amounts of COFs (10 and 20 wt%) into Ultem could both increase the solubility and diffusivity of CO_2. However, NUS-3@Ultem has a comparable CO_2/CH_4 selectivity but a much larger CO_2 permeability. This is because the large pore size NUS-3 lead to faster gas molecule diffusivity. Moreover, a same trend happened in the low COF content Ultem@MMMs used for the H_2/CO_2 separation properties. However, the NUS-2@Ultem has a further improve CO_2 gas molecule permeability. As the COFs content increased to 30wt%, NUS-3@Ultem membrane showed decreased CO_2/CH_4 selectivity and CO_2 barrier properties. This was the reason why that higher COFs content is difficult to prepare homogeneous membrane without any defects within the membrane materials.

In 2016, polymer PBI-BuI was used as matrix to prepare a series of highly flexible TpPa-1@PBI-BuI and TpBD@PBIBuI hybrid membranes.[54] H_2, N_2, CH_4, and CO_2 single gas permanence studies were measured at 308 k and 20 atm upstream

pressure. The single H_2 and CO_2 permeability of these hybrid membranes increased almost linearly with the increased COFs materials loading amount. After addition of 40% content TpPa-1, the hybrid membrane has H_2 permeability increased from 6.2 barrier (pristine PBI) to 18.8 barrier. Moreover, an incensement in H_2/CH_4 selectivity from 155 to 165.5 and H_2/N_2 selectivity from 69 to 79 was observed in this membrane. However, the CO_2/N_2 selectivities were slightly decreased and CO_2/CH_4 selectivity remained appreciable when COFs loading amount reaches 40% TpPa-1. In a more recent study, they used COF-300 and $Zn_2(bdc)_2(dabco)$ or ZIF-8a to prepare novel membranes with COF-MOF materials. The H_2/CO_2 selectivity of polymeric membranes is higher than the pure COF-300 or MOF membranes. Also, the membranes' gas barrier properties are up the polymer's Robeson upper bound. They use H_2/CO_2 1:1 mixture to measure the gas mixture separation capability for the COF-MOF composite membranes. [COF-300]-[$Zn_2(bdc)_2(dabco)$] membrane has a H_2/CO_2 separation factor around 12.6. This value is greatly higher than the vales of COF-300 membrane (6.0) and the values of 7.0 for $Zn_2(bdc)_2(dabco)$ membrane. Moreover, the H_2/CO_2 mixture separation factor of [COF-300]-[ZIF-8] membrane is around 13.5. This value is higher than the values of the COF-300 membrane (6.0) and the values of the ZIF-8 membrane (9.1). In the last several years, although progress has been made in the hybrid membranes for gas separation. However, improving morphologies including particles' uniform distribution and particle/polymer adhesion is necessary for large-scale fabrication and application for industry.

1.1.5.3.7. Conclusion and Perspectives

In the last decades, some excited research progresses were achieved using COFs materials as potential solid porous materials for CO_2, H_2, CH_4, NH_3 capture and separation. As for the CO_2 adsorption, high BET and pore volume, and small pore size below 1nm should be taken into consideration when COFs materials were designed for CO_2 capture and separation. Also, the promising development demonstrated that introducing functional groups or polar heteroatoms into the skeleton via COFs predesign or post channel wall functionalization is a powerful

strategy for enhancing the interaction between COFs networks and CO_2 gas molecules. To date, most of COFs exhibited physical adsorption for CO_2 rather than chemical adsorption, which is suitable for CO_2 capture at high pressure. Therefore, chemical adsorption for CO_2 at low pressure (0.15 bars) using COFs materials is necessary and urgent since the content of CO_2 in the flue gas is lower than 0.15 bars. Moreover, COF-based membranes have been used for gas separation such as CO_2/N_2, CO_2/CH_4, CO_2/H_2, which demonstrated that COFs-based membranes have the comparable performance compared with other porous materials based membranes. Even though COFs materials exhibited promising application and potential in this area, there is still a long way for COFs materials used for practical application in industries.

1.2 Scope of This Thesis

COFs is novel porous crystalline materials. Introduing lightweight elements into frameworks with strong covalent bonds could form COFs materials. COFs' distinct feature is that organic building blocks could be introduced into extended 2D or 3D structures. The predesignable and controllable features of COFs make these materials as a promising platform for exploring functions such as gas storage, photoelectronics, catalysis, and semiconductors. Carbon dioxide (CO_2) is the main component of greenhouse gases and its concentration in atmosphere are rapidly increased to 400 ppm, leading to a series of detrimental effects including rising sea level, global climate warming. Therefore, exploring effective materials and novel technology for CO_2 adsorption and storage is an important task. In this study, I focused on the design and synthesis of COFs with specific skeletons and pore walls, with an aim to achieve systems with exceptional CO_2 capture capability.

In chapter 1, I reviewed the field of COFs by summarizing the general principle for the structural design and illustrating the synthetic methods and approaches. I further summarized the structural diversity and functional design based on skeletons and pores, by focusing on the progress in CO_2 capture and separation.

In chapter 2, I designed and synthesized a series of hexagonal COFs with a similar pore size but with different skeleton structures, with an aim to elucidating the

design principle of the skeletons for CO_2 capture. Especially, different triarylamine units' contents were introduced into COFs skeleton. TFPB-TAPB-COF could capture 12 and 20 mg $g^{-1}CO_2$ gas molecule at 298 and 273 K, respectively. This COF have no triarylamine. Under 298 and 273 K TFPA-TAPB-COF could capture 33 and 61 mg g^{-1} CO_2. This COF have three triarylamine. BTMA-TAPA-COF could capture 45 and 84 mg g^{-1} CO_2 at the same condition. This COF have three triarylamine. Notably, TFPA-TAPA-COF could adsorb 52 and 105 mg g^{-1} CO_2 at the same condition. This COF have six triarylamine. Triarylamine units with networks dominate the CO_2 adsorption process. Also, the CO_2 uptake was enhanced with triarylamine contents increasing. The experimental results clearly demonstrate a new design principle for CO_2 capture.

In chapter 3, I designed and synthesized two 3D COFs, i.e. TAPA-TADM-COF and TAPA-TA-COF, which were constructed using tetrahedral sp^3-nitrogen building blocks for CO_2 capture and separation. The structures and porosities of these COFs were investigated in detail. Notably, these COFs possess mciropores and high BET surface areas. As a result, the high BET surface area and the small pore size endow these COFs with greatly improved CO_2 uptake capacity. At 298 and 273 K, TAPA-TA-COF could capture 54 and 127 mg g^{-1} CO_2. By contrast, TAPA-TADM-COF could adsorb 82 and 170 mg g^{-1} CO_2 at the same condition. These capacities of TAPA-TADM are 1.4 fold larger than those of TAPA-TA-COF because of a higher BET surface and a smaller pore size of TAPA-TADM-COF.

In chapter 4, I designed and synthesized a series of hybrids of COFs with amines, targeting for constructing CO_2 separation systems with exceptional selectivity. For this purpose, I designed and synthesized a novel COF material, i.e., TAPB-DMPTA-COF, which is highly porous and stable against water, strong acid and base. The COF possesses hexagonally aligned mesoporous channels and exhibited a high capacity of loading CO_2-philic tetraethylenepentamine (TEPA) in the pores. The uptake and separation of CO_2 were investigated in detail by using various methods. As a result, TAPB-DMPTA-COF only takes up 11, 6.6, and 3.9 mg g^{-1} CO_2 at 0.15 bar and 273, 298, and 323 K, respectively. The TEPA-hybridized

TAPB-DMPTA-COF exhibited dramatically increased CO_2 adsorption capacities under the same conditions. Especially, 52wt%TEPA @DMPTA-TAPB-COF takes up 122.8, 111.4, and 111.1 mg g^{-1} of CO_2 at the same condition. These capacities are 11.2, 16.9 and 28.5 fold greater than those of TAPB-DMPTA-COF itself. These values are the highest performance for CO_2 within 2D and 3D COFs materials. The TEPA-hybridized COFs exhibit high CO_2 uptake and outstanding CO_2/N_2 selectivity at low pressure and high temperature.

In chapter 5, I summarized the results of this work and showed the perspectives of COFs for CO_2 adsorption and separation. Through the three-year studies, I unambiguously demonstrated the principle of design and synthesis of COFs for CO_2 uptake and separation. I developed a series of novel COFs systems for the uptake of CO_2 with high capacity and selectivity. These results clearly show the high potential of COFs for structural design and set up a new platform to address environmental issues.

In this thesis, measurements done by co-workers have been listed: Dr. Hong Xu and Dr. Qiuhong Chen in our group contributed on structure optimization using DFT and DFT-B methods and PXRD simulation.

1.3 Reference

(1) Wu, D.; Xu, F.; Sun, B.; Fu, R.; He, H.; Matyjaszewski, K. Design and preparation of porous polymers. *Chem. Rev.,* **2012,** *112*, 3959-4015.

(2) Das, S.; Heasman, P.; Ben, T.; Qiu, S. Porous Organic Materials: Strategic Design and Structure-Function Correlation. *Chem. Rev.,* **2017,** *117*, 1515-1563.

(3) Pera-Titus, M. Porous inorganic membranes for CO_2 capture: present and prospects. *Chem. Rev.,* **2014,** *114*, 1413-1492.

(4) Côté, A. P.; Benin, A. I.; Ockwig, N. W.; O'Keeffe, M.; Matzger, A. J.; Yaghi, O. M. Porous, Crystalline, Covalent Organic Frameworks. *Science.,* **2005,** *310* , 1166.

(5) Huang, N.; Wang, P.; Jiang, D. Covalent organic frameworks: a materials platform for structural and functional designs. *Nat. Rev. Mat.,* **2016,** *1* , 16068. Doi: 10.1038/natrevmats2016.68.

(6) Feng, X.; Ding, X.; Jiang, D. Covalent organic frameworks. *Chem. Soc. Rev.,* **2012,** *41*, 6010-6022.

(7) El-Kaderi, H. M.; Hunt, J. R.; Mendoza-Cortés, J. L.; Côté, A. P.; Taylor, R. E.; O'Keeffe, M.; Yaghi, O. M. Designed Synthesis of 3D Covalent Organic Frameworks. *Science.,* **2007,** *316*, 268.

(8) Rowan. S. J, Cantrell. S. J, Cousins. G. R. L, Sanders. J. K. M, Stoddart. J. F. Dynamic Covalent Chemistry. *Angew. Chem. Int. Ed.* **2002**, *41*, 898-952

(9) Hunt. J. R, Doonan. C. J, LeVangie. J. D, Côté, Yaghi. O. M. Reticular Synthesis of Covalent Organic Borosilicate Frameworks. *J. Am Chem. Soc*., **2008**, *130*, 11872–11873

(10) Lanni, L. M.; Tilford, R. W.; Bharathy, M.; Lavigne, J. J. Enhanced Hydrolytic Stability of Self-Assembling Alkylated Two-Dimensional Covalent Organic Frameworks. *J. Am Chem. Soc*., **2011,** *133* (35), 13975.

(11) Uribe-Romo. F. J, Hunt. J. R, Furukawa. H, Klöck. C, O'Keeffe. M, Yaghi. O. M, A Crystalline Imine-Linked 3-D Porous Covalent Organic Framework. *J. Am Chem. Soc*., **2009**, *131*, 4570–4571

(12) Wan, S.; Gándara, F.; Asano, A.; Furukawa, H.; Saeki, A.; Dey, S. K.; Liao, L.; Ambrogio, M. W.; Botros, Y. Y.; Duan, X.et al. Covalent Organic Frameworks with High Charge Carrier Mobility. *Chem. Mater.,* **2011,** *23*, 4094-4097.

(13) Uribe-Romo, F. J.; Doonan, C. J.; Furukawa, H.; Oisaki, K.; Yaghi, O. M. Crystalline Covalent Organic Frameworks with Hydrazone Linkages. *J. Am Chem. Soc*., **2011,** *133*, 11478-11481.

(14) Dalapati, S.; Jin, S. B.; Gao, J.; Xu, Y. H.; Nagai, A.; Jiang, D. L. An Azine-Linked Covalent Organic Framework. *J. Am. Chem. Soc*., *135*, 17310-17313.

(15) Kuhn, P.; Antonietti, M.; Thomas, A. Porous, covalent triazine-based frameworks prepared by ionothermal synthesis. *Angew. Chem. Int. Ed.,* **2008,** *47*, 3450-3453.

(16) Bojdys, M. J.; Jeromenok, J.; Thomas, A.; Antonietti, M. Rational extension of the family of layered, covalent, triazine-based frameworks with regular porosity. *Adv. Mater.,* **2010,** *22*, 2202-2205.

(17) Bunck, D. N.; Dichtel, W. R. Internal functionalization of three-dimensional covalent organic frameworks. *Angew. Chem. Int. Ed.,* **2012,** *51*, 1885-1889.

(18) Huang, N.; Ding, X.; Kim, J.; Ihee, H.; Jiang, D. A Photoresponsive Smart Covalent Organic Framework. *Angew. Chem. Int. Ed.,* **2015,** *54*, 8704-8707.

(19) Wan, S.; Guo, J.; Kim, J.; Ihee, H.; Jiang, D. A belt-shaped, blue luminescent, and semiconducting covalent organic framework. *Angew. Chem. Int. Ed.,* **2008,** *47*, 8826-8830.

(20) Côté, A. P.; El-Kaderi, H. M.; Furukawa, H.; Hunt, J. R.; Yaghi, O. M. Reticular Synthesis of Microporous and Mesoporous 2D Covalent Organic Frameworks. *J. Am. Chem. Soc.,* **2007,** *129*, 12914-12915.

(21) Chen, X.; Addicoat, M.; Jin, E. Q.; Zhai, L. P.; Xu, H.; Huang, N.; Guo, Z. Q.; Liu, L. L.; Irle, S.; Jiang, D. L. Locking Covalent Organic Frameworks with Hydrogen Bonds: General and Remarkable Effects on Crystalline Structure, Physical Properties, and Photochemical Activity. *J. Am. Chem. Soc.,* **2015,** *137*, 3241-3247.

(22) Zhou, T.-Y.; Xu, S.-Q.; Wen, Q.; Pang, Z.-F.; Zhao, X. One-Step Construction of Two Different Kinds of Pores in a 2D Covalent Organic Framework. *J. Am. Chem. Soc.,* **2014,** *136*, 15885-15888.

(23) Zhu, Y.; Wan, S.; Jin, Y.; Zhang, W. Desymmetrized Vertex Design for the Synthesis of Covalent Organic Frameworks with Periodically Heterogeneous Pore Structures. *J. Am. Chem. Soc.,* **2015,** *137*, 13772-13775.

(24) Ding, X.; Guo, J.; Feng, X.; Honsho, Y.; Seki, S.; Maitarad, P.; Saeki, A.; Nagase, S.; Jiang, D. Synthesis of metallophthalocyanine covalent organic frameworks that exhibit high carrier mobility and photoconductivity. *Angew. Chem. Int. Ed.,* **2011,** *50*, 1289-1293.

(25) Kappe, C. O. Controlled microwave heating in modern organic synthesis. *Angew. Chem. Int. Ed.,* **2004,** *43*, 6250-6284.

(26) Makhseed, S.; Samuel, J. Hydrogen adsorption in microporous organic framework polymer. *Chem. Commun.,* **2008**, 4342-4344.

(27) Biswal, B. P.; Chandra, S.; Kandambeth, S.; Lukose, B.; Heine, T.; Banerjeet, R. Mechanochemical Synthesis of Chemically Stable Isoreticular Covalent Organic Frameworks. *J. Am. Chem. Soc.,* **2013,** *135*, 5328-5331.

(28) Colson, J. W.; Woll, A. R.; Mukherjee, A.; Levendorf, M. P.; Spitler, E. L.; Shields, V. B.; Spencer, M. G.; Park, J.; Dichtel, W. R. Oriented 2D Covalent Organic Framework Thin Films on Single-Layer Graphene. *Science.,* **2011,** *332*, 228.

(29) Hunt, J. R.; Doonan, C. J.; LeVangie, J. D.; Côté, A. P.; Yaghi, O. M. Reticular Synthesis of Covalent Organic Borosilicate Frameworks. *J. Am. Chem. Soc.,* **2008,** *130*, 11872-11873.

(30) Zwaneveld, N. A. A.; Pawlak, R.; Abel, M.; Catalin, D.; Gigmes, D.; Bertin, D.; Porte, L. Organized Formation of 2D Extended Covalent Organic Frameworks at Surfaces. *J. Am. Chem. Soc.,* **2008,** *130*, 6678-6679.

(31) Spitler, E. L.; Koo, B. T.; Novotney, J. L.; Colson, J. W.; Uribe-Romo, F. J.; Gutierrez, G. D.; Clancy, P.; Dichtel, W. R. A 2D Covalent Organic Framework with 4.7-nm Pores and Insight into Its Interlayer Stacking. *J. Am.*

Chem. Soc., **2011,** *133*, 19416-19421.

(32) Tilford, R. W.; Mugavero, S. J., 3rd; Pellechia, P. J.; Lavigne, J. J. Tailoring microporosity in covalent organic frameworks. *Adv. Mater.,* **2008,** *20*, 2741-2746.

(33) Nagai, A.; Guo, Z.; Feng, X.; Jin, S.; Chen, X.; Ding, X.; Jiang, D. Pore surface engineering in covalent organic frameworks. *Nat. Commun.,* **2011,** *2*, 536. Doi: 10.1038/ncomms1542.

(34) Xu, H.; Gao, J.; Jiang, D. L. Stable, crystalline, porous, covalent organic frameworks as a platform for chiral organocatalysts. *Nat. Chem.,* **2015,** *7*, 905-912.

(35) Ding, S. Y.; Gao, J.; Wang, Q.; Zhang, Y.; Song, W. G.; Su, C. Y.; Wang, W. Construction of Covalent Organic Framework for Catalysis: Pd/COF-LZU1 in Suzuki-Miyaura Coupling Reaction. *J. Am. Chem. Soc.,* **2011,** *133* (49), 19816-19822.

(36) Wan, S.; Guo, J.; Kim, J.; Ihee, H.; Jiang, D. A photoconductive covalent organic framework: self-condensed arene cubes composed of eclipsed 2D polypyrene sheets for photocurrent generation. *Angew. Chem. Int. Ed.,* **2009,** *48*, 5439-5442.

(37) Olah, G. A.; Prakash, G. K.; Goeppert, A. Anthropogenic chemical carbon cycle for a sustainable future. *J. Am. Chem. Soc.,* **2011,** *133*, 12881-12898.

(38) Aresta, M.; Dibenedetto, A.; Angelini, A. Catalysis for the valorization of exhaust carbon: from CO_2 to chemicals, materials, and fuels. technological use of CO_2. *Chem. Rev.,* **2014,** *114*, 1709-1742.

(39) Li, Z.; Zhi, Y.; Feng, X.; Ding, X.; Zou, Y.; Liu, X.; Mu, Y. An Azine-Linked Covalent Organic Framework: Synthesis, Characterization and Efficient Gas Storage. *Chem.Eur. J.,* **2015,** *21*, 12079-12084.

(40) Li, Z. P.; Feng, X.; Zou, Y. C.; Zhang, Y. W.; Xia, H.; Liu, X. M.; Mu, Y. A 2D azine-linked covalent organic framework for gas storage applications. *Chem. Commun.,* **2014,** *50*, 13825-13828.

(41) Alahakoon, S. B.; Thompson, C. M.; Nguyen, A. X.; Occhialini, G.;

McCandless, G. T.; Smaldone, R. A. An azine-linked hexaphenylbenzene based covalent organic framework. *Chem. Commun.,* **2016,** *52*, 2843-2845.

(42) Huang, N.; Chen, X.; Krishna, R.; Jiang, D. Two-dimensional covalent organic frameworks for carbon dioxide capture through channel-wall functionalization. *Angew. Chem. Int. Ed.,* **2015,** *54*, 2986-2990.

(43) Huang, N.; Krishna, R.; Jiang, D. Tailor-Made Pore Surface Engineering in Covalent Organic Frameworks: Systematic Functionalization for Performance Screening. *J. Am. Chem. Soc.,* **2015,** *137*, 7079-7082.

(44) Zhao, S.; Dong, B.; Ge, R.; Wang, C.; Song, X.; Ma, W.; Wang, Y.; Hao, C.; Guo, X.; Gao, Y. Channel-wall functionalization in covalent organic frameworks for the enhancement of CO_2 uptake and CO_2/N_2 selectivity. *Rsc. Adv.,* **2016,** *6*, 38774.

(45) Dong, B.; Wang, L.; Zhao, S.; Ge, R.; Song, X.; Wang, Y.; Gao, Y. Immobilization of ionic liquids to covalent organic frameworks for catalyzing the formylation of amines with CO_2 and phenylsilane. *Chem. Commun.,* **2016,** *52*, 7082-7085.

(46) FitzGerald, S. A.; Burkholder, B.; Friedman, M.; Hopkins, J. B.; Pierce, C. J.; Schloss, J. M.; Thompson, B.; Rowsell, J. L. Metal-specific interactions of H_2 adsorbed within isostructural metal-organic frameworks. *J. Am. Chem. Soc.,* **2011,** *133*, 20310-20318.

(47) Suh, M. P.; Park, H. J.; Prasad, T. K.; Lim, D. W. Hydrogen storage in metal-organic frameworks. *Chem. Rev.,* **2009,** 38, 1294-1314.

(48) Hiroyasu. Furukawa, O. M. Y. Storage of Hydrogen, Methane, and Carbon Dioxide in Highly Porous Covalent Organic Frameworks for Clean Energy Applications. *J. Am. Chem. Soc.,* **2009,** *131*, 8875-8883.

(49) Yu, J.-T.; Chen, Z.; Sun, J.; Huang, Z.-T.; Zheng, Q.-Y. Cyclotricatechylene based porous crystalline material: Synthesis and applications in gas storage. *J. Mater. Chem.,* **2012,** *22*, 5369-5373.

(50) Kahveci, Z.; Islamoglu, T.; Shar, G. A.; Ding, R.; El-Kaderi, H. M. Targeted synthesis of a mesoporous triptycene-derived covalent organic framework.

Cryst. Eng. Comm., **2013,** *15*, 1524-1527.

(51) Rabbani, M. G.; Sekizkardes, A. K.; Kahveci, Z.; Reich, T. E.; Ding, R.; El-Kaderi, H. M. A 2D mesoporous imine-linked covalent organic framework for high pressure gas storage applications. *Chem. Eur. J.,* **2013,** *19*, 3324-3328.

(52) Stephens, F. H.; Pons, V.; Tom Baker, R. Ammonia-borane: the hydrogen source par excellence? *Dalton. Trans.,* **2007**, 2613-2626.

(53) Doonan, C. J.; Tranchemontagne, D. J.; Glover, T. G.; Hunt, J. R.; Yaghi, O. M. Exceptional ammonia uptake by a covalent organic framework. *Nat. Chem.,* **2010,** *2*, 235-238.

(54) Kang, Z.; Peng, Y.; Qian, Y.; Yuan, D.; Addicoat, M. A.; Heine, T.; Hu, Z.; Tee, L.; Guo, Z.; Zhao, D. Mixed Matrix Membranes (MMMs) Comprising Exfoliated 2D Covalent Organic Frameworks (COFs) for Efficient CO_2 Separation. *Chem. Mater.,* **2016,** *28*, 1277-1285.

(55) Biswal, B. P.; Chaudhari, H. D.; Banerjee, R.; Kharul, U. K. Chemically Stable Covalent Organic Framework (COF)-Polybenzimidazole Hybrid Membranes: Enhanced Gas Separation through Pore Modulation. *Chem. Eur. J.,* **2016,** *22*, 4695-4699.

Chapter 2

Design and Synthesis of Covalent Organic Frameworks with Suitable Skeletons for Carbon Dioxide Adsorption

Chem. Commun., 2017. **53**,5147-5150.

Lipeng Zhai, Ning Huang, Hong Xu, Qiuhong Chen and Donglin Jiang

Abstract: A series of hexagonal COFs with a similar pore size but with different skeleton structures were designed and synthesized, with an aim to elucidating the design principle of the skeletons for CO_2 capture. Especially, different yet discrete contents of triarylamine units that interact weakly with CO_2 were designed and introduced into the COFs' backbones. CO_2 Adsorption experiments showed that the triarylamine units in the backbone dominate the CO_2 capture process and the CO_2 capture capacity was increased monotonically with the triarylamine content. These results clearly demonstrate a new design principle for CO_2 capture.

Keywords: carbon dioxide; covalent organic frameworks; gas adsorption; synthesis; recycle

2.1 Introduction

Carbon dioxide (CO_2) is the main component of greenhouse gas, which releases amount and its concentration in atmosphere are rapidly increasing because of the increasing global population and industrial and economical development.[1-3] As a consequence, the detrimental effects including global climate warming, rising sea level and anthropogenic climate change were happened. Therefore, developing effective technologies and design novel materials for CO_2 adsorption and sequestration is an urgent and essential task for humans.

Covalent organic frameworks (COFs) are a class of crystalline porous materials that allow precisely introduction of organic building blocks into extended order structures.[4-9] A distinct feature of COFs materials is as following: total design and control of structures including skeleton, pore size and pore shape is avalibale.[10-15] Via the changing the diversity of topologies and linkages, availability of building blocks, COFs materials have become as a molecular platform. Therefore, COFs materials have broad potential applications ranging from gas storage to catalysis, energy storage and conversion, and optoelectronics.[16-24]

Because COFs have high porosity and structural predesignablity characteristics, COFs are promising candidates as porous platfrom for CO_2 removing.[4,14] Especially, using pore-wall surface engineering could change conventional COFs into funtional COFs for improving the capture capacity by incorporating different functional groups such as carboxylic acid and alkyl amine to the pore surface that have strong interactions with CO_2 molecule.[25-27] Although various linkages were reported, only azine linkage[28] exhibited a potential application in increasing the CO_2 capture capacity.[29-32] Even though great progress in designing COFs materials, a principle using COFs' backbone design aiming for CO_2 capture is still remaining to be explored. In this research work, I succeeded in introducing triarylamine that has very weak basicity in enhancing CO_2 interaction as a building block to the COFs' backbone and elucidated its possible effect on CO_2 adsorption.

2.2 Results and Discussions

2.2.1 Synthesis and Structural characterizations

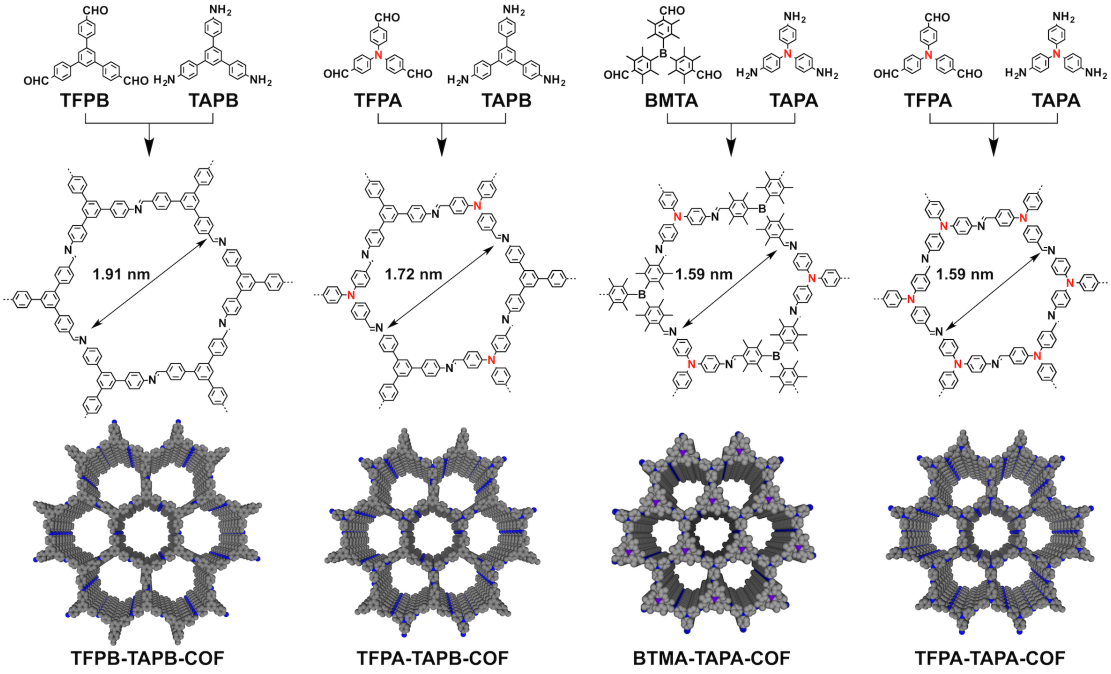

Figure 1. Schematic of COFs with different yet discrete content of triarylamine units

I designed four imine-linked COFs with similar hexagonal topology and similar micro-pore size with tris(4-formylphenyl)amine (TFPA) and tris(4-aminophenyl)amine (TAPA) as triarylamine building blocks. Using 4,4',4"-boranetriyltris (2,3,5,6-tetramethylbenzaldehyde) (BTMA, Figure 11 and 12) and 1,3,5-tris(4-formylphenyl) benzene (TFPB), 1,3,5-tris(4-aminophenyl)benzene (TAPB) as non-triarylamine units to synthesis different COFs materials. Co-condensation of monomer TFPB and TAPB could form TFPB-TAPB-COF without triarylamine organic units in the COFs' backbone. Using TFPA with TAPB or BTMA or TFPA with TAPA could produce TFPA-TAPB-COF or BTMA-TAPA-COF or TFPA-TAPA-COF with three and six triarylamine organic units in the hexagon skeleton, respectively (Figure 1). The polycondensation reactions were done under solvothermal conditions using the mixture of mesitylene and 1,4-dioxane as solvent for TFPB-TAPB-COF, TFPA-TAPB-COF and TAPA-TFPA-COF and

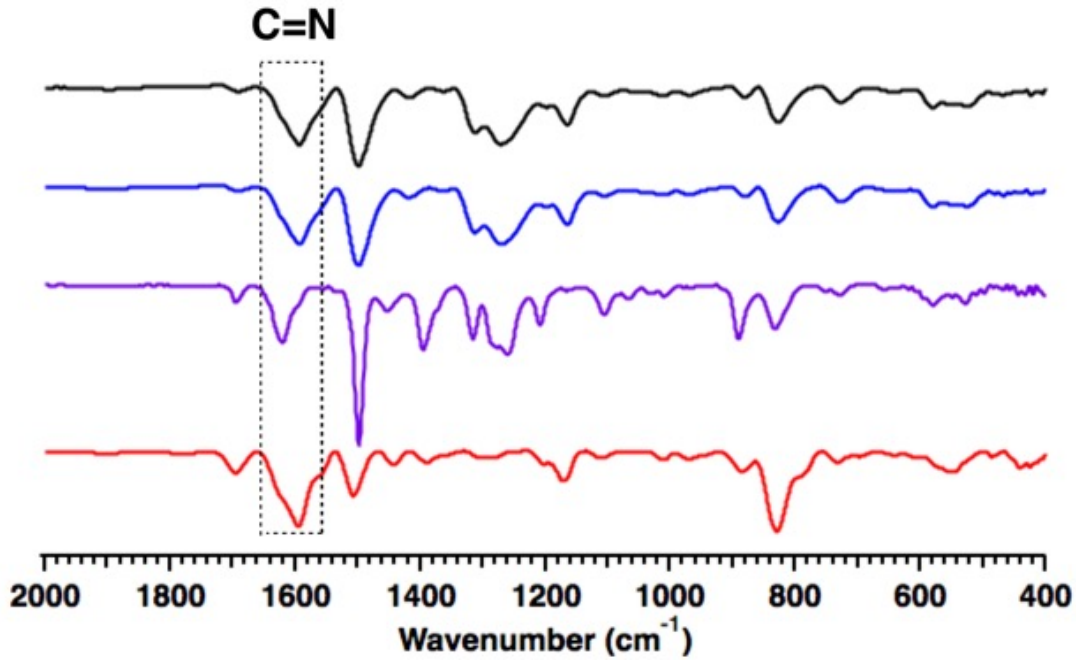

Figure 2 . FT-IR spectra of TFPB-TAPB-COF (black), TFPA-TAPB-COF (blue), BTMA-TAPA-COF (purple) and TFPA-TAPA-COF (red).

o-dichlorobenzene (*o*-DCB) and *n*-butanol for BTMA-TAPA-COF via acetic acid as catalyst heating at 120 °C for 3 days. The yields of TFPB-TAPB-COF, TFPA-TAPB-COF, BTMA-TAPA-COF and TFPA-TAPA-COF were 87%, 84%, 78% and 85%, respectively. Infrared spectroscopy (IR) showed stretching vibration bands at 1625 $cm^{-1.}$ This IR peak were attributed to the C=N bond (Figure 2). Element analysis (EA) results are similar with the theoretical values. Thermal gravimetric analysis (TGA) showed that these COFs are stable in N_2 atmosphere until 400 °C (Figure 3).

2.2.2 PXRD pattern and Theoretical Calculation

Powder X-ray diffraction (PXRD) measurements as well as computational structural simulations calculation and Pawley refinements were used to simulate crystal structures of TFPB-TAPB-COF, TFPA-TAPB-COF, BTMA-TAPA-COF and TFPA-TAPA-COF. TFPB-TAPB-COF had five main PXRD diffraction peaks at 3.92°, 6.78°, 10.38°, 14.24° and 24.88°. These peaks were attributed to the (100), (110), (210), (310) and (001) facets, respectively (Figure 4a, green curve). TFPA-TAPB-COF had PXRD peaks at 4.46°, 7.58°, 10.24°, 16.8° and 24.62°. These PXRD peaks could be attributed to the (100),

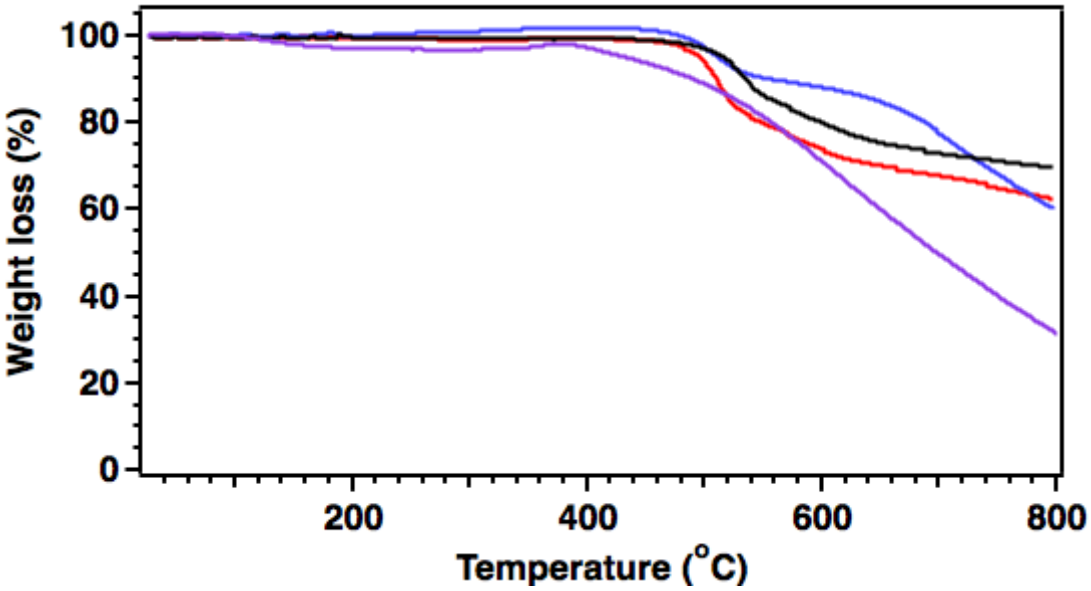

Figure 3. TGA curve of TFPB-TAPB-COF (black curves), TFPA-TAPB-COF (blue curves), BTMA-TAPA-COF (purple curves) and TFPA-TAPA-COF (red curves)

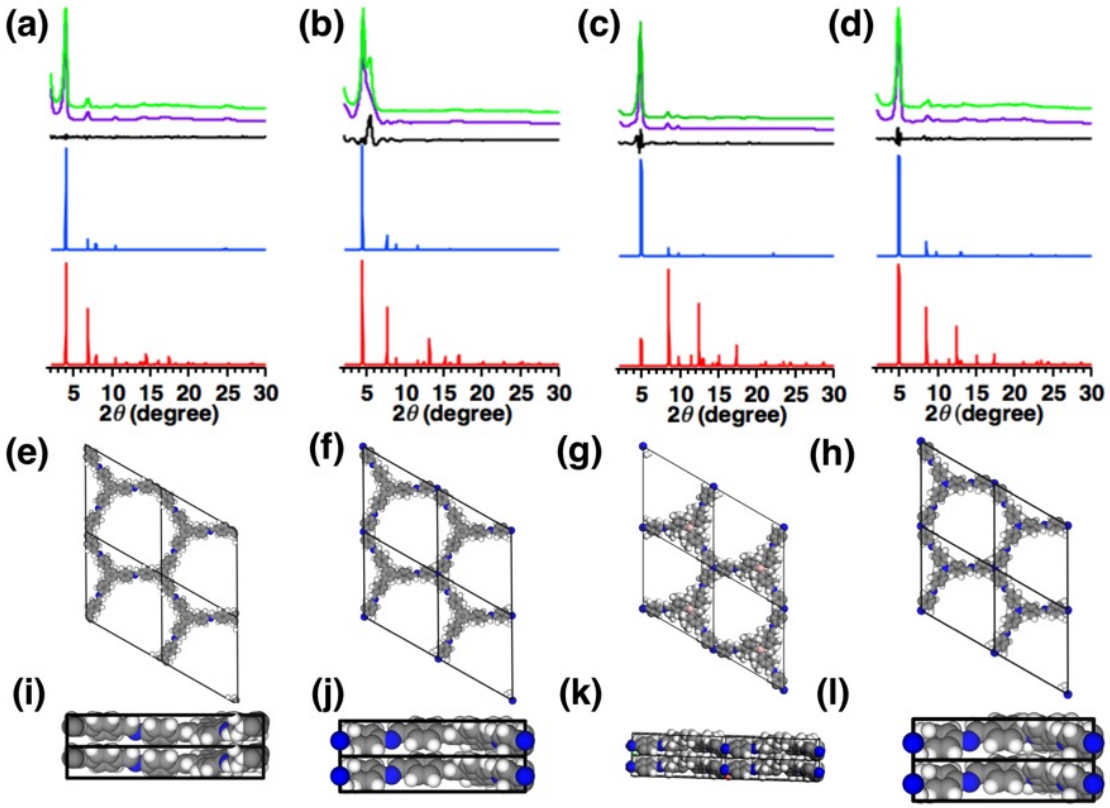

Figure 4. PXRD patterns of **(a)** TFPB-TAPB-COF, **(b)** TFPA-TAPB-COF, **(c)** BTMA-TAPA-COF and **(d)** TFPA-TAPA-COF (green for the experimentally observed, purple for Pawley refinement, black for their difference, blue for simulated using AA and red for AB-stacking modes. Top **(e-h)** and side **(i-l)** views of the unit cell of **(e, i)** TFPB-TAPB-COF, **(f, j)** TFPA-TAPB-COF, **(g. k)** BTMA-TAPA-COF and **(h. l)** TFPA-TAPA-COF

(110), (210), (310) and (001) facets, respectively (Figure 4b, green curve). BTMA-TAPA-COF had PXRD diffraction peaks at 4.89°, 8.47°, 9.78°, 12.94°, 16.98° and 25.32°. These peaks were attributed to the (100), (110), (200), (210), (220) and (001) Facets, respectively (Figure 4c, green curve). TFPA-TAPA-COF showed similar PXRD peaks at 4.78 °, 8.68 °, 9.92°, 13.64° and 21.76°. These peaks were attributed to the (100), (110), (200), (300) and (001) Facets, respectively (Figure 4d, green curve). Figure 5 summarizes the assignments' details of the PXRD patterns for these COFs materials.

Using pawley refinements method could yielded PXRD patterns (Figure 4a-d, purple curves), which were similar with the experimentally observed curves. Their negligible difference (Figure 4a-d, black curves) confirmed this. The conformation of single layer and the configuration of different stacking modes by using density functional theory tight binding (DF-TB) calculations were optimized. Table 1-12 concludes all the atomistic coordinates for these COFs materials. After calculation, AA-stacking mode (Figure 4e-l) is the energetically most stable among various

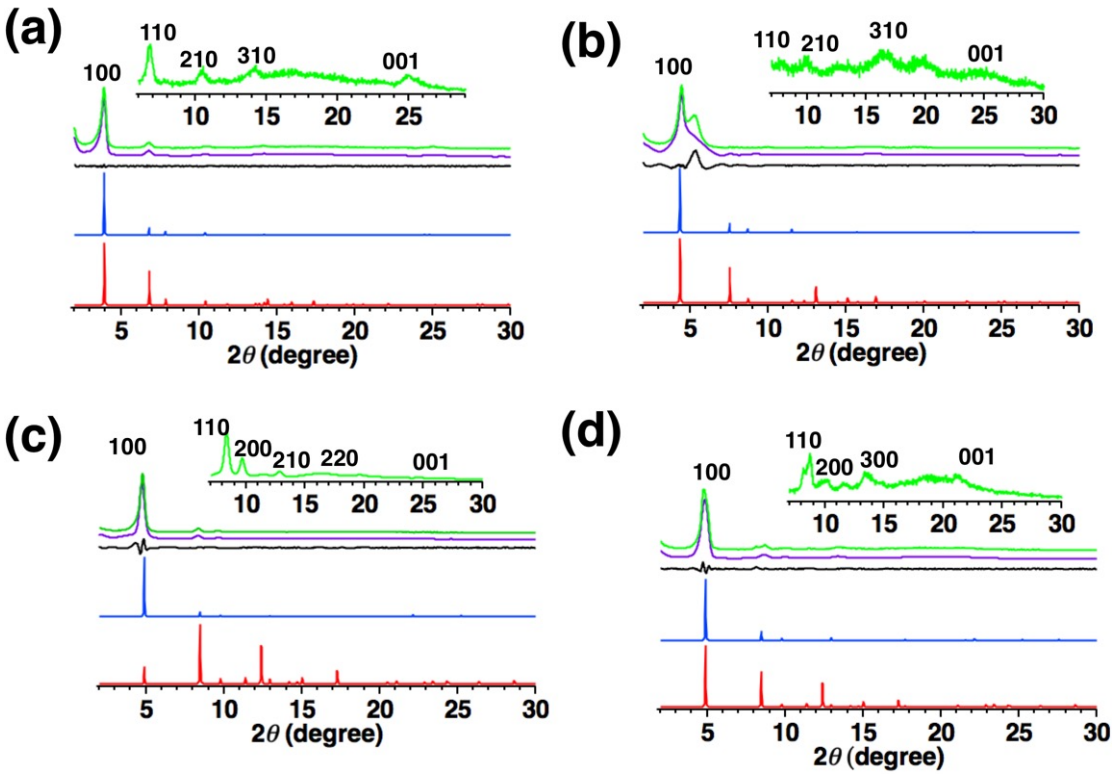

Figure 5. PXRD assignments of **(a)** TFPB-TAPB-COF, **(b)** TFPA-TAPB-COF, **(c)** BTMA-TAPA-COF and **(d)** TFPA-TAPA-COF. The originality of the shoulder peak around 6° in **(b)** is unclear

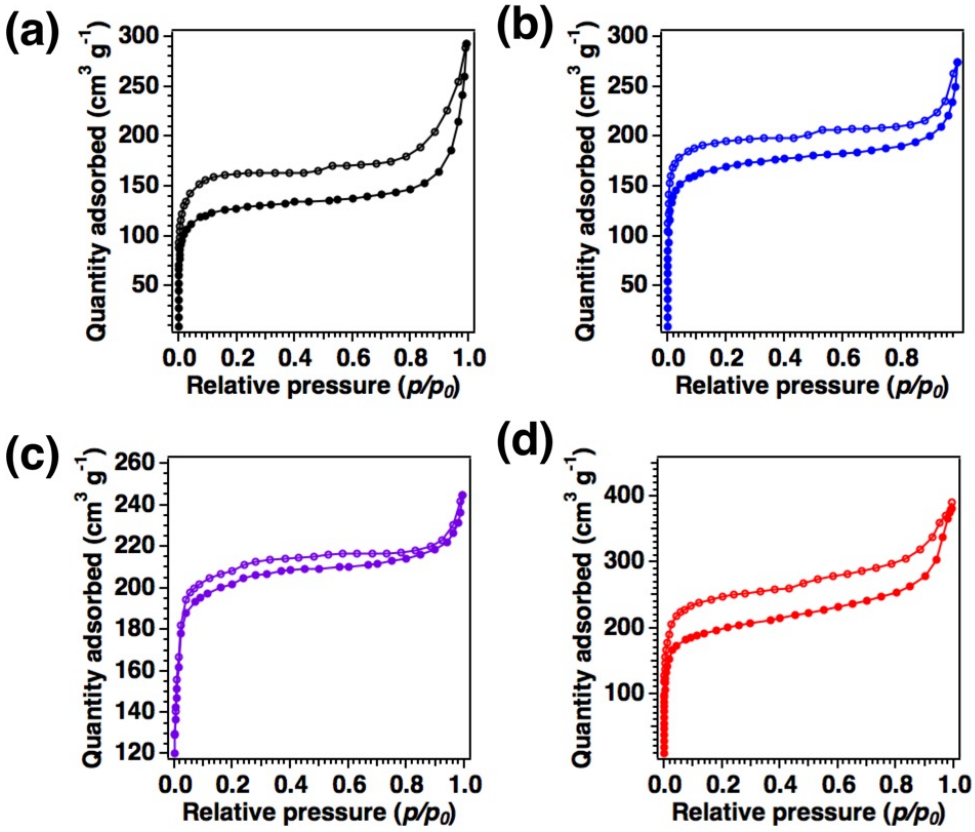

Figure 6. Nitrogen sorption isotherms measured at 77 K of **(a)** TFPB-TAPB-COF, **(b)** TFPA-TAPB-COF, **(c)** BTMA-TAPA-COF and **(d)** TFPA-TAPA-COF.

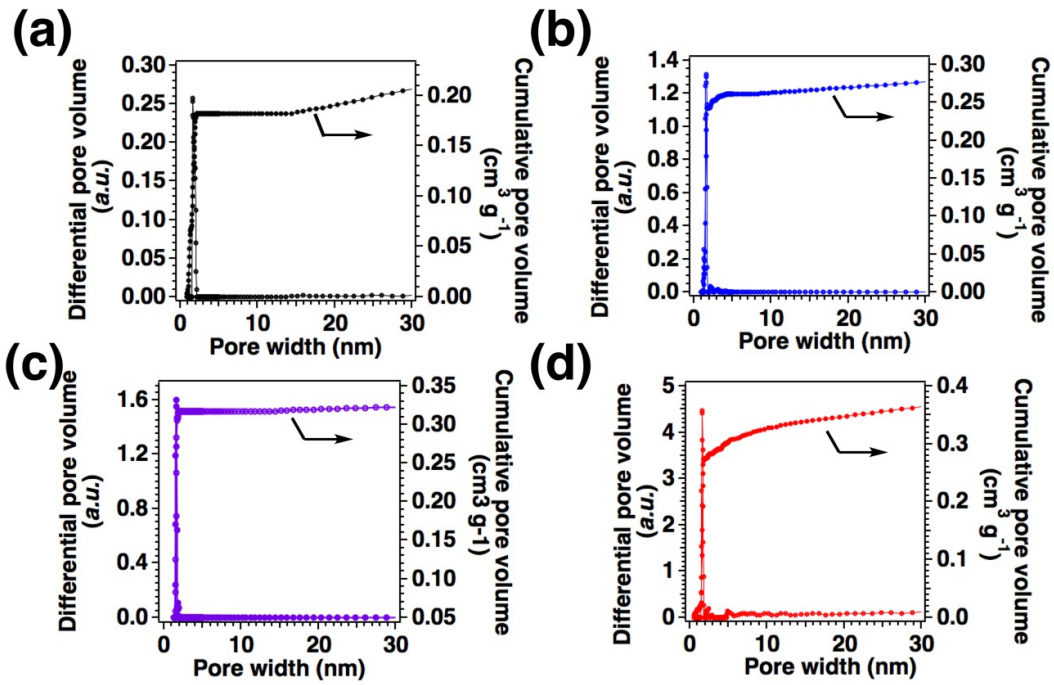

Figure 7. Pore size distribution and cumulative pore volume of **(a)** TFPB-TAPB-COF, **(b)** TFPA-TAPB-COF, **(c)** BTMA-TAPA-COF and **(d)** TFPA-TAPA-COF.

stacking modes (AA and AB stacking). AA stacking mode yields PXRD patterns (Figure 4a-d, blue curves), which are similar with the experimentally observed curves. On contrast, the AB-stacking mode produces PXRD curves (Figure 4a-d, red curves) that are different from the observed experimental PXRD profiles. Thus, these COFs materials adopt AA-stacking mode and have crystal structures, whose aligned vertices and linkers where the triarylamine units can be accessible to external guest gas molecules (Figure 4e-l).

2.2.3 Porosity Property

TFPB-TAPB-COF, TFPA-TAPB-COF, BTMA-TAPA-COF and TFPA-TAPA-COF possess 1D open pore channels, which were determined through the crystal structures of COFs materials,. Their porosities were determined using nitrogen sorption isotherms at 77 K. Typically, All these COFs materials showed type I sorption profiles (Figure 6), which are typically microporous materials. The Brunauer-Emmett-Teller (BET) surface area of 410, 540, 630 and 660 $m^2 g^{-1}$ with pore volume of 0.19, 0.25, 0.32 and 0.32 $cm^3 g^{-1}$ (Figure 7) for TFPB-TAPB-COF, TFPA-TAPB-COF, BTMA-TAPA-COF and TFPA-TAPA-COF, respectively. Moreover, their pore sizes were changed from 1.91, 1.72 1.59 to 1.59 nm, respectively (Figure 7) according to the their pore size distribution, which was calculated according to the nonlocal density

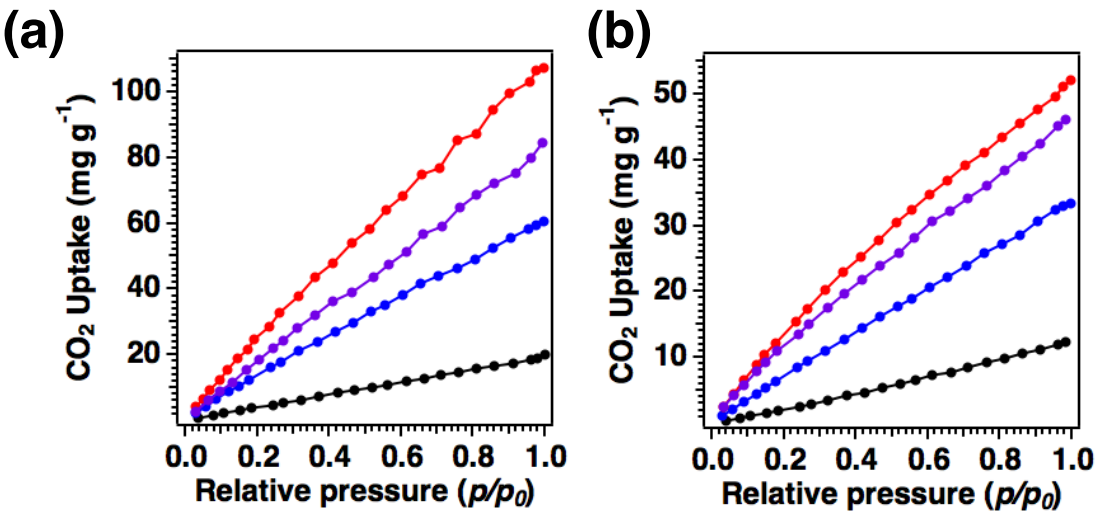

Figure 8. CO_2 uptake at **(a)** 273 K and **(b)** 298 K (black for TFPB-TAPB-COF, blue for TFPA-TAPB-COF, purple for BTMA-TAPA-COF and red for TAPA-TFPA-COF.

functional theory method.

2.2.4 CO_2 Adsorption Property

CO_2 capture properties were investigated at 273 K (Figure 8a) and 298 K (Figure 8b) up to 1 bar. TFPB-TAPB-COF without organic triarylamine units within the COFs' backbone showed CO_2 adsorption capacities of 12 and 20 mg g^{-1} at 298 and 273 K, respectively (Figure 8a, b, black curves). This result reveals that the imine-linked COFs' backbone is not suitable for CO_2 capture. In contrast, TFPA-TAPB-COF having three triarylamine building units in the hexagon topology pore channel showed greatly improved CO_2 capture capacities of 33 and 61 mg g^{-1} at 298 and 273 K, respectively (Figure 8a, b, blue curves). TFPA-TAPB-COF' capacities are 2.5 fold those of TFPB-TAPB-COF. BTMA-TAPA-COF having three organic triarylamine units in the hexagon toology pore channel showed enhanced CO_2 adsorption properties of 45 and 84 mg g^{-1} at 298 and 273K (Figure 8a, b, purple curves). Interestingly, TFPA- TAPA-COF having six triarylamine organic units in the skeleton showed CO_2 uptake capacities of 52 and 105 mg g^{-1} at 298 and 273 K, respectively (Figure 8 a, b, red curves). These capacities of TFPA- TAPA-COF are almost 1.25 fold BTMA-TAPA-COF, two fold TFPA-TAPB-COF and four fold of TFPB-TAPB-COF's capacities as well. Moreover, because BTMA-TAPA-COF and TAPA-TFPA-COF have similar pore size and pore volume. Therefore, the improved CO_2 capture capacity investigated for TAPA-TFPA-COF exhibits that the triarylamine units in the COFs' backbone exhibited a positive effect on improving the CO_2 uptake properties.

Based on the nitrogen sorption profiles at 273 and 298 K (Figure 9), the CO_2/N_2 selectivity at 273 K for TFPB-TAPB-COF, TFPA-TAPB-COF, BTMA- TAPA-COF and TFPA-TAPA-COF was determined to be 5, 13, 16.8 and 21, respectively. Furthermore, the CO_2/N_2 selectivity at 298 K was 6, 14, 18 and 21 for TFPB-TAPB-COF, TFPA-TAPB-COF, and BTMA-TAPA-COF, which were similar with the selectivity at 273K. and TFPA-TAPA-COF, respectively. The selectivity tendencies increased with the increasing triarylamine contents, which showed the triarylamine organic

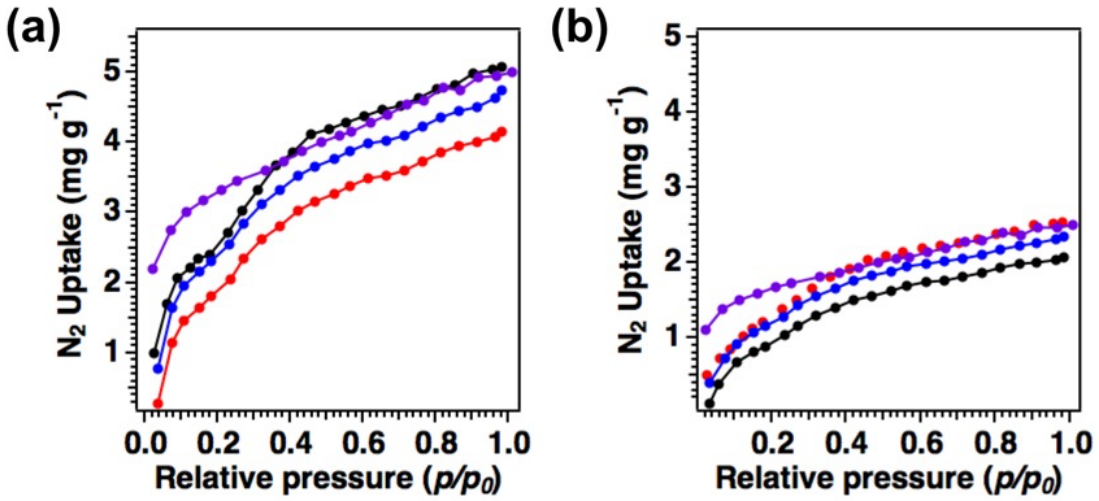

Figure 9. Nitrogen adsorption isotherm curves of TFPB-TAPB-COF (black curve), TFPA-TAPB-COF (blue curve), BTMA-TAPA-COF (purple curve) and TFPA-TAPA-COF (red curve) at **(a)** 273 K and **(b)** 298 K

units have an important role in the adsorption properties of CO_2.

TFPA-TAPA-COF showed outstanding cycling performance without any decrease in uptake capacity over ten cycles at 273K (Figure 10). To further understanding the interaction of these four COFs materials to CO_2 gas molecule, the isosteric heat of adsorption (Q_{st}) was calculated according to the Clausius-Clapeyron equation based on the adsorption data collected at 298 and 273 K. The Q_{st} values of TFPB-TAPB-COF, TFPA-TAPB-COF, BTMA-TAPA-COF and TFPA-TAPA-COF are 17.7, 21.1, 24.6 and 28.4 kJ mol^{-1} at zero coverage,, respectively. The Q_{st} values showed that the backbones of COFs with more triarylamine units have stronger interactions to CO_2 gas molecule. Due to the same pore size and pore volume, BTMA-TAPA-COF has lower Q_{st} than that of TFPA-TAPA-COF, which showed that the COFs' backbones having more triarylamine units produce stronger interactions toward gas CO_2 molecule.

COFs' molecular building blocks design for CO_2 capture has been mainly worked on the pore surface functionalization. The results demonstrated that the

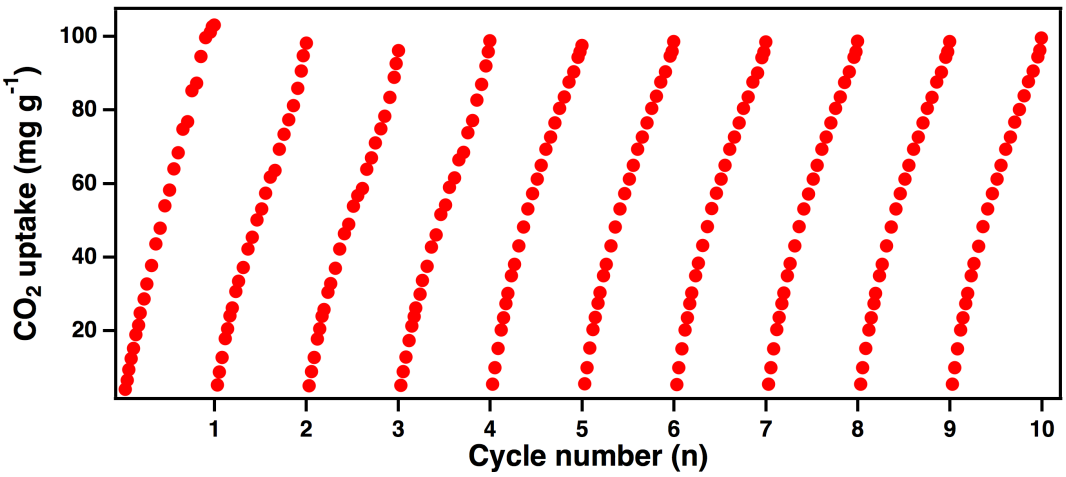

Figure 10. CO_2 uptake cycling performance of TFPA-TAPA-COF at 273 K

COFs' backbone has an important role in CO_2 uptake properties. The triarylamine backbones' collective effect is important and could not be overlooked. Considering the availability of organic building blocks with strong basicity, the results in this work showed an easy protocol for the COFs' backbone design using for CO_2 capture and separation.

2.3 Experimental Sections

2.3.1 Methods

I used JASCO model named FT-IR-6100 infrared spectrometer machine to investigated FT-IR spectra for COFs materials. Also, I use Rigaku model RINT Ultima III diffractometer depositing COFs materials smaple powder on the glass substrate. The angle increased from 1.5° up to 60° with 0.02° increment for COFs materials to Powder X-ray diffraction (PXRD) data. Mettler-Toledo model TGA/SDTA851e was applied for COFs materials. TGA measurements in N_2 atmosphere. Moreover, heat the COFs materials to 800 °C at a rate of 10 °C min^{-1}. Bel Japan Inc was used for COFs materials.Nitrogen sorption isotherms measurement at 77 K. The COFs materials were dried under oil vacuum at 120 °C more than 12 h before measurement. The COFs materials pore size distribution and volume was calculated acoording to the traditional non-local density functional theory (NLDFT) method.

The isosteric heat, Q_{st}, defined as Q_{st} = RT^2

$(\frac{\partial lnp}{\partial T})_q$ ……..1

were detemined acoording to the pure component isotherm fits based on the Clausius-Clapeyron equation.

I used the density-functional tight-binding (DFTB+) methodology to investigate the COFs materials crystalline structures with Lennard-Jones (LJ) dispersion. I also use the DFTB+ program package 1.2 version for COFs materials In this research work. [33] The self-consistent charge (SCC) formalism was used to reveal the COFs materials Coulombic interaction between among partial atomic charges. And the Lennard-Jones type dispersion was applied for COFs materials in all these calculations, which exhibited van der Waals (vdW) and π-π stacking interactions. Using geometry to optimize the lattice dimensions of COFs materials. The different Standard of DFTB parameters from the mio-0-1 set for variety X–Y element pair (X, Y = C, S, H and N) interactions were applied for COFs materials. [34]

I used Reflex for organic molecular modeling and COFs' Pawley refinements, and crystal determination according to the PXRD pattern. This was implemented in MS modeling 4.4version (Accelrys Inc.).[35] Firstly, for hexagonal lattices, unit cell dimensions were calculated based on the DFTB calculation. The *P*3 were selected as space group for hexagonal crystal system respectively. the lattice parameters were optimized using pawley refinements for hexagonal lattice to optimize iteratively until. s. The final R_{WP} = 15.60%; R_P = 12.77% for BTMA-TAPA-COF and R_{WP} = 9.90%; R_P = 7.65% for TFPA-TAPA-COF, respectively. R_{WP} = 9.56% and R_P = 6.56% for TFPB-TAPB-COF, R_{WP} = 21.7% and R_P = 15.08% for TFPA-TAPB-COF

2.3.2 Materials and Synthetic Procedures

o-DCB, Mesitylene, n-BuOH, tetrahydrofuran (THF), and 1,4-dioxane were bought from Wako chemicals company. tris(4-formylphenyl)amine(TFPA), 1,3,5-tris(4-aminophenyl)benzene (TAPB), Tris(4-aminophenyl)amine(TAPA), and AcOH were purchased from TCI. 1,3,5-Tris (4-formylphenyl)benzene (TFPB) was synthesized according to literature.[36] Tris(bromoduryl)borane monomer was synthesized according to literature.[37]

Synthesis of 4,4',4''-boranetriyltris(2,3,5,6-tetramethylbenzaldehyde) (BTMA).

A hexane solution t-BuLi (1.6 M, 5 mL, 7.5mmol) was added dropwisely to the anhydrous THF solution (200 mL) of tris(bromoduryl)borane (5 g, 9 mmol) at –78 ^{o}C. The reaction system was stirred for 2 h at room temperature. Then 25ml anhydrous DMF was added at –78 ^{o}C. The reaction system was warmed to room temperature and then stirred overnight about 12 hours. Then Using concentrated HCl to charge the reaction system mixture. Then, the reaction mixture was stirred at room temperature for anther 2 h. Then 100ml water was added into the reaction system. Using 4x 80ml CH_2Cl_2 to extract the mixture. The extract organic solvent was combined and collects the crude product under reduced pressure. The crude product was purified using a mixture of CH_2Cl_2 and hexane (1:1 to 3:1) as eluent through silica column chromatography. 4,4',4''-boranetriyltris(2,3,5,6-tetramethylbenzaldehyde) was offered as a white solid (1100 mg, 27% yield). ^{1}HNMR ($CDCl_3$): 10.64 (s, 3H), 2.28 (s, 18H) and 1.97 (s, 18H).

TFPB-TAPB-COF

A mixture of TFPB (0.048 mmol, 18.9 mg) and TAPB (0.048 mmol, 17 mg) using AcOH (6 M, 0.1mL) as catalyst and mesitylene/1,4-dioxane (0.9 mL/0.1 mL) as solvent in a 10ml-Pyrex tube. The reaction tube was degassed by three freeze-pump-thaw cycles to remove the oxygen. Then the reaction tube was sealed by flame gun. The reaction mixture tube was heated at 120 °C for 3 days using oven. The COF solid was collected through centrifuge and was washed with THF for 6 times (each time 2ml). The COF powder was dried at 120 °C under vacuum about 8 hours to obtain the TFPB-TAPB-COF in 87% yield. Elemental analysis calcd for TFPB-TAPB-COF: C, 88.44; H, 5.35; N, 6.07. Found: C, 86.16; H. 5.22; N, 5.39.

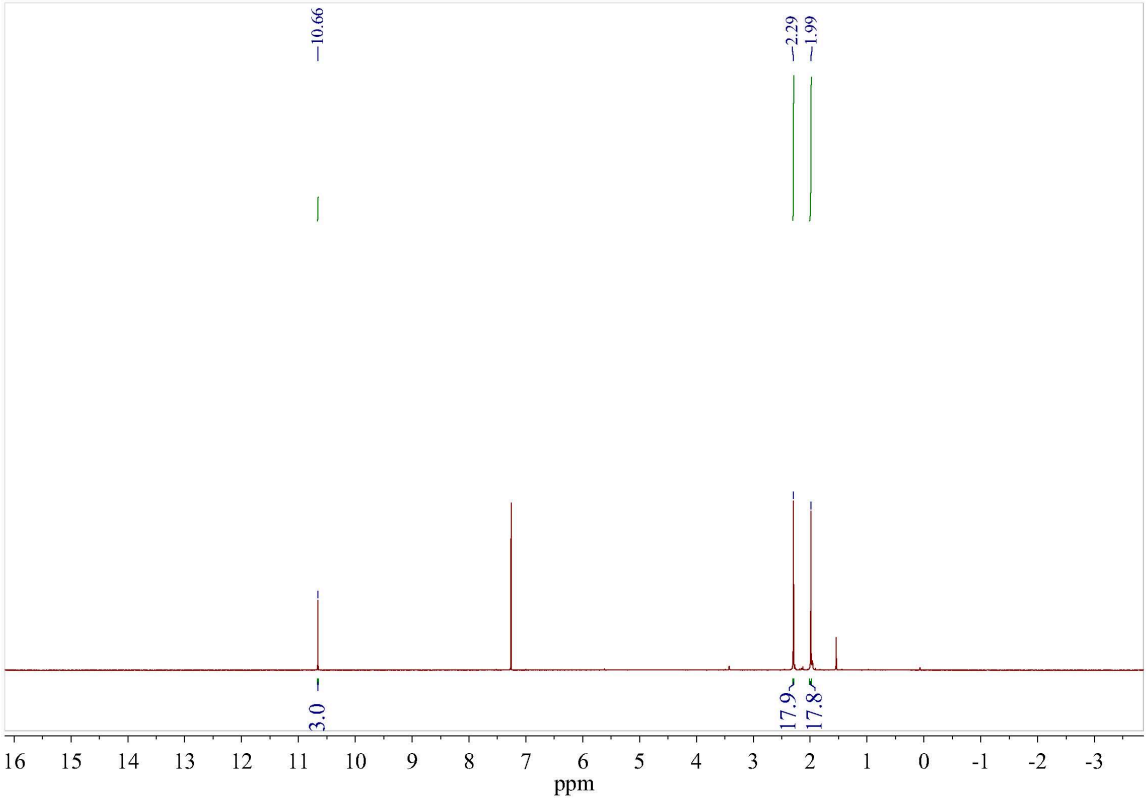

Figure 11. ^{1}HNMR of 4,4',4"-boranetriyltris(2,3,5,6-tetramethylbenzaldehyde, BTMA) ($CDCl_3$)

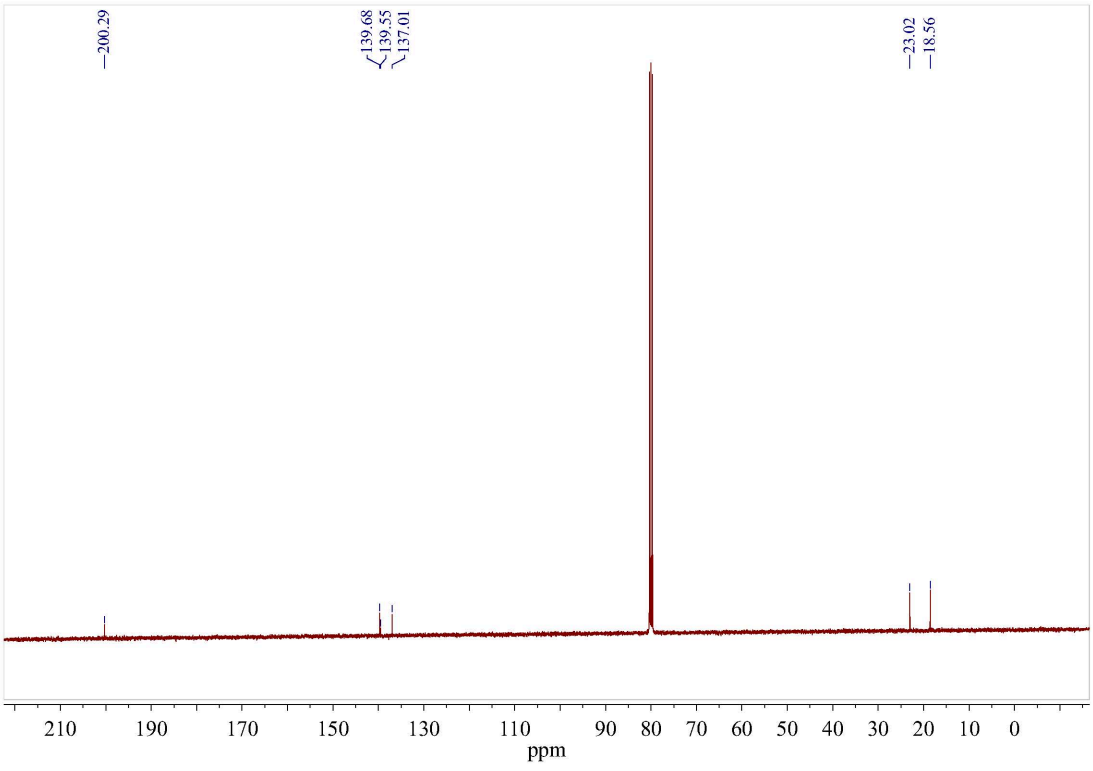

Figure 12. ^{13}C NMR of 4,4',4"-boranetriyltris(2,3,5,6-tetramethylbenzaldehyde, BTMA) ($CDCl_3$)

TFPA-TAPB-COF

A mixture of monomer TAPB (0.048 mmol, 17 mg) and TFPA (0.048 mmol, 15.94 mg) using AcOH (6 M, 0.1 mL) as catalyst and 1,4-dioxane/mesitylene (0.5 mL/0.5 mL) as solvent in a 10ml-Pyrex tube. The reaction tube was degassed by three freeze-pump-thaw cycles to exclude the oxygen. Then the reaction tube was sealed by flame gun. The reaction mixture tube was heated at 120 °C for 3 days. The COF solid was collected through centrifuge. The COF sample was washed with THF for 6 times (each time 2ml). The COF powder was dried to remove solvent at 120 °C under vacuum about 8 hours to give the TFPA-TAPB-COF in 84% yield. Elemental analysis calcd for TFPB-TAPB-COF: C, 85.71; H, 5.39; N, 7.61. Found: C, 83.69; H. 4.85; N, 8.41.

BTMA-TAPA-COF

An mixture of monomer TAPA (17.8 mg, 0.0617 mmol) and BTMA (30.37 mg, 0.0617 mmol) in using AcOH as catalyst (6 M, 0.1 mL) and *o*-DCB/n-BuOH (0.5 mL/0.5 mL) as solvent in a 10ml-Pyrex tube. The reaction tube was degassed by three freeze-pump-thaw cycles. The reaction tube was sealed by flame gun. Then the tube was heated at 120 °C for 3 days. The COF solid was collected through centrifuge. The COF solid was washed with THF for 6 times (each time 2ml). The COF powder was dried to remove solvent at 120 °C under vacuum around 8 hours to give the BTMA-TAPA-COF in 78% yield. Elemental analysis calcd for TFPA-TFPB-COF: C, 83.84; H, 6.99; N, 7.67. Found: C, 81.57; H, 5.68; N, 7.34.

TFPA-TAPA-COF

A mixture of monomer TAPA (0.049 mmol, 14.1 mg) and TFPA (0.048 mmol, 15.94 mg) using AcOH (6 M, 0.1 mL) as catalyst and 1,4-dioxane/ mesitylene (0.5 mL/0.5 mL) as solvent in a 10ml-Pyrex tube. The reaction tube was degassed by three freeze-pump-thaw cycles. The tube was sealed by flame gun. The reaction mixture tube was heated at 120 °C for 3 days. The COF solid was collected through centrifuge and the COF solid was washed with THF for 6 times (each time 2ml). The COF powder was dried to remove solvent at 120 °C under oil vacuum about 8 hours

to obtain the TFPA-TAPA-COF in 85% yield. Elemental analysis calcd for TFPB-TAPB-COF: C, 82.75; H, 5.44; N, 12.88. Found: C, 79.22; H. 3.89; N, 11.44.

2.4 Atomistic coordinates

Table 1. Atomistic coordinates for the AA-stacking mode of TFPB-TAPB-COF optimized by using DFTB+ method. Space group: *P*3*; a* = 26.0324 Å, *b* = 26.0324 Å, and *c* = 3.6329 Å.

Atom	*x/a*	*y/b*	*z/c*
C	2.26456	2.82035	0.34858
C	2.29494	2.78951	0.33548
C	2.26886	2.73077	0.46047
C	2.21047	2.70421	0.59277
C	2.1795	2.73449	0.60274
C	2.20648	2.79378	0.48562
C	2.30197	2.69774	0.45481
C	2.27181	2.63577	0.45448
N	2.64962	2.82033	0.48383
C	3.09128	3.226	0.50235
C	3.05551	3.16506	0.49663
C	3.07555	3.12784	0.63497
C	3.13327	3.15455	0.77787
C	3.1692	3.21552	0.78291
C	3.14892	3.25249	0.64562
C	3.03669	3.06206	0.63223
C	2.97498	3.03618	0.63205
C	3.13016	2.813	0.65488
H	2.28576	2.86612	0.24944
H	2.33962	2.81162	0.21776
H	2.18848	2.65877	0.69867
H	2.13401	2.7114	0.70749
H	2.22332	2.61138	0.45511
H	3.07485	3.25417	0.39098
H	3.01136	3.14621	0.37365
H	3.15039	3.12749	0.89736
H	3.21387	3.23499	0.89987
H	2.95527	3.0647	0.63236
H	3.10563	2.77081	0.81586

Table 2. Atomistic coordinates for the refined unit cell parameters for TFPB-TAPB-COF via Pawley refinement. Space group: *P*3*; a* = 26.0077 Å, *b* = 26.0077 Å, and *c* = 3.6347 Å.

Atom	***x/a***	***y/b***	***z/c***
C	2.26456	2.82035	0.34858
C	2.29494	2.78951	0.33548
C	2.26886	2.73077	0.46047
C	2.21047	2.70421	0.59277
C	2.1795	2.73449	0.60274
C	2.20648	2.79378	0.48562
C	2.30197	2.69774	0.45481
C	2.27181	2.63577	0.45448
N	2.64962	2.82033	0.48383
C	3.09128	3.226	0.50235
C	3.05551	3.16506	0.49663
C	3.07555	3.12784	0.63497
C	3.13327	3.15455	0.77787
C	3.1692	3.21552	0.78291
C	3.14892	3.25249	0.64562
C	3.03669	3.06206	0.63223
C	2.97498	3.03618	0.63205
C	3.13016	2.813	0.65488
H	2.28576	2.86612	0.24944
H	2.33962	2.81162	0.21776
H	2.18848	2.65877	0.69867
H	2.13401	2.7114	0.70749
H	2.22332	2.61138	0.45511
H	3.07485	3.25417	0.39098
H	3.01136	3.14621	0.37365
H	3.15039	3.12749	0.89736
H	3.21387	3.23499	0.89987
H	2.95527	3.0647	0.63236
H	3.10563	2.77081	0.81586

Table 3. Atomistic coordinates for the AB-stacking mode of TFPB-TAPB-COF optimized by using DFTB+ method. Space group: *P*3*; a* = 25.9516 Å, *b* = 25.9516 Å, and *c* = 6.3891 Å.

Atom	*x/a*	*y/b*	*z/c*
C	0.25086	0.80492	0.00839
C	0.27908	0.77163	0.00833
C	0.27543	0.73747	0.18289
C	0.24367	0.73792	0.35881
C	0.21532	0.77111	0.36023
C	0.21777	0.80408	0.18286
C	0.30549	0.70086	0.18225
C	0.27147	0.6389	0.18223
N	0.64887	0.80895	0.17686
C	0.0863	0.22537	0.16224
C	0.05162	0.16411	0.16178
C	0.07225	0.12843	0.25135
C	0.12902	0.15674	0.34209
C	0.16374	0.21802	0.34322
C	0.14304	0.25346	0.25309
C	0.03504	0.06232	0.25004
C	0.97303	0.03465	0.24989
C	0.13826	0.81976	0.25354
H	0.25316	0.83096	-0.12953
H	0.30417	0.77185	-0.1297
H	0.24155	0.71221	0.49766
H	0.19195	0.77205	0.50154
H	0.22287	0.61707	0.18243
H	0.06953	0.2524	0.09028
H	0.00778	0.14384	0.08798
H	0.14673	0.13069	0.41458
H	0.2078	0.23882	0.41636
H	0.9518	0.06194	0.24985
H	0.11133	0.77373	0.31929
C	0.93793	0.15908	0.66745
C	0.96657	0.12625	0.66449
C	0.94017	0.06903	0.75186
C	0.88361	0.04607	0.84178
C	0.85504	0.07894	0.84912
C	0.88234	0.13641	0.76421
C	0.97097	0.03348	0.74929
C	0.93828	0.97133	0.74917

N	0.3168	0.14609	0.75869
C	0.75994	0.55639	0.74102
C	0.72885	0.49483	0.73766
C	0.73092	0.4624	0.90908
C	0.76429	0.49299	1.08485
C	0.79454	0.55457	1.08966
C	0.79318	0.58727	0.91736
C	0.69763	0.39553	0.90578
C	0.63554	0.36419	0.90569
C	0.82625	0.17355	0.9229
H	0.95941	0.2036	0.59851
H	0.01023	0.14565	0.58963
H	0.861	1.00142	0.90945
H	0.81066	0.05918	0.91886
H	0.88967	0.9487	0.74906
H	0.75843	0.5814	0.6054
H	0.70291	0.47139	0.59899
H	0.76606	0.46818	1.22054
H	0.82004	0.57779	1.22953
H	0.61109	0.38843	0.90638
H	0.82575	0.15175	1.07491

Table 4. Atomistic coordinates for the AA-stacking mode of TFPA-TAPB-COF optimized by using DFTB+ method. Space group: *P*3*; a* = 23.4586 Å, *b* = 23.4586 Å, and *c* = 3.8991 Å.

Atom	***x/a***	***y/b***	***z/c***
C	-0.13052	-0.17467	0.30775
C	-0.09667	-0.10678	0.29438
C	-0.03459	-0.07013	0.44937
C	-0.00766	-0.10487	0.61074
C	-0.04109	-0.1728	0.62013
C	-0.10396	-0.20927	0.47314
N	-0.13546	0.14292	0.46933
C	0.4164	0.18581	0.47434
C	0.48406	0.21405	0.46698
C	0.52486	0.27475	0.62632
C	0.49507	0.30611	0.79253
C	0.42736	0.27787	0.80043
C	0.38671	0.21718	0.64162
C	0.59786	0.30492	0.62192
C	0.62673	0.26531	0.62164
C	-0.12771	-0.31495	0.65322
H	-0.17873	-0.20216	0.18476
H	-0.11887	-0.08211	0.15764
H	0.04026	-0.07848	0.73652
H	-0.01765	-0.19706	0.74994
H	0.38538	0.13867	0.34601
H	0.50552	0.18889	0.32669
H	0.52507	-0.6473	0.92758
H	0.40542	0.30309	0.93632
H	0.59526	0.21173	0.62215
H	-0.08388	-0.29507	0.82666
N	0	0	0.44289

Table 5. Atomistic coordinates for the refined unit cell parameters for TFPA-TAPB-COF via Pawley refinement. Space group: *P*3*; a* = 23.4694 Å, *b* = 23.4694 Å, and *c* = 3.8935 Å.

Atom	***x/a***	***y/b***	***z/c***
C	-0.13052	-0.17467	0.30775
C	-0.09667	-0.10678	0.29438
C	-0.03459	-0.07013	0.44937
C	-0.00766	-0.10487	0.61074
C	-0.04109	-0.1728	0.62013
C	-0.10396	-0.20927	0.47314
N	-0.13546	0.14292	0.46933
C	0.4164	0.18581	0.47434
C	0.48406	0.21405	0.46698
C	0.52486	0.27475	0.62632
C	0.49507	0.30611	0.79253
C	0.42736	0.27787	0.80043
C	0.38671	0.21718	0.64162
C	0.59786	0.30492	0.62192
C	0.62673	0.26531	0.62164
C	-0.12771	-0.31495	0.65322
H	-0.17873	-0.20216	0.18476
H	-0.11887	-0.08211	0.15764
H	0.04026	-0.07848	0.73652
H	-0.01765	-0.19706	0.74994
H	0.38538	0.13867	0.34601
H	0.50552	0.18889	0.32669
H	0.52507	-0.6473	0.92758
H	0.40542	0.30309	0.93632
H	0.59526	0.21173	0.62215
H	-0.08388	-0.29507	0.82666
N	0	0	0.44289

Table 6. Atomistic coordinates for the AB-stacking mode of TFPA-TAPB-COF optimized by using DFTB+ method. Space group: *P3; a* = 23.394 Å, *b* = 23.394 Å, and *c* = 7.179 Å.

Atom	*x/a*	*y/b*	*z/c*
C	0.54067	0.16046	0.10875
C	0.57483	0.22862	0.10776
C	0.63133	0.26324	0.21893
C	0.65238	0.22814	0.33119
C	0.61823	0.15995	0.33095
C	0.56218	0.12498	0.21769
N	0.53272	0.47695	0.21129
C	0.08174	0.52269	0.17064
C	0.14933	0.54936	0.16493
C	0.19162	0.61112	0.24511
C	0.16355	0.64519	0.33034
C	0.09587	0.61869	0.33495
C	0.05374	0.55684	0.25582
C	0.26462	0.63977	0.2398
C	0.29197	0.59866	0.23897
C	0.54629	0.0181	0.2615
H	0.497	0.13347	0.02078
H	0.55793	0.25551	0.02015
H	0.69561	0.25483	0.42099
H	0.63477	0.13398	0.42365
H	0.04941	0.4745	0.10711
H	0.16944	0.52185	0.09382
H	0.19482	0.6929	0.39734
H	0.07528	0.64622	0.40361
H	0.25943	0.5451	0.23901
H	0.59838	0.03717	0.3088
C	0.19913	0.49214	0.66251
C	0.23412	0.56022	0.65325
C	0.29725	0.59637	0.73307
C	0.32389	0.561	0.81895
C	0.28878	0.49293	0.83004
C	0.22506	0.45725	0.75464
N	0.201	0.81323	0.75503
C	0.75193	0.85768	0.74858
C	0.82009	0.8887	0.74823
C	0.85707	0.93482	0.88613
C	0.82385	0.94868	1.02511

C	0.75558	0.91679	1.02731
C	0.71843	0.87095	0.88869
C	0.93098	0.96856	0.88545
C	0.96263	0.93136	0.88543
C	0.19147	0.35402	0.89129
H	0.15003	0.46517	0.59978
H	0.21185	0.58528	0.58076
H	0.37299	0.58701	0.88114
H	0.31211	0.46776	0.89695
H	0.72353	0.82204	0.63924
H	0.84526	0.87754	0.63765
H	0.85185	0.98425	1.13494
H	0.73051	0.92783	1.13864
H	0.93325	0.87739	0.88555
H	0.22375	0.37739	1.01594
N	0.66667	0.33333	0.2194
N	0.33333	0.66667	0.72637

Table 7. Atomistic coordinates for the AA-stacking mode of TFPA-TAPA-COF optimized by using DFTB+ method. Space group: *P*3*; a* = 20.8677 Å, *b* = 20.8677 Å, and *c* = 4.1175 Å.

Atom	***x/a***	***y/b***	***z/c***
C	-0.04977	1.14634	0.29258
C	-0.01204	1.10778	0.27472
C	-0.03955	1.0392	0.43122
C	-0.10701	1.01025	0.59848
C	-0.14504	1.04857	0.61396
C	-0.11634	1.11823	0.46594
N	0.31234	1.1499	0.46794
C	-0.26369	0.53303	0.49259
C	-0.30847	0.45708	0.48958
C	-0.28721	0.41168	0.65389
C	-0.21956	0.44534	0.82123
C	-0.17534	0.52143	0.82573
C	-0.19628	0.56684	0.66105
C	-0.20338	1.14907	0.66684
H	-0.02763	1.19966	0.16914
H	0.03936	1.1312	0.13557
H	-0.1301	0.95696	0.72237
H	-0.19731	1.02359	0.74764
H	-0.2807	0.56749	0.35972
H	0.63949	0.43264	0.35498
H	-0.20155	0.41176	0.95348
H	-0.12341	0.54625	0.96267
H	-0.2262	1.10306	0.84866
N	0	1	0.42
N	-0.33333	0.33333	0.65134

Table 8. Atomistic coordinates for the refined unit cell parameters for TFPA-TAPA-COF via Pawley refinement. Space group: *P3; a* = 20.0691 Å, *b* = 20.0691 Å, and *c* = 4.1936Å.

Atom	***x/a***	***y/b***	***z/c***
C	-0.04977	1.14634	0.29258
C	-0.01204	1.10778	0.27472
C	-0.03955	1.0392	0.43122
C	-0.10701	1.01025	0.59848
C	-0.14504	1.04857	0.61396
C	-0.11634	1.11823	0.46594
N	0.31234	1.1499	0.46794
C	-0.26369	0.53303	0.49259
C	-0.30847	0.45708	0.48958
C	-0.28721	0.41168	0.65389
C	-0.21956	0.44534	0.82123
C	-0.17534	0.52143	0.82573
C	-0.19628	0.56684	0.66105
C	-0.20338	1.14907	0.66684
H	-0.02763	1.19966	0.16914
H	0.03936	1.1312	0.13557
H	-0.1301	0.95696	0.72237
H	-0.19731	1.02359	0.74764
H	-0.2807	0.56749	0.35972
H	0.63949	0.43264	0.35498
H	-0.20155	0.41176	0.95348
H	-0.12341	0.54625	0.96267
H	-0.2262	1.10306	0.84866
N	0	1	0.42
N	-0.33333	0.33333	0.65134

Table 9. Atomistic coordinates for the AB-stacking mode of TFPA-TAPA-COF optimized by using DFTB+ method. Space group: *P3; a* = 20.8778 Å, *b* = 20.8778 Å, and *c* = 7.7734 Å.

Atom	*x/a*	*y/b*	*z/c*
C	0.28632	0.81315	0.10156
C	0.32206	0.7726	0.09417
C	0.29656	0.70843	0.19413
C	0.23491	0.68617	0.30129
C	0.19915	0.72675	0.30769
C	0.22382	0.79054	0.20617
N	0.64421	0.80766	0.20705
C	0.06927	0.19989	0.18339
C	0.02397	0.12403	0.18154
C	0.04628	0.07815	0.26255
C	0.11559	0.11113	0.34381
C	0.16134	0.18693	0.34145
C	0.13909	0.23286	0.2619
C	0.12508	0.81191	0.25967
H	0.30591	0.86286	0.02263
H	0.37028	0.79061	0.01074
H	0.2155	0.637	0.38213
H	0.15255	0.70907	0.39616
H	0.05116	0.23479	0.11929
H	0.97101	0.10026	0.11429
H	0.13403	0.07729	0.41101
H	0.21508	0.21103	0.40599
H	0.08778	0.75361	0.30352
C	0.95794	0.15206	0.69045
C	0.99387	0.11167	0.68189
C	0.96317	0.04183	0.76054
C	0.89466	0.01377	0.84379
C	0.85829	0.05372	0.85013
C	0.88999	0.12442	0.77603
N	0.31218	0.14336	0.7733
C	0.73367	0.53147	0.77199
C	0.69095	0.45529	0.76737
C	0.71057	0.41179	0.86761
C	0.77374	0.44636	0.97216
C	0.81563	0.52265	0.97701
C	0.79664	0.56661	0.87705
C	0.80562	0.15813	0.88361

H	0.98285	0.20646	0.6293
H	0.04611	0.13469	0.61173
H	0.86913	0.95971	0.90629
H	0.8045	0.0287	0.91425
H	0.71842	0.56511	0.6927
H	0.64198	0.42889	0.68484
H	0.78949	0.41318	1.05151
H	0.86439	0.54889	1.0605
H	0.78637	0.11535	0.98778
N	0.33333	0.66667	0.18782
N	0	0	0.26174
N	0	0	0.75461
N	0.66667	0.33333	0.86317

Table 10. Atomistic coordinates for the AA-stacking mode of BTMA-TAPA-COF optimized by using DFTB+ method. Space group: *P*3*;a* = 20.7444 Å, *b* = 20.7444 Å, and *c* = 4.1175 Å.

Atom	*x/a*	*y/b*	*z/c*
C	-0.04977	1.14634	0.29258
C	-0.01204	1.10778	0.27472
C	-0.03955	1.0392	0.43122
C	-0.10701	1.01025	0.59848
C	-0.14504	1.04857	0.61396
C	-0.11634	1.11823	0.46594
N	0.31234	1.1499	0.46794
C	-0.26369	0.53303	0.49259
C	-0.30847	0.45708	0.48958
C	-0.28721	0.41168	0.65389
C	-0.21956	0.44534	0.82123
C	-0.17534	0.52143	0.82573
C	-0.19628	0.56684	0.66105
C	-0.20338	1.14907	0.66684
H	-0.02692	1.20204	0.16513
H	-0.13127	0.95424	0.7244
H	-0.20019	1.02369	0.74767
H	-0.22402	1.10087	0.84458
C	0.45874	0.36486	0.85463
H	0.41573	0.35006	1.05431
H	0.43522	0.37078	0.61385
H	0.51058	0.41936	0.91712
C	0.58699	0.41828	0.88764
H	0.60984	0.45057	0.65224
H	0.63341	0.43756	1.07403
H	0.54165	0.42828	0.98581
C	0.40712	0.12309	0.41526
H	0.42505	0.08341	0.51369
H	0.39929	0.11586	0.14105
H	0.35272	0.11064	0.53379
C	0.53494	0.18172	0.76823
H	0.56011	0.14655	0.69146
H	0.47383	0.14416	0.82695
H	0.56498	0.21541	0.99255
H	0.0419	1.13159	0.13207
N	0	1	0.42
B	-0.33333	0.33333	0.65134

Table 11. Atomistic coordinates for the refined unit cell parameters for BTMA-TAPA-COF via Pawley refinement. Space group: *P*3*;* a = 20.7444 Å, b = 20.7444 Å, and c = 4.1175 Å.

Atom	*x/a*	*y/b*	*z/c*
C	-0.04977	1.14634	0.29258
C	-0.01204	1.10778	0.27472
C	-0.03955	1.0392	0.43122
C	-0.10701	1.01025	0.59848
C	-0.14504	1.04857	0.61396
C	-0.11634	1.11823	0.46594
N	0.31234	1.1499	0.46794
C	-0.26369	0.53303	0.49259
C	-0.30847	0.45708	0.48958
C	-0.28721	0.41168	0.65389
C	-0.21956	0.44534	0.82123
C	-0.17534	0.52143	0.82573
C	-0.19628	0.56684	0.66105
C	-0.20338	1.14907	0.66684
H	-0.02692	1.20204	0.16513
H	-0.13127	0.95424	0.7244
H	-0.20019	1.02369	0.74767
H	-0.22402	1.10087	0.84458
C	0.45874	0.36486	0.85463
H	0.41573	0.35006	1.05431
H	0.43522	0.37078	0.61385
H	0.51058	0.41936	0.91712
C	0.58699	0.41828	0.88764
H	0.60984	0.45057	0.65224
H	0.63341	0.43756	1.07403
H	0.54165	0.42828	0.98581
C	0.40712	0.12309	0.41526
H	0.42505	0.08341	0.51369
H	0.39929	0.11586	0.14105
H	0.35272	0.11064	0.53379
C	0.53494	0.18172	0.76823
H	0.56011	0.14655	0.69146
H	0.47383	0.14416	0.82695
H	0.56498	0.21541	0.99255
H	0.0419	1.13159	0.13207
N	0	1	0.42
B	-0.33333	0.33333	0.65134

Table 12. Atomistic coordinates for the AB-stacking mode of BTMA-TAPA-COF optimized by using DFTB+ method. Space group: *P3; a* = 20.878 Å, *b* = 20.8778 Å, and *c* = 7.7734 Å.

Atom	*x/a*	*y/b*	*z/c*
C	0.28632	0.81315	0.10156
C	0.32206	0.7726	0.09417
C	0.29656	0.70843	0.19413
C	0.23491	0.68617	0.30129
C	0.19915	0.72675	0.30769
C	0.22382	0.79054	0.20617
C	0.64421	0.80766	0.20705
C	0.06927	0.19989	0.18339
C	0.02397	0.12403	0.18154
C	0.04628	0.07815	0.26255
C	0.11559	0.11113	0.34381
C	0.16134	0.18693	0.34145
C	0.13909	0.23286	0.2619
N	0.12508	0.81191	0.25967
C	0.30591	0.86286	0.02263
C	0.37028	0.79061	0.01074
C	0.2155	0.637	0.38213
C	0.15255	0.70907	0.39616
H	0.05012	0.23677	0.12047
H	0.96805	0.09818	0.11402
H	0.13454	0.07526	0.41256
H	0.21814	0.21301	0.40482
C	0.95794	0.15206	0.69045
C	0.99387	0.11167	0.68189
C	0.96317	0.04183	0.76054
C	0.89466	0.01377	0.84379
C	0.85829	0.05372	0.85013
C	0.88999	0.12442	0.77603
N	0.31218	0.14336	0.7733
C	0.73367	0.53147	0.77199
C	0.69095	0.45529	0.76737
C	0.71057	0.41179	0.86761
C	0.77374	0.44636	0.97216
C	0.81563	0.52265	0.97701
C	0.79664	0.56661	0.87705
C	0.80562	0.15813	0.88361
H	0.98347	0.20887	0.62733

H	0.04878	0.13495	0.61069
H	0.86807	0.95706	0.90773
H	0.8021	0.02933	0.91589
C	0.71842	0.56511	0.6927
C	0.64198	0.42889	0.68484
C	0.78949	0.41318	1.05151
C	0.86439	0.54889	1.0605
H	0.78833	0.11344	0.98617
H	0.67018	0.77392	0.16111
H	0.28056	0.84669	-0.11132
H	0.36875	0.89218	0.01221
H	0.28883	0.90152	0.08474
H	0.35652	0.80155	-0.12414
H	0.38588	0.74555	0.00492
H	0.41869	0.84351	0.06451
H	0.26461	0.63089	0.42305
H	0.17469	0.58598	0.3064
H	0.18697	0.64289	0.50117
H	0.13545	0.65158	0.44762
H	0.104	0.70747	0.32516
H	0.16964	0.74973	0.50791
H	0.6557	0.53931	0.69201
H	0.73891	0.56763	0.55557
H	0.74477	0.62343	0.74794
H	0.6216	0.36714	0.67551
H	0.65676	0.45453	0.55097
H	0.59655	0.43749	0.74205
H	0.82186	0.39363	0.97008
H	0.7376	0.36318	1.10412
H	0.82542	0.44814	1.16304
H	0.91342	0.59309	0.98494
H	0.87791	0.50538	1.10838
H	0.85259	0.57551	1.17507
B	0.33333	0.66667	0.18782
N	0	0	0.26174
N	0	0	0.75461
B	0.66667	0.33333	0.86317

2.5 References

(1) Aresta. M, Dibenedetto. A, Angelini. A. Catalysis for the Valorization of Exhaust Carbon: from CO_2 to Chemicals, Materials, and Fuels. Technological Use of CO_2. *Chem. Rev.,* 2014, **114**, 1709-1742.

(2) Olah. G. A, Prakash. G. K, Goeppert. A. Anthropogenic Chemical Carbon Cycle for a Sustainable Future. *J. Am. Chem. Soc.,* 2011, **133**, 12881-12898.

(3) Sanz-Pérez, E. S, Murdock. C. R, Didas. S. A, Jones. C. W. Direct Capture of CO_2 from Ambient Air. *Chem. Rev.,* 2016, **116**, 11840-11876.

(4) Feng. X, Ding. X. S, Jiang. D. Covalent organic frameworks. *Chem. Soc. Rev.,* 2012, **41**, 6010-6022.

(5) Yaghi. O. M. Reticular Chemistry-Construction, Properties, and Precision Reactions of Frameworks. *J. Am. Chem. Soc.,* 2016, **138**, 15507–15509.

(6) Xu. H, Gao. J, Jiang. D. Stable, crystalline, porous, covalent organic frameworks as a platform or chiral organocatalysts. *Nat. Chem.,* 2015, **7**, 905-912.

(7) Fang. Q. R, Zhuang. Z. B, Gu. S, Kaspar. R. B, Zheng. J, Wang. J. H, Qiu. S. L, Yan. Y. S. Designed synthesis of large-pore crystalline polyimide covalent organic frameworks. *Nat. Commun*., 2014, **5**, 4503. Doi: 10.1038/ncomms5503.

(8) Colson. J. W, Dichtel. W. R. Rationally synthesized two-dimensional polymers. *Nat. Chem*., 2013, **5**, 453-465.

(9) Ascherl. L, Sick. T, Margraf. J. T, Lapidus. S. H, Calik. M, Hettstedt. C, Karaghiosoff. K, Döblinger. M, Clark. T, Chapman. K. W, Auras. F, Bein. T. Molecular docking sites designed for the generation of highly crystalline covalent organic frameworks. *Nat. Chem*., 2016, **8**, 310-316.

(10) Zeng. Y. F, Zou. R. Y, Luo. Z, Zhang. H. C, Yao. X, Ma. X, Zou. R. Q, Zhao. Y. Covalent organic Frameworks Formed with Two Types of Covalent Bonds Based on Orthogonal Reactions. *J. Am. Chem. Soc*., 2015, **137**, 1020-1023.

(11) Dalapati. S, Addicoat. M, Jin. S, Sakurai. T, Gao. J, Xu. H, Irle. S, Seki. S, Jiang. D. Rational design of crystalline supermicroporous covalent organic frameworks with triangular topologies. *Nat. Commun*., 2015, **6**, 7786. Doi: 10.1038/ncomms8786.

(12) Huang. N, Zhai. L. P, Coupry. D. E, Addicoat. M. A, Okushita. K, Nishimura. K, Heine. T, Jiang. D. Multiple-component covalent organic frameworks. *Nat. Commun*., 2016, **7**, 12325. Doi: 10.1038/ncomms12325.

(13) Zhu. Y, Wan. S, Jin. Y, Zhang. W. Desymmetrized Vertex Design for the Synthesis of Covalent Organic Frameworks with Periodically Heterogeneous Pore Structures. *J. Am. Chem. Soc*., 2015, **137**, 13772-13775.

(14) Huang. N, Wang. P. Jiang. D. Covalent organic frameworks: a materials platform for structural and functional designs. *Nat. Rev. Mat.*, 2016, **1**, 16068. Doi: 10.1038/natrevmats2016.68.

(15) Pang. Z. F, Xu. S. Q, Zhou. T. Y, Liang. R. R, Zhan. T. G, Zhao. X. Construction of Covalent Organic Frameworks Bearing Three Different Kinds of Pores through the Heterostructural Mixed Linker Strategy. *J. Am. Chem. Soc*., 2016, **138**, 4710-4713.

(16) Kandambeth. S, Venkatesh. V, Shinde. D. B, Kumari. S, Halder. A, Verma. S, Banerjee. R. Self-templated chemically stable hollow spherical covalent organic frameworks. *Nat. Commun.,* 2015, **6**, 6786. Doi: 10.1038/ncomms7786.

(17) Xu. F, Xu. H, Chen. X, Wu. D, Wu. Y, Liu. H, Gu. C, Fu. R, Jiang. D. Radical Covalent Organic Frameworks: A General Strategy to immobilize Open-Accessible Polyradicals for High-Performance Capacitive Energy Storage. *Angew. Chem. Int. Ed.,* 2015, **54**, 6814-6818.

(18) Bertrand. G. H. V, Michaelis. V. K, Ong. T. -C, Griffin. R. G, Dincă. M. Thiophene-based covalent organic frameworks. *Proc. Nat. Acad. Sci. USA.,* 2013, **110**, 4923-4928.

(19) Vyas. V. S, Haase. F, Stegbauer. L, Savasci. G, Podjaski. F, Ochsenfeld. C. Lotsch. B. V. A tunable azine covalent organic framework platform for visible light-induced hydrogen generation. *Nat. Commun.,* 2015, **6**, 8508. Doi: 10.1038/ncomms9508.

(20) Tan. J, Namuangruk. S, Kong. W, Kungwan. N, Guo. J, Wang. C. C. Manipulation of Amorphous-to-Crystalline Transformation: Towards the Construction of Covalent Organic Framework Hybrid Microspheres with NIR Photothermal Conversion Ability. *Angew. Chem. Int. End.*, 2016, **55**, 13979-13984.

(21) Xu. H, Chen. X, Gao. J, Lin. J, Addicoat. M, Irle. S, Jiang. D. Catalytic covalent organic frameworks via pore surface engineering. *Chem. Commun.,* 2014, **50**, 1292-1294.

(22) Sun. Q, Aguila. B, Perman. J. A, Nguyen. N. T.-K. Ma. S. Flexibility Matters: Cooperative Active Sites in Covalent Frameworks and Threaded Ionic Polymer. *J. Am. Chem. Soc.,* 2016, **138**, 15790-15796.

(23) Ding. S. Y, Gao. J, Wang. Q, Zhang. Y, Song. W. G, Su. C. Y. Wang. W. Construction of Covalent organic Framework for Catalysis: Pd/COF-LZU1 in Suzuki-Miyaura Coupling Reaction. *J. Am. Chem. Soc.,* 2011, **133**, 19816-19822.

(24) Ma. H. P, Liu. B. L, Li. B, Zhang. L. M, Li. Y. G, Tan. H. Q, Zang. H. Y, Zhu. G. S. Cationic Covalent Organic Frameworks: A Simple Platform of Anionic Exchange for Porosity Tuning and Proton Conduction. *J. Am. Chem. Soc.,* 2016, **138**, 5897-5903.

(25) Huang. N, Chen. X, Krishna. R, Jiang. D. Two-Dimensional Covalent Organic Frameworks for Carbon Dioxide Capture through Channel-wall Functionalization. *Angew. Chem. Int. End.*, 2015, **54**, 2986-2990.

(26) Rabbani. M. G, Sekizkardes. A. K, Kahveci. Z, Reich. T. E, Ding. R. S, EI-Kaderi. H. M. A 2D Mesoporous Imine-Linked Covalent Organic Framework for High Pressure Gas Storage Applications. *Chem. Eur. J.,* 2013, **19**, 3324-3328.

(27) Huang. N, Krishna. R, Jiang. D. Tailor-Made Pore Surface Engineering in Covalent Organic Frameworks: Systematic Functionalization for Performance Screening. *J. Am. Chem. Soc.,* 2015, **137**,7079-7082.

(28) Dlapati. S, Jin. S, Guo. J, Xu. Y, Nagai. A, Jiang. D. An Azine-Linked Covalent Organic Framework. *J. Am. Chem. Soc.,* 2013, **135**,17310-17313.

(29) Alahakoon. S. B, Thompson. C. M, Nguyen. A. X, Occhialini. G, McCandless. G. T, Smaldone. R. A. An azine-linked hexaphenylbenzene based covalent organic framework. *Chem. Commun.,* 2016, **5**2, 2843-2845.

(30) Li. Z. P, Feng. X, Zou. Y. C, Zhang. Y. W, Xia. H, Liu. X. M, Mu. Y. A 2D azine-linked covalent organic framework for gas storage applications. *Chem. Commun.,* 2014, **50**, 13825-13828.

(31) Li. Z. P, Zhi. Y. F, Feng. X, Ding. X. S, Zou. Y. C, Liu. X. M, Mu. Y. An Azine-Linked Covalent organic Framework: Synthesis, Characterization and Efficient Gas Storage. *Chem. Eur. J.,* 2015, **21**, 12079-12084.

(32) Kang. Z. X, Peng. Y. W, Qian. Y. H, Yuan. D. Q, Addicoat. M. A, Heine. T, Hu. Z. G, Tee. L, Guo. Z. G, Zhao. D. Mixed Matrix Membranes (MMMs) Comprising Exfoliated 2D Covalent Organic Frameworks (COFs) for Efficient CO_2 Separation. *Chem. Mater.,* 2016, **28**, 1277-1285.

(33) Aradi. B, Hourahine. B, Frauenheim T. DFTB+, a Sparse Matrix-Based Implementation of the DFTB Method. J. Phys. Chem. A., 2007, **111**, 5678.

(34) http://www.dftb.org.

(35) Accelrys, Material Studio Release Notes, Release 4.4, Accelrys Software, San Diego 2008.

(36) Gong. Z. M, Yang. B, Lin. H. P, Tang. Y. Y, Tang. Z. Y, Zhang. J. J, Zhang. H. M, Li. Y. Y, Xie. Y. S, Li. Q, Chi. L. F. Structural Variation in Surface-Supported Synthesis by Adjusting the Stoichiometric Ratio of the Reactants. *ACS Nano*, 2016, **10**, 4228.

(37) Liu. Y, Xu. X, Zheng. F. K, Cui. Y. Chiral Octupolar Metal-Organoboron NLO Frameworks with (14,3) Topology. *Angew. Chem. Int. End.,* 2008, **47**, 4538-4541.

Chapter 3

Design and Synthesis of Three-Dimensional Covalent Organic Frameworks for Carbon Dioxide Capture

Abstract: Covalent organic frameworks (COFs) represent a new porous crystalline polymer with tunable and predesignable structures. Here, two new COFs were constructed using highly flexible tetrahedral sp^3 nitrogen building blocks. These building blocks' flexibility produces structural changes, which produce the possibility for constructing COFs materials with mciropores and high BET surface area. The tetrahedral sp^3 nitrogen building blocks would break the planarity of the COFs' framework and form conventional 3D stacking structures. The results demonstrated that the micropore and porosity dominate the CO_2 adsorption process.

Keywords: Carbon Dioxide, 3D COFs, and Recycle

3.1 Introduction

CO_2 is the main component of greenhouse gas and its concentration in atmosphere are rapidly increasing since industrial revolution owing to the increasing population and industrial development.[1-3] Increasing concentration of CO_2 in the atmosphere leading to a series of detrimental effects such as global climate warming, rising sea level and anthropogenic climate change. Therefore, developing effective technologies and novel materials for CO_2 adsorption and sequestration is an urgent and essential task.

Covalent organic frameworks (COFs) are a new class of crystalline porous materials that allows precisely introduction of organic building blocks into extended two-dimensional (2D) or three-dimensional (3D) order structures.[4-9] these unique features enable COFs total design and control of structures including skeleton, pore size and shape.[10-15] Owing to the diversity of topologies and linkages and available building blocks, COFs have developed as a promising platform for constructing multi-functional materials with widely potential applications such as gas storage and separation, catalysis, energy storage and conversion, semiconductors and optoelectronics.[16-24]

Because of high porosity and controlabe and predesignable structures, COFs materials are promising candidates for CO_2 capture and separation.[4,14] To date, lots of 2D COFs have been developed for CO_2 uptake materials and these reported COFs exhibited outstanding CO_2 capture properties. In contrast, 3D COFs have been seldom reported in the filed of CO_2 adsorption and separation, even 3D COFs always have samll pore size and high BET surface area. Using 3D COFs for removing CO_2 from atmosphere and further understanding the principle is remaining explored. In this research work, I succeeded in syntheising two new 3D COFs with T_d-symmetric buidling blocks triarylamine.

3.2 Results and Discussions

3.2.1 Synthesis and Structural Characterizations

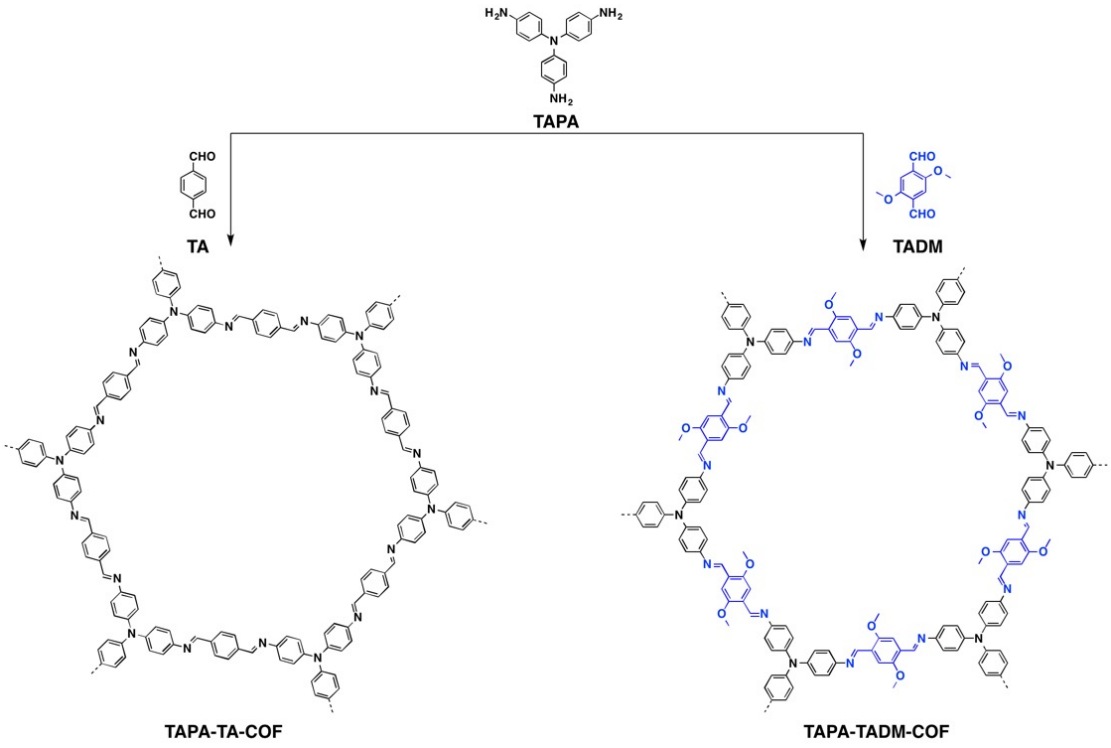

Figure 1. Schematic of synthesis and structures of 3D COFs： TAPA-TA-COF and TAPA-TADM-COF

I developed two novel 3D COFs structures with the same topology and similar micropore size by using T_d-symmetric buidling block tris(4-aminophenyl)amine (TAPA) as C_3 vertices and terephthaldehyde (TA) or dimethoxyterephthaldehyde (TADM) as C_2-phenyl edges. Polycondensation of TAPA and TA yield TAPA-TA-COF, whereas TAPA-TADM-COF was synthesized by condensation of TAPA and TADM (Figure 1). The polycondensation reactions were carried out under solvothermal conditions in a mixture of mesitylene and 1,4-dioxane for TAPA-TA-COF or *o*-dichlorobenzene and butanol for TAPA-TADM-COF with acetic acid catalyst at 120 °C for 3 days. TAPA-TA-COF and TAPA-TADM-COF were obtained in 78% and 84% yields, respectively. Infrared spectroscopy exhibited stretching vibration bands between 1622 and 1626 cm^{-1} that were assigned to the C=N bond (Figure 2). Experimental element analysis results are similar with the theoretical values for TAPA-TA-COF and TAPA-TADM-COF, respectively. Thermal gravimetric analysis revealed that these COFs are stable up to 400 °C under N_2 (Figure 3).

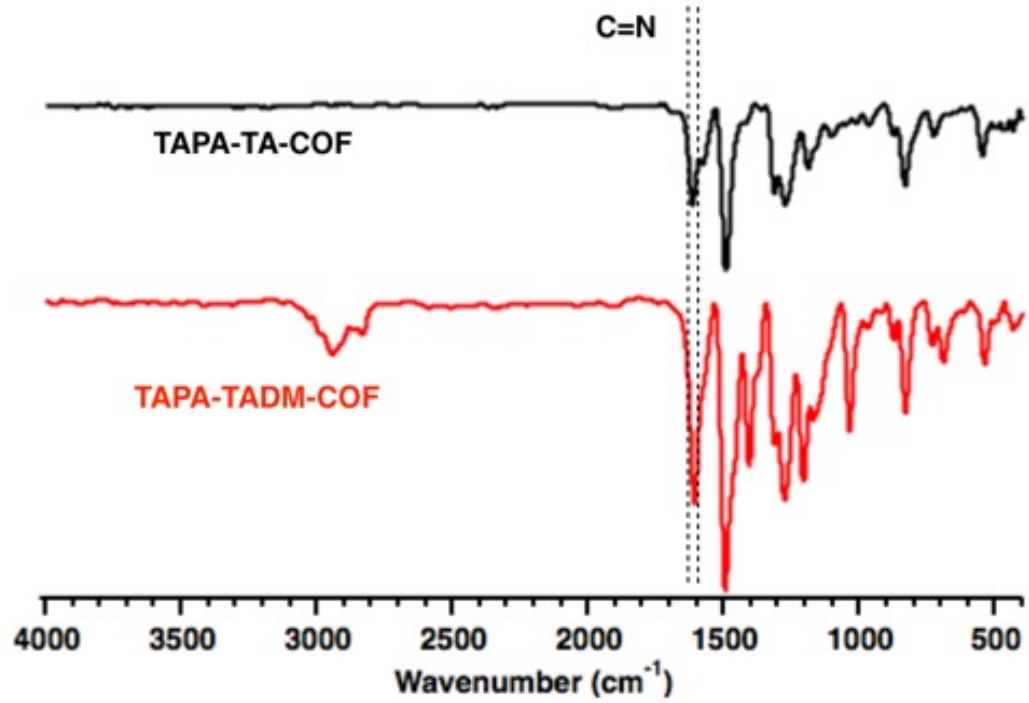

Figure 2. FT-IR spectra of TAPA-TA-COF (black) and TAPA-TADM-COF (red).

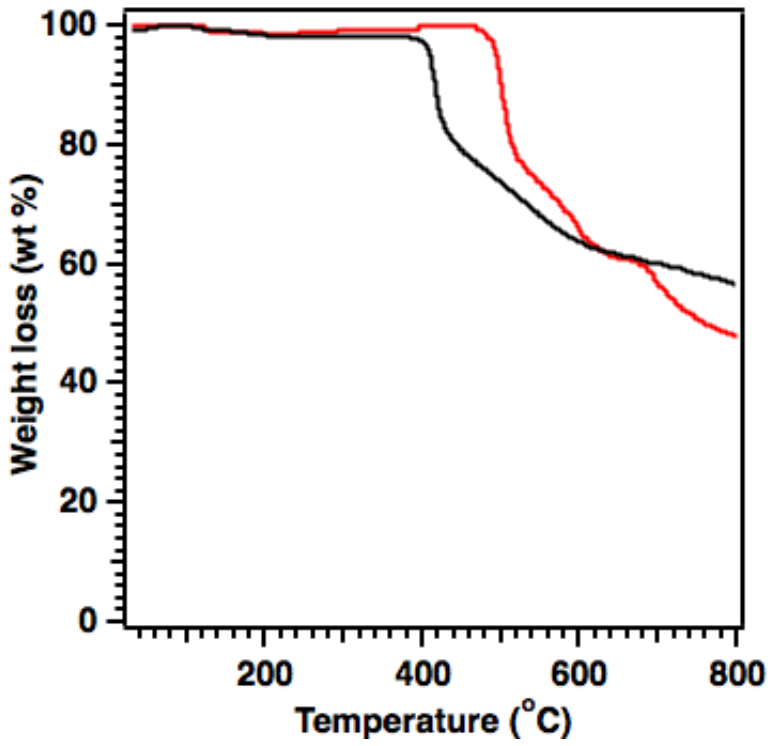

Figure 3. TGA curve of TAPA-TA-COF (black) and TAPA-TADM-COF (red)

TAPA-TA-COF has micrometre-scale shape morphology, as determined by field emission scanning electron microscopy (FE-SEM), whereas TAPA-TADM-COF adopted a micro-particle morphology (Figure 4).

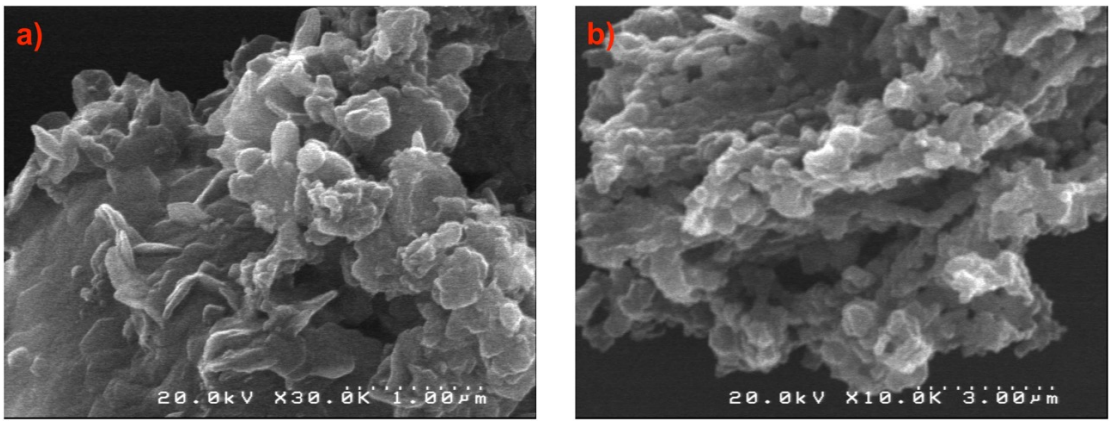

Figure 4. SEM images of TAPA-TA-COF **(a)** and TAPA-TADM-COF **(b)**

3.2.2 PXRD Pattern

The crystal structures of TAPA-TA-COF and TAPA-TADM-COF were resolved by using powder X-ray diffraction (PXRD) measurements. TAPA-TA-COF exhibited five prominent diffraction peaks at 5.5°, 8.56°, 11.04°, 19.06°, 20.76° and 22.68° (Figure 5). TAPA-TADM-COF exhibited similar PXRD peaks at 6.8°, 11.08°, 17.96° and 26.86° (Figure 5). The first diffraction peak appeared after 5°, which indicates that these two 3D COFs are microporous materials. Moreover, the weak peak intensity around 25° demonstrated that T_d-symmetric building block tris(4-aminophenyl)amine would destroy the planarity of the frameworks, which induces the 3D frameworks.

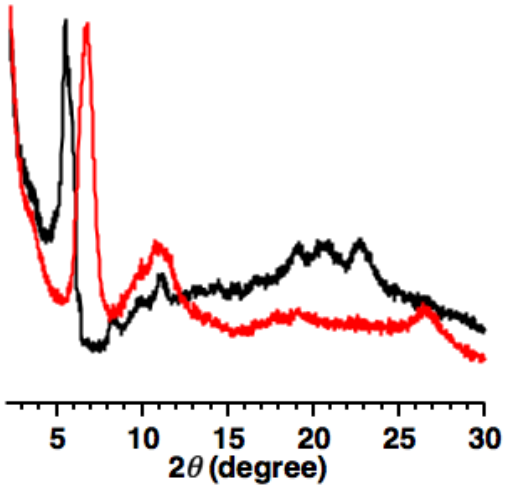

Figure 5. PXRD patterns of TAPA-TA-COF (black) and TAPA-TADM-COF (red)

3.2.3 Porosity Property

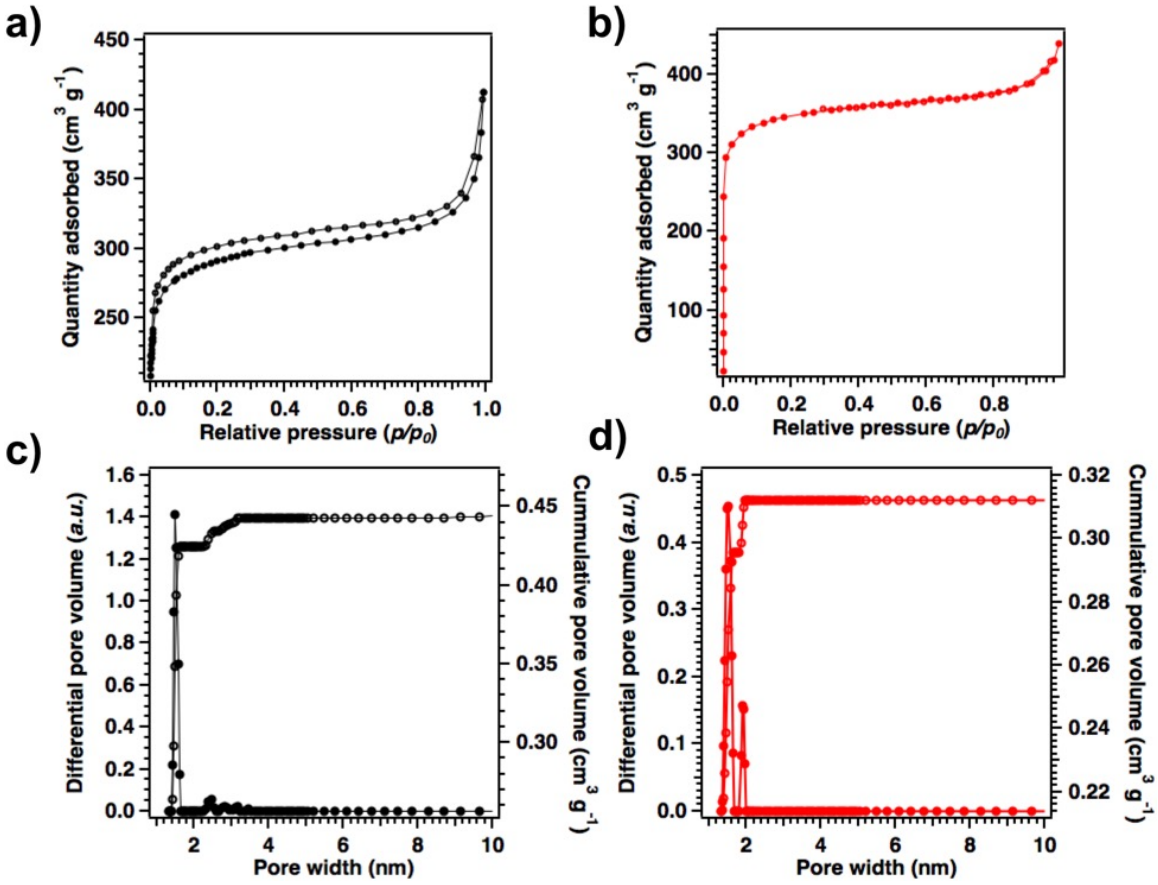

Figure 6. Nitrogen sorption isotherms measured at 77 K of **(a)** TAPA-TA-COF, **(b)** TAPA-TADM-COF; Pore size distribution and cumulative pore volume of **(c)** TAPA-TA-COF, **(d)** TAPA-TADM-COF.

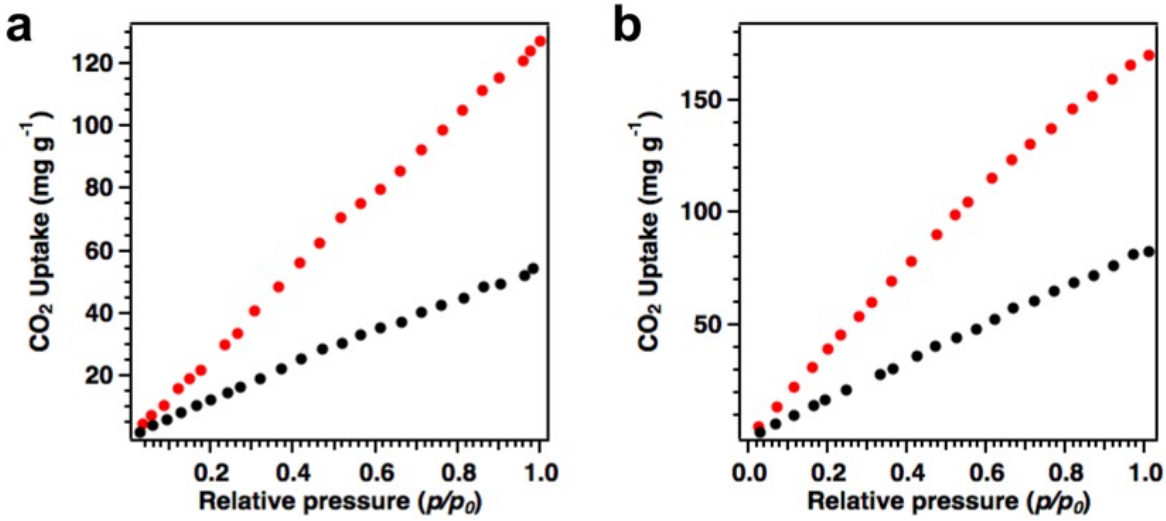

Figure 7. CO_2 uptake of **(a)** TAPA-TA-COF and **(b)** TAPA-TADM-COF at 273 K (red) and 298 K (black)

Porosity of TAPA-TA-COF and TAPA-TADM-COF was investigated by using nitrogen sorption measurements at 77 K. These COFs exhibited typical type I sorption curves (Figure 6), which indicates that these two 3D COFs are of micropore. TAPA-TA-COF and TAPA-TADM-COF exhibited Brunauer-Emmett-Teller (BET) surface area of 905 and 1150 $m^2 g^{-1}$ (Figure 6a and b). Their pore size distributions were calculated based on the N_2 sorption isotherms according to the nonlocal density functional theory method. Therefore, their pore sizes are 1.5 and 1.3 and 1.9 nm, respectively with pore volume of 0.44 and 0.31 $cm^3 g^{-1}$, respectively (Figure 6c and d). The pore size and high BET surface area prompted us to investigate the CO_2 uptake properties of these 3D COFs since the micropore has significant positive effect on the CO_2 adsorption properties.

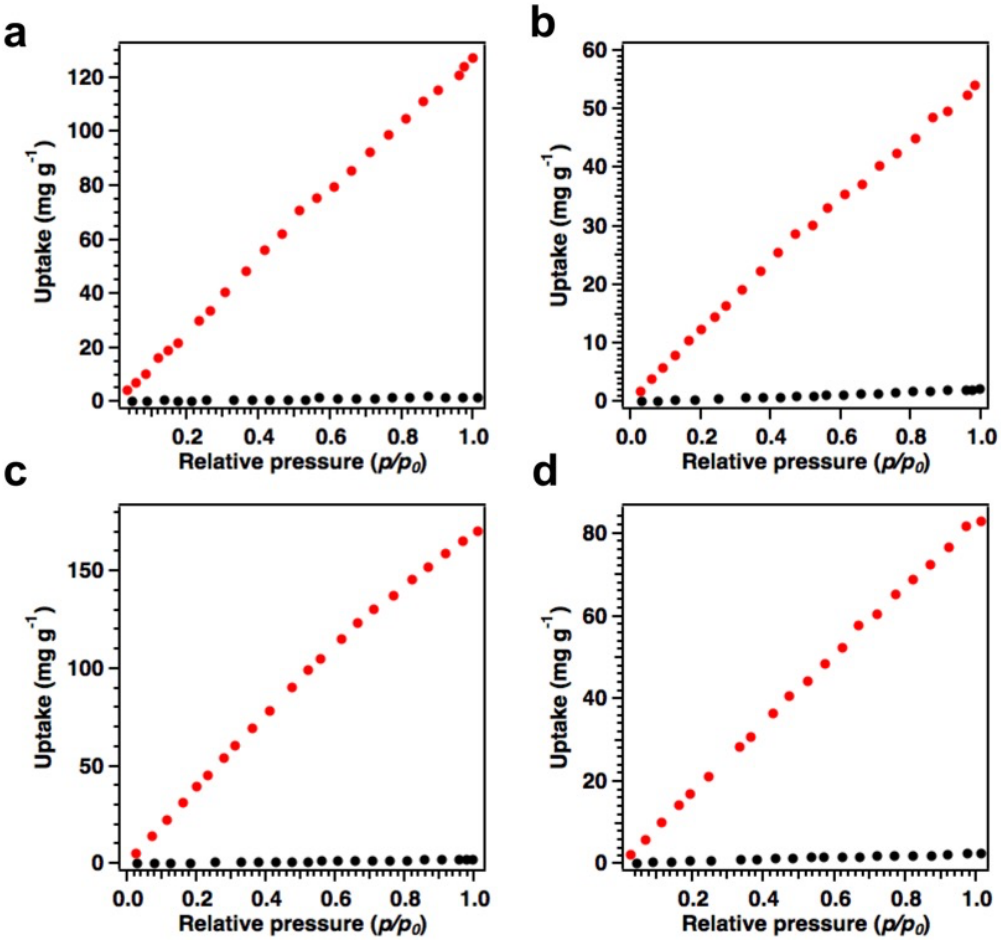

Figure 8. CO_2 (red) and N_2 (black) uptake of TAPA-TA-COF (**a, b**) and TAPA-TADM-COF (**c, d**), **a** and **c** at 273K, **b** and **d** at 298K

3.2.4 CO_2 Adsorption Property

CO_2 adsorption experiments were conducted at 273 K (Figure 7, red curve) and 298 K (Figure 7, black curve) up to 1 bar for these 3D COFs. TAPA-TA-COF exhibited CO_2 uptake capacity of 54 and 127 mg g^{-1} at 298 and 273 K, respectively (Figure 7a). By contrast, TAPA-TADM-COF showed slight enhanced CO_2 adsorption capacity of 82 and 170 mg g^{-1} at 298 and 273 K, respectively (Figure 7b). These capacities of TAPA-TADM-COF are 1.4

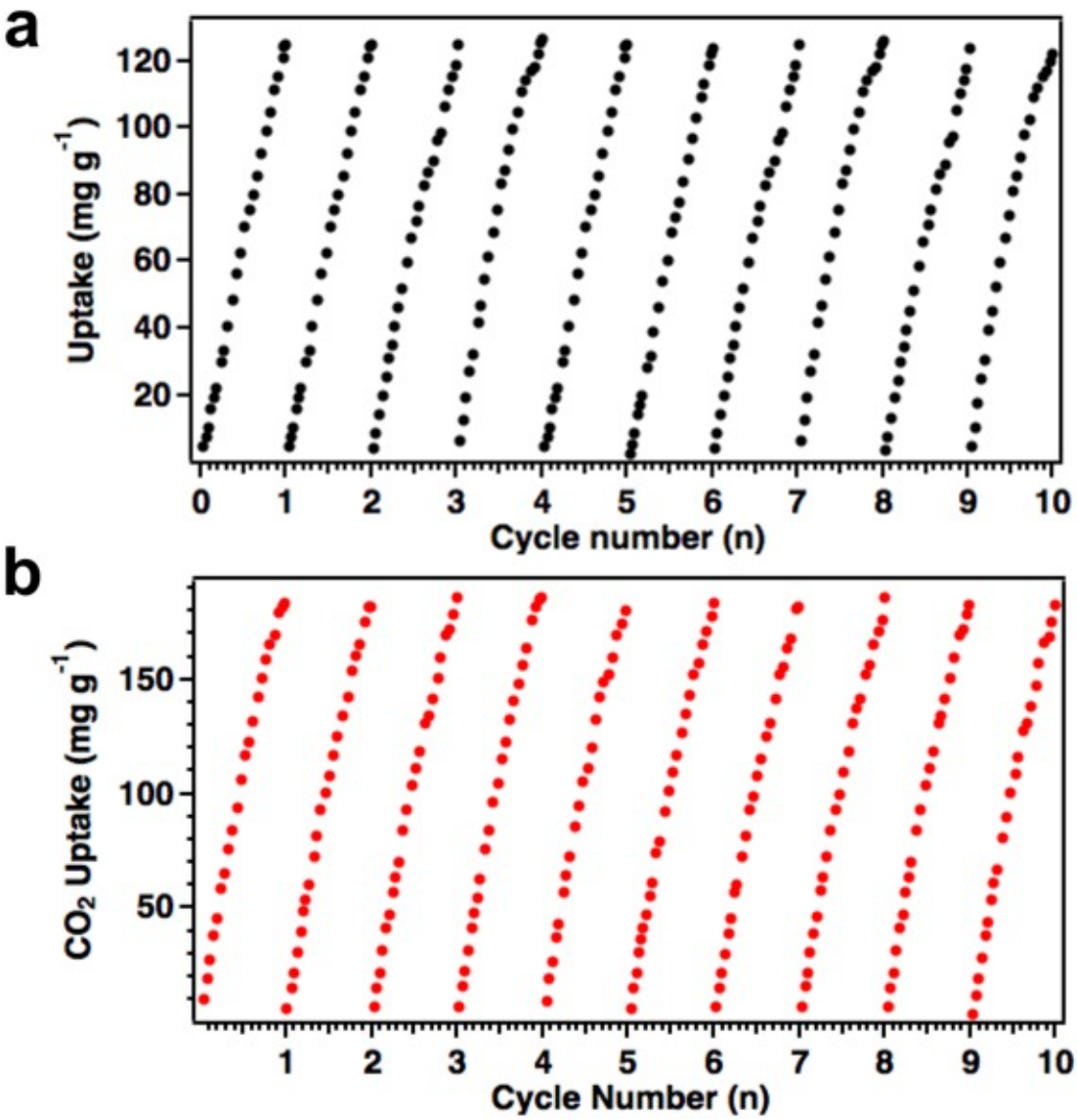

Figure 9. CO_2 uptake cycling performance: **a)** TAPA-TA-COF and **b)** TAPA-TADM at 273 K

fold those of TAPA-TA-COF and the enhanced CO_2 uptakes of TAPA-TADM-COF was attributed to the smaller pore size and the higher BET surface area of TAPA-TADM-COF.

By measuring the nitrogen sorption curves of TAPA-TA-COF and TAPA-TADM-COF at 273 and 298 K (Figure 8), the CO_2/N_2 selectivity at 273 K was evaluated to be 74 and 78 for TAPA-TA-COF and TAPA-TADM-COF, respectively. Similarly, the CO_2/N_2 selectivity 298 K was 69 and 73 for TAPA-TA-COF and TAPA-TADM-COF, respectively. The seletivites of these two 3D COFs are similar under 273 and 298k, which indicate that the seletiveits of these two COFs are irrespective of temperature. Moreover, both TAPA-TA-COF and TAPA-TADM-COF exhibited excellent cycle performance without deterioration in uptake capacity even after ten cycles, which revealed that these two 3D COFs are easyly capable of regenration for reuse (Figure 9).

Molecular design of COFs for CO_2 adsorption has been mainly focused on 2D COFs while using 3D COFs for CO_2 adsorption is still in the infant stage. Therefore, developing new 3D COFs system for CO_2 capture and separation is essential for this flied. Our results demonstrated that these two new constructed 3D COFs TAPA-TA-COF and TAPA-TADM-COF exhibited outstanding CO_2 capture capacity and selectivities. Moreover, our results demonstrated that using T_d-symmetric buidling blocks triarylamine is an effective way to form COFs with small pore size and high BET surface area, which provides an effective way to desgin COFs for CO_2 capture and separation.

3.3 Experimental Sections

3.3.1 Materials and Synthetic Procedures

Mesitylene, *o*-DCB, n-BuOH 1,4-dioxane and tetrahydrofuran (THF) were purchased from Wako chemicals. Tris(4-aminophenyl)amine(TAPA), terephthaldehyde (TA) and acetic acid were purchased from TCI. Dimethoxyterephthaldehyde (TADM) was synthesized according to a reported method.[25]

TAPA-TA-COF

A mixture of monomer TAPA (0.061 mmol, 17.7 mg) and TA (0.092 mmol, 12.3 mg) using AcOH (3 M, 0.1 mL) as catalyst and mesitylene/1,4-dioxane (0.9 mL/0.1 mL) as solvent in a 10ml-Pyrex tube. The reaction tube was degassed through three freeze-pump-thaw cycles. The reaction tube was sealed by flame gun. The tube was heated at 120 °C for 3 days. The COF solid was collected via centrifuge and the sample was washed with THF for 6 times (each time 3ml). The COF powder was dried at 120 °C under vacuum to obtain the TAPA-TA-COF solid in 78% yield. Elemental analysis calcd for TAPA-TA-COF: C, 80.41; H, 5.15; N, 12.37. Found: C, 77.27; H. 4.70; N, 11.52.

TAPA-TADM-COF

A mixture of monomer TAPA (0.052 mmol, 15.02 mg) and TAPB (0.078 mmol, 14.98 mg) using AcOH (6 M, 0.1 mL) as catalyst and *o*-DCB/BuOH (0.7 mL/0.3 mL) as reaction solvent in a 10ml-Pyrex tube. The reaction tube was degassed through three freeze-pump-thaw cycles. The reaction tube was sealed by flame gun. The reaction mixture was heated at 120 °C for 3 days. The COF solid was collected via centrifuge, washed with THF for 6 times (each time 3ml). The COF powder was dried at 120 °C under vacuum to give the TAPA-TADM-COF in 84% yield. Elemental analysis calcd for TFPB-TAPB-COF: C, 74.83; H, 5.34; N, 10.69. Found: C, 76.06; H. 4.79; N, 10.94.

3.4 Reference

(1) Aresta. M, Dibenedetto. A, Angelini. A. Catalysis for the Valorization of Exhaust Carbon: from CO_2 to Chemicals, Materials, and Fuels. Technological Use of CO_2. *Chem. Rev.,* 2014, **114**, 1709-1742.

(2) Olah. G. A, Prakash. G. K, Goeppert. A. Anthropogenic Chemical Carbon Cycle for a Sustainable Future. *J. Am. Chem. Soc.,* 2011, **133**, 12881-12898.

(3) Sanz-Pérez, E. S, Murdock. C. R, Didas. S. A, Jones. C. W. Direct Capture of CO_2 from Ambient Air. *Chem. Rev.,* 2016, **116**, 11840-11876.

(4) Feng. X, Ding. X. S, Jiang. D. Covalent organic frameworks. *Chem. Soc. Rev.,* 2012, **41**, 6010-6022.

(5) Yaghi. O. M. Reticular Chemistry-Construction, Properties, and Precision Reactions of Frameworks. *J. Am. Chem. Soc.,* 2016, **138**, 15507–15509.

(6) Xu. H, Gao. J, Jiang. D. Stable, crystalline, porous, covalent organic frameworks as a platform or chiral organocatalysts. *Nat. Chem.,* 2015, **7**, 905-912.

(7) Fang. Q. R, Zhuang. Z. B, Gu. S, Kaspar. R. B, Zheng. J, Wang. J. H, Qiu. S. L, Yan. Y. S. Designed synthesis of large-pore crystalline polyimide covalent organic frameworks. *Nat. Commun*., 2014, **5**, 4503. Doi: 10.1038/ncomms5503.

(8) Colson. J. W, Dichtel. W. R. Rationally synthesized two-dimensional polymers. *Nat. Chem*., 2013, **5**, 453-465.

(9) Ascherl. L, Sick. T, Margraf. J. T, Lapidus. S. H, Calik. M, Hettstedt. C, Karaghiosoff. K, Döblinger. M, Clark. T, Chapman. K. W, Auras. F, Bein. T. Molecular docking sites designed for the generation of highly crystalline covalent organic frameworks. *Nat. Chem*., 2016, **8**, 310-316.

(10) Zeng. Y. F, Zou. R. Y, Luo. Z, Zhang. H. C, Yao. X, Ma. X, Zou. R. Q, Zhao. Y. Covalent organic Frameworks Formed with Two Types of Covalent Bonds Based on Orthogonal Reactions. *J. Am. Chem. Soc*., 2015, **137**, 1020-1023.

(11) Dalapati. S, Addicoat. M, Jin. S, Sakurai. T, Gao. J, Xu. H, Irle. S, Seki. S, Jiang. D. Rational design of crystalline supermicroporous covalent organic frameworks with triangular topologies. *Nat. Commun*., 2015, **6**, 7786. Doi: 10.1038/ncomms8786.

(12) Huang. N, Zhai. L. P, Coupry. D. E, Addicoat. M. A, Okushita. K, Nishimura. K, Heine. T, Jiang. D. Multiple-component covalent organic frameworks. *Nat. Commun*., 2016, **7**, 12325. Doi: 10.1038/ncomms12325.

(13) Zhu. Y, Wan. S, Jin. Y, Zhang. W. Desymmetrized Vertex Design for the Synthesis of Covalent Organic Frameworks with Periodically Heterogeneous Pore Structures. *J. Am. Chem. Soc*., 2015, **137**, 13772-13775.

(14) Huang. N, Wang. P. Jiang. D. Covalent organic frameworks: a materials platform for structural and functional designs. *Nat. Rev. Mat.*, 2016, **1**, 16068. Doi: 10.1038/natrevmats2016.68.

(15) Pang. Z. F, Xu. S. Q, Zhou. T. Y, Liang. R. R, Zhan. T. G, Zhao. X. Construction of Covalent Organic Frameworks Bearing Three Different Kinds of Pores through the Heterostructural Mixed Linker Strategy. *J. Am. Chem. Soc*., 2016, **138**, 4710-4713.

(16) Kandambeth. S, Venkatesh. V, Shinde. D. B, Kumari. S, Halder. A, Verma. S, Banerjee. R. Self-templated chemically stable hollow spherical covalent organic frameworks. *Nat. Commun.,* 2015, **6**, 6786. Doi: 10.1038/ncomms7786.

(17) Xu. F, Xu. H, Chen. X, Wu. D, Wu. Y, Liu. H, Gu. C, Fu. R, Jiang. D. Radical Covalent Organic Frameworks: A General Strategy to immobilize Open-Accessible Polyradicals for High-Performance Capacitive Energy Storage. *Angew. Chem. Int. Ed.,* 2015, **54**, 6814-6818.

(18) Bertrand. G. H. V, Michaelis. V. K, Ong. T. -C, Griffin. R. G, Dincă. M. Thiophene-based covalent organic frameworks. *Proc. Nat. Acad. Sci. USA.,* 2013, **110**, 4923-4928.

(19) Vyas. V. S, Haase. F, Stegbauer. L, Savasci. G, Podjaski. F, Ochsenfeld. C. Lotsch. B. V. A tunable azine covalent organic framework platform for visible light-induced hydrogen generation. *Nat. Commun.,* 2015, **6**, 8508. Doi: 10.1038/ncomms9508.

(20) Tan. J, Namuangruk. S, Kong. W, Kungwan. N, Guo. J, Wang. C. C. Manipulation of Amorphous-to-Crystalline Transformation: Towards the Construction of Covalent Organic Framework Hybrid Microspheres with NIR Photothermal Conversion Ability. *Angew. Chem. Int. End.*, 2016, **55**, 13979-13984.

(21) Xu. H, Chen. X, Gao. J, Lin. J, Addicoat. M, Irle. S, Jiang. D. Catalytic covalent organic frameworks via pore surface engineering. *Chem. Commun.,* 2014, **50**, 1292-1294.

(22) Sun. Q, Aguila. B, Perman. J. A, Nguyen. N. T.-K. Ma. S. Flexibility Matters: Cooperative Active Sites in Covalent Frameworks and Threaded Ionic Polymer. *J. Am. Chem. Soc.,* 2016, **138**, 15790-15796.

(23) Ding. S. Y, Gao. J, Wang. Q, Zhang. Y, Song. W. G, Su. C. Y. Wang. W. Construction of Covalent organic Framework for Catalysis: Pd/COF-LZU1 in Suzuki-Miyaura Coupling Reaction. *J. Am. Chem. Soc.,* 2011, **133**, 19816-19822.

(24) Ma. H. P, Liu. B. L, Li. B, Zhang. L. M, Li. Y. G, Tan. H. Q, Zang. H. Y, Zhu. G. S. Cationic Covalent Organic Frameworks: A Simple Platform of Anionic Exchange for Porosity Tuning and Proton Conduction. *J. Am. Chem. Soc.,* 2016, **138**, 5897-5903.

(25) Hiremath. U. S. Liquid crystalline bis(N-salicylideneaniline)s: synthesis and thermal behaviour of constitutional isomers. *Tetrahedron Lett.,* 2013. **54**, 3419-3423.

Chapter 4

Hybridization of Covalent Organic Frameworks for Carbon Dioxide Capture

Abstract: Covalent organic frameworks (COFs) have emerged as a novel platform for designing advanced organic materials with periodic structures and ordered nanochannels. Post-Combustion CO_2 capture and air separation remained unexplored for covalent organic frameworks, which is essential for directly capturing CO_2 from flue gas. Here, I synthesized a novel COF material, TAPB-DMPTA-COF that is highly porous, stable against water, strong acid and base. The frameworks are designed to constitute hexagonally aligned, dense, mesoporous channels that allow for loading of CO_2-philic Tetraethylenepentamine (TEPA). The result demonstrated that TEPA functionalized COFs material showed high CO_2 uptake and CO_2/N_2 selectivities at low pressure and high temperature.

Keywords: COFs, Carbon Dioxide, Flue Gas, Porous, and Stability

4.1. Introduction

Carbon dioxide emissions into the atmosphere have risen with the rapidly increasing combustion of fossil fuels, which adversely affect the fight against the global warming. Due to the global warming, there are global environmental crisis happened including ocean acidification, sea level rising, and climate change and. The carbon capture and sequestration (CCS) aiming to separate CO_2 gas molecule from flue gas of coal-fired power plants has been built up to lower the anthropogenic CO_2 emissions level.[1-2] however, to date, selective removing of CO_2 from flue gas emissions is still remaining challenging for chemists. Owing to the very low concentration of CO_2 in the atmosphere (ca. 400ppm), effective and economical direct air capture requires a sorbent that optimally combines a number of attributes such as strong CO_2-binding affinity, high capacity, good selectivity against other gas components in the air.[3-4] The removal of CO_2 from low-pressure flue gas mixture is currently dominated by aqueous amine solutions that are highly selective for acid gases. However, these aqueous solutions always have high heat capacity, which makes the regeneration quite energy-intensive and costly. Solid adsorbents with appreciably lower heat capacities are frequently developed as promising alternatives. Moreover, the corrosion and volatility issues of liquid solution could be minimized, even solved in solid adsorbents.

Covalent organic frameworks (COFs) are a novel platform of crystalline porous polymers. COFs materials allow the atomically precise introduction of organic building units into periodicities networks. COFs materials have been developed as a novel materials platform for constructing advanced different organic materials with different applications. Structures and skeleton of COFs materials can be finely predesigned using reticular chemistry and constructed via reversible polycondensation reactions.[5-11] Even though COFs materials with boroxine and boronate-ester linkages showed outstanding crystallinities and porosities, their stability is very weak toward water or protic solvents owing to the easy decomposition of boronate or boroxine bonds.[12-17] On the contrary, COFs with imine, hydrazone, trizine, phenazine and azine linkages showed improved chemical stability while they usually have low

crystallinities and limited porosities.[17-23] Lots of research works have been developed to synthesis these materials with new structures, while outstanding stability, crystallinity and porosity are seldomly achieved in only one COF material except TPB-DMTP-COF published in nature chemistry.[24]

Moreover, to date, various COFs materials have different building blocks' structures have been precisely designed and synthesized. Also, these materials have been investigated as a practical platform for CO_2 uptake and separation. However, most COFs' CO_2 adsorption capacities are unsatisfying at low pressures (below 0.15bar) and high temperature. Especially, pressure below 0.15 bar under 25 and 50 °C, which is identical and similar to industrial applications.[25-29] To better this situation, I present a easy way that functionalize the pore surface of COFs materials by introducing CO_2-philic functional groups and demonstrate its importance and efficiency in change 2D COFs into high-performance CO_2 capture and separation at low pressure and high temperature.

4.2. Synthesis and Characterization

In this work, I developed a novel structure with 2,5-dimethylterephthalaldehyde (DMPTA) as linker and 1,3,5-tris (4-aminophenyl) benzene (TAPB) as knot for the construction of the hexagonal TAPB-DMPTA-COF (Figure 1a). The polycondensation reactions were conducted under solvothermal conditions in a mixed solvent of *n*-butanol and *o*-dicholorobenzene using acetic acid (AcOH) as catalyst at 120 °C for 3 days. The TAPB-DMPTA-COF was obtained as a yellow powder in 89% isolation yield and unambiguously characterized with various analytical methods. Infrared spectroscopy (IR) showed a common stretching vibration band around 1622-1626 cm^{-1}. These peaks were attributed to the imine C=N bond of TAPB-DMPTA-COF (Figure 2). Elemental analysis of the TAPB-BMTA-COF corroborates well with the theoretical values of infinite 2D sheet (Table 2); Field emission scanning electron microscopy (FE-SEM) revealed that the TAPB-DMPTA-COF adopts micrometer-scale flower morphology (Figure 4). Thermal gravimetric analysis (TGA) demonstrated that the TAPB-DMPTA-COF is

4.2.1. Crystal Structure and Porosity

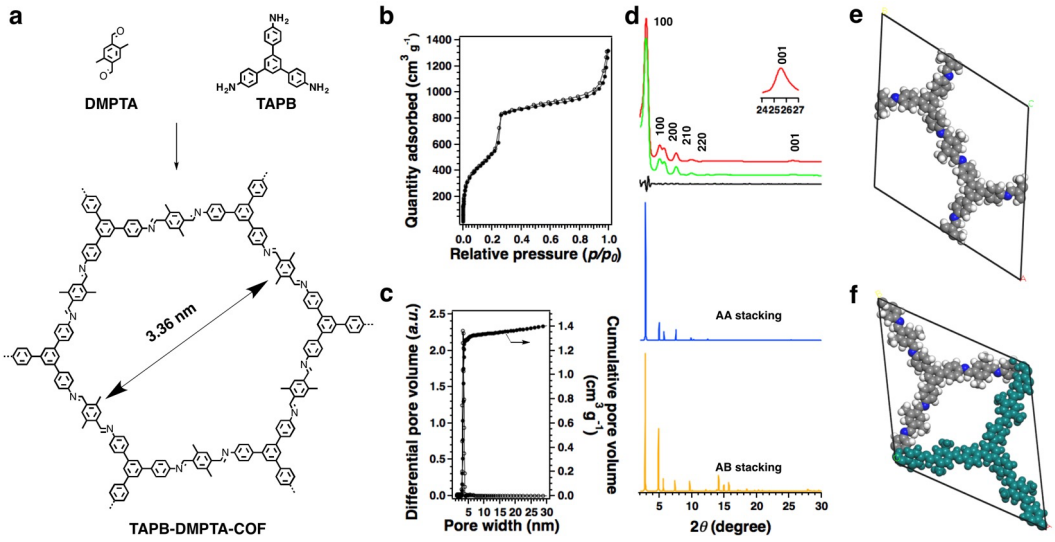

Figure 1. a) Synthesis of TAPB-DMPTA-COF via the poly-condensation of DMPTA (orange) and TAPB (black). **b)** Nitrogen-sorption isotherm curves measured at 77K. **c)** Profiles of the pore size and pore-size distribution. **d)** PXRD profiles of TAPB-DMPTA-COF. Experimentally observed (red), Pawley refined (green) and their difference (black), simulated using the AA stacking mode (blue) and the staggered AB stacking mode (orange). **e)** Unit cell of the AA stacking mode (N, blue; C, grey; H, white). **f)** Unit cell of the AB stacking mode (N, blue; C, grey; H, white)

stable up to 450 °C under N_2 atmosphere (Figure 5).

X-ray diffraction (XRD) measurements in conjunction with computational structural simulations and Pawley refinements (Figure 1) were used to investigate the crystal structures of TAPB-DMPTA-COF. The PXRD pattern of TAPB-DMPTA-COF exhibited six prominent diffraction peaks, with the most-intensive one at 2.92° and five other peaks at 4.94, 5.62, 7.54, 10.1, and 25.4°. These peaks were attributed to the (100), (110), (200), (210), (220) and (001) facets, respectively (Figure 1d, red curve). The Pawley refinement yielded a PXRD pattern (Figure 1d, green curve) that is in good agreement with the experimentally PXRD observed pattern, as evident by their negligible difference (Figure 1d, blacks curve). The AA stacking mode (Figure 1d, blue curve) can reproduce the peak position and intensity of the PXRD pattern. By contrast, the AB stacking mode (Figure 1d, orange curve) resulted in a PXRD pattern

that largely deviates from that of the experimentally observed profile. To construct the optimal crystal structures for this COF, the COFs were revealed by the density-functional tight-binding (DFTB) method including Lennard-Jones dispersion. A hexagonal unit cell (P6) with the parameters of a = b = 37.2718 Å, c = 3.52 Å, α = β = 90°, and γ = 120° (Table 5 and 6) was deduced. The R_p and R_{wp} values are 3.08 and 6.22%, respectively. The presence of the (001) facet at 25.4° was attributed to a π-π stacking distance of 3.6 Å of COFs materials. These properties reveal that the structural ordering further extends along the AA stacking direction, which was perpendicular to the 2D polymer sheets.

Table 1. Calculated crystal stacking energy for TAPB-DMPTA-COF

Stacking	*C* [Å]	Total Energy kcal mol^{-1}	LJ Energy kcal mol^{-1}	Stacking Energy kcal mol^{-1}
AA	3.52	164.848	81.991	81.092
AB	7.04	386.663	226.125	160.538

To investigate the porous structure of TAPB-DMPTA-COF, nitrogen adsorption curves were measured at 77K (Figure 1b). There is a steep N_2 uptake in the low relative pressure region ($P/P_0 < 0.01$) and a sharp uptake amount increase ranging from $P/P_0 = 0.05$ to 0.3, which indicate that the sorption curve is a typical type IV isotherm (Figure 1b) and TAPB-DMPTA-COF is characteristic of mesoporous materials. The Brunauer-Emmett-Teller surface area and pore volume were estimated to be 2894 $m^2\ g^{-1}$ and 1.60 $cm^3\ g^{-1}$, respectively. Notably, the BET surface area was higher than the theoretical BET surface area of 2365 $m^2\ g^{-1}$, suggesting TAPB-DMPTA-COF exhibits high structural integrity and high porosity. The pore size distribution calculated by using the nonlocal density functional theory (NLDFT) method resulted in a pore size of 3.36 nm (Figure 1c), which is similar with the theoretical one. Interestingly, TAPB-DMPTA-COF's surface areas and pore volume are the highest pore volume and BET surface area for 2D COFs.

4.2.2. Stability of COFs

To examine the TAPB-DMPTA-COF's chemical stability, TAPB-DMPTA-COF were dispersed in different solvents such as THF, MeOH, CH_3CN, water (25 and 100 °C), aqueous HCl (12 M), and NaOH (14 M) solutions for one week. After one week, TAPB-DMPTA-COF could keep its pristine crystalline properties, which were indicated by the similar intensities and positions of the PXRD peaks in the powder X-ray diffraction (PXRD) curves. As for TAPB-DMPTA-COF treated one week in THF, MeOH, CH_3CN, water (25 °C), no obvious decrement were found. Moreover,

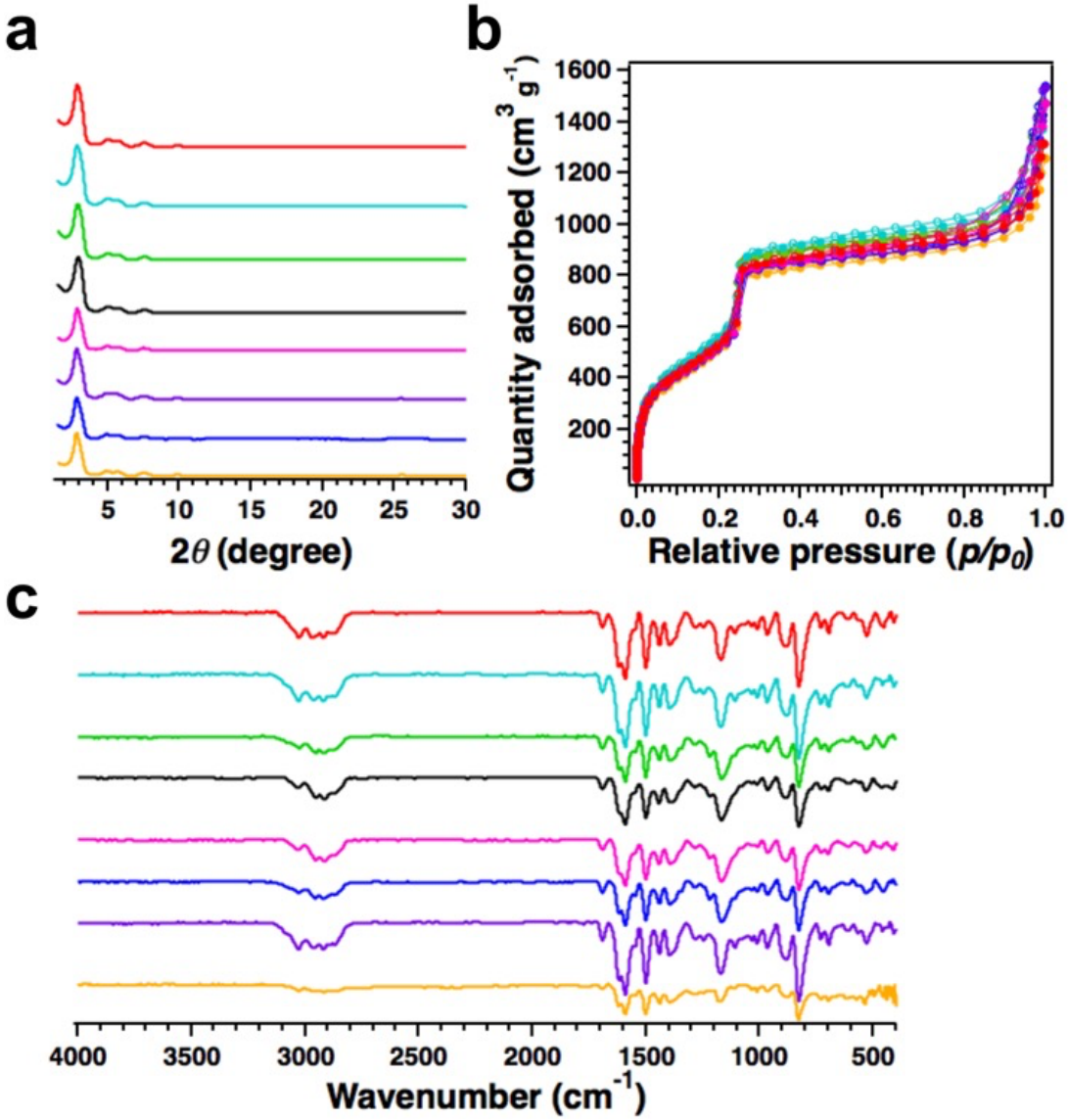

Figure 2. a) PXRD patterns, **b**) N_2 sorption curves, and **c**) FT-IR spectra of TAPB-DMPTA-COF upon one week treatment in different solvents: As-synthesized COF (red curve), THF (sky blue curve), MeOH (green curve), CH_3CN (black curve), H_2O (pink curve), H_2O (100 °C) (purple

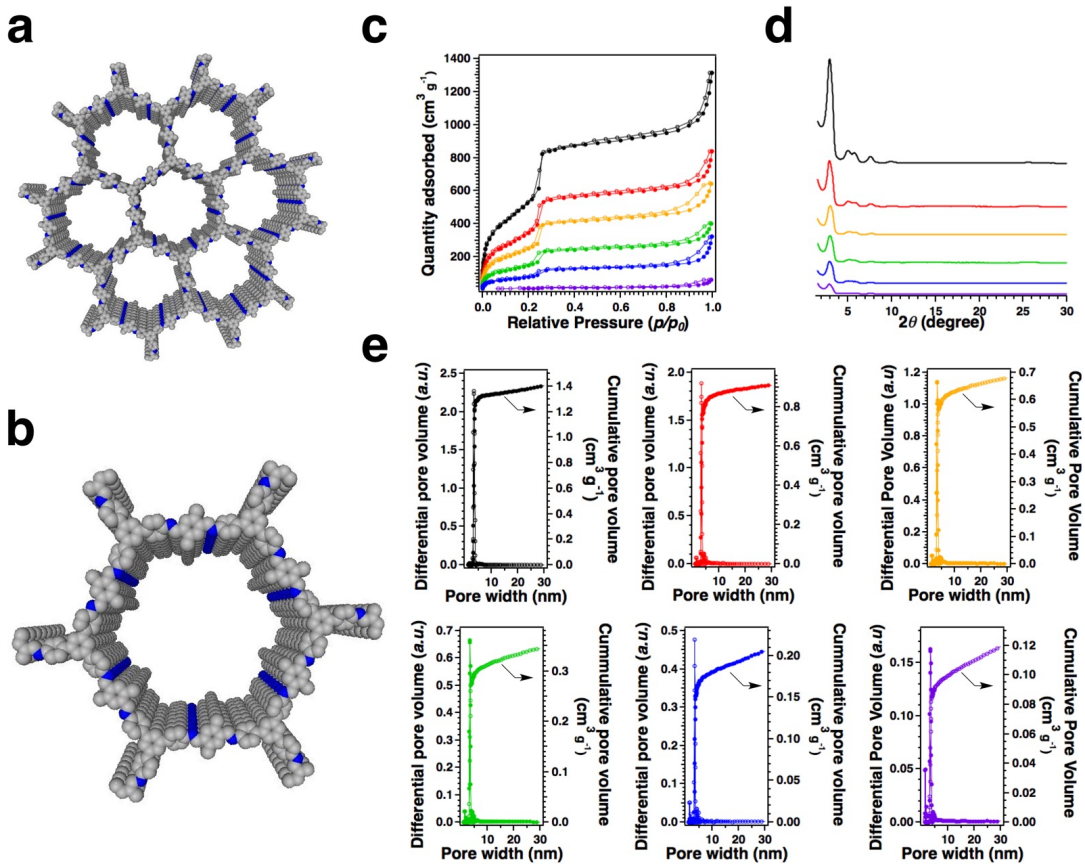

Figure 3. a) Hexagonal structure of TAPB-DMPTA-COF, showing ordered one-dimensional open channels. **b)** TEPA molecules in the channels. **c)** Nitrogen sorption isotherm profiles of TAPB-DMPTA-COF with different TEPA content. **d)** PXRD patterns of TAPB-DMPTA-COF with different TEPA content. **e)** Pore size distribution and cumulative pore volume profiles of the TAPB-DMPTA-COF with different TEPA content. TAPB-DMPTA-COF (black curve), 14wt%TEPA @TAPB-DMPTA-COF (red curve), 30wt%TEPA@TAPB-DMPTA-COF (orange curve), 42wt%TEPA@TAPB-DMPTA-COF (green curve), 52wt%TEPA @TAPB-DMPTA-COF (blue curve), 65wt%TEPA@TAPB-DMPTA-COF (purple curve).

curve), NaOH (14M) (blue curve), HCl (12M) (orange curve), (color in b is the same as that in a). The intensity of TAPB-DMPTA-COF slightly decreased upon treatment in water (100 °C), aqueous HCl (12 M) and aqueous NaOH (14 M) solutions (Figure 2a). When the COF samples were treated one week in THF, MeOH, CH_3CN, water (25 and 100 °C) strong acid and strong base, the BET surface areas 2900，2893，2895，2736，2726, 2693 and 2,710 $m^2\ g^{-1}$ for the COF samples, respectively (Figure 2b). These values are very close to that of the as-synthesized COF (2,894 $m^2\ g^{-1}$). In

addition, the chemical bonds were well protected after treatment one week in different solvent according to the infrared spectra (IR) (Figure 2c).

As shown above, TAPB-DMPTA-COF exhibits an outstanding stability and possesses high crystallinity and porosity toward different solvent for one week. Such a robust open framework provides a very useful material platform for functional exploration. Therefore, TAPB-DMPTA-COF, which has an exceptionally high surface area, pore volume and an extremely robust scaffold, is an ideal platform for incorporating of tetraethylenepentamine (TEPA) CO_2-philic groups into the pore channels for CO_2 capture from flue gas.

4.3. Selective Gas Sorption

Amine functionalized porous materials that have been synthesized commonly exhibited large adsorption enthalpies for CO_2 and high CO_2/N_2 selectivities. It is worthy pointing out that the porosity of the supporting materials will be compromised by the introduction of CO_2-philic functional groups into the pore channel. CO_2 capture capacities under practical conditions are mainly associated with the adsorption Q_{st} and porosity of supporting material. Therefore, loading level of functional groups must be balanced to achieve high loading and moderate porosity. Therefore, the

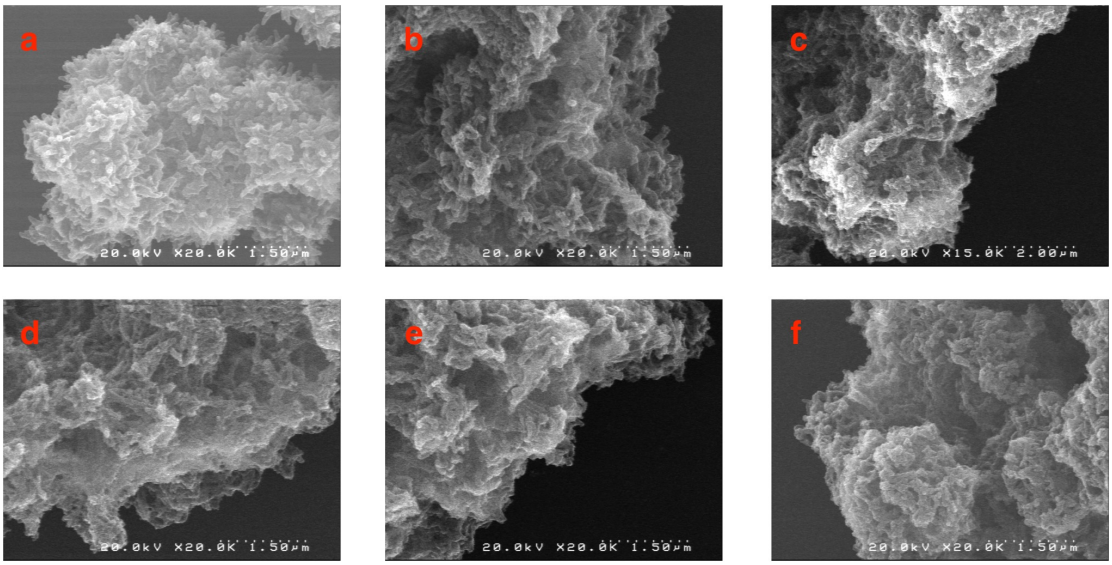

Figure 4. SEM images of **a)** TAPB-DMPTA-COF, **b)** 14wt%TEPA@TAPB-DMPTA-COF, **c)** 30wt%TEPA@TAPB-DMPTA-COF, **d)** 42wt%TEPA@TAPB-DMPTA-COF, **e)** 52wt%TEPA@TAPB-DMPTA-COF, **f)** 65wt%TEPA@TAPB-DMPTA-COF.

loading amount of TEPA into the pore channels of TAPB-DMPTA-COF should be carefully designed to achieve the optimal conditions for CO_2 capture. Figure 3a, b demonstrated that TAPB-DMPTA-COF could accommodate TEPA into its mesopores with different content. After introducing amino source TEPA into the pore channels of TAPB-DMPTA-COF, the PXRD intensity decreased with increasing TEPA loading amount from 0 to 14wt%, 30wt%, 42wt%, 52wt% and 65wt%, respectively (Figure 3d). In addition, the PXRD profiles of TEPA@TAPB-DMPTA-COF showed diffraction patterns that were identical to that of pristine COF, indicating that the lattice structure was not affected by the TEPA incorporating into the pore channels (Figure 3d). At the same time, The BET surface area of TEPA@TAPB-DMPTA-COF decreased dramatically from 2894 to 1834, 1331, 792, 370, and 50 $m^2\ g^{-1}$ with the content of TEPA increasing from 0 to 14wt%, 30wt%, 42wt%, 52wt% and 65wt%, respectively (Figure 3c). Incorporating TEPA would increase the total molecular weight and framework density of COF skeleton leading to the decrease of porosity. Moreover, The pore volume of TEPA@TAPB-DMPTA-COF exhibited decline from 1.60 to 0.98, 0.76, 0.45, 0.26, and 0.12 $cm^3\ g^{-1}$ as the content increase from 0 to 65wt% (Figure 3e). The decreased porosity indicates that the functional amino groups of TEPA within the channel walls filled the space of COF materials. The main pore size of TEPA@TAPB-DMPTA-COF does not change and some new peaks appear according to the calculated pore size distribution curves. These results demonstrate that the TEPA can act as partitions to segregate the channels of TAPB-DMPTA-COF into confined compartments. Scanning electron microscopy (SEM) images of TEPA@TAPB-DMPTA-COF samples display their preserved crystal morphologies (Figure 4). Thus, the overall consideration of the pore size distribution, PXRD measurements, and microscopy images strongly supports that most of the TEPA are distributed inside the TAPB-DMPTA-COF pore channels and serve as partitions. As determined by elemental analysis and thermal gravimetric analysis, the loading amount of TEPA is 14wt%, 30wt%, 42wt%, 52wt%, and 65wt% (Table 2 and Figure 5). The TEPA loading amount can be adjusted by carefully altering the amount of the TEPA concentration in the CH_3CN solution.

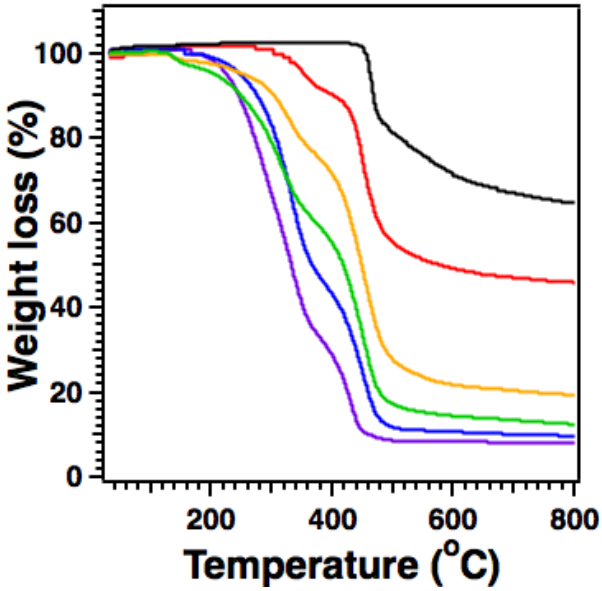

Figure 5. Thermogravimetric curves of TAPB-DMPTA-COF (black curve), 14wt%TEPA@TAPB-DMPTA-COF (red curve), 30wt%TEPA@TAPB-DMPTA-COF (orange curve), 42wt%TEPA@TAPB-DMPTA-COF (green curve), 52wt%TEPA@TAPB-DMPTA-COF (blue curve), 65wt%TEPA@TAPB-DMPTA-COF (purple curve)

Table 2. Elemental analysis results of TAPB-DMPTA-COF and TEPA@TAPB-DMPTA-COF

COFs		C%	H%	N%
TAPB-DMPTA-COF	Calcd.	86.66	5.56	7.78
	Found	85.61	5.39	7.53
14%TEPA@TAPB-DMPTA-COF	Calcd.	81.64	6.4	11.87
	Found	82.2	6.1	10.48
30%TEPA@TAPB-DMPTA-COF	Calcd.	75.9	7.6	16.5
	Found	75.3	7.8	15.95
42%TEPA@TAPB-DMPTA-COF	Calcd.	71.6	8.3	20.1
	Found	61.5	8.8	19.4
52%TEPA@TAPB-DMPTA-COF	Calcd.	68.0	9.0	23.0
	Found	63.1	9.0	20.91
64%TEPA@TAPB-DMPTA-COF	Calcd.	63.7	9.8	26.5
	Found	59.37	9.9	24.06

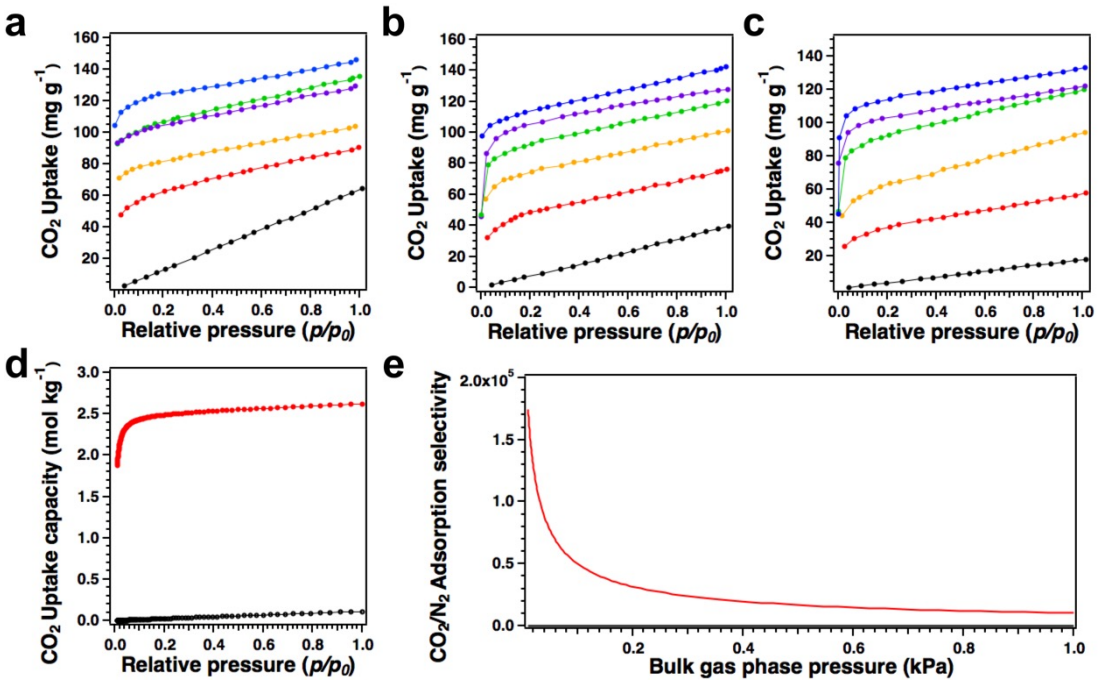

Figure 6. a) CO_2 adsorptions at 273 K. **b)** CO_2 adsorptions at 298 K. **c)** CO_2 adsorptions at 323 K: TAPB-DMPTA-COF (black curve), 14wt%TEPA@TAPB-DMPTA-COF (red curve), 30wt%TEPA@TAPB-DMPTA-COF (orange curve), 42wt%TEPA@TAPB-DMPTA-COF (green curve), 52wt%TEPA@TAPB-DMPTA-COF (blue curve), 65wt%TEPA@TAPB-DMPTA-COF (purple curve). **d)** CO_2 uptake by TAPB-DMPTA-COF (black curve) and 52wt%TEPA@TAPB-DMPTA-COF (red curve) of a 15/85 CO_2/N_2 flue gas mixture at 298 K. **e)** CO_2/N_2 adsorption selectivity of TAPB-DMPTA-COF (black curve) and 52wt%TEPA@TAPB-DMPTA-COF (red curve) for the 15/85 CO_2/N_2 flue gas mixture at 298 K.

Compartments with confined space together with abundant exposed surfaces and amino groups in pore channels, TEPA@TAPB-DMPTA-COF are supposed to be favorable for CO_2 capture and separation. Firstly, I measured the CO_2 adsorption capacity of TEPA@TAPB-DMPTA-COF at pressure up to 1bar and at different temperatures such as 273 K (Figure 6a), 298 K (Figure 6b) and 323 K (Figure 6c). It can be seen that all TEPA@TAPB-DMPTA-COF samples exhibited significantly enhanced CO_2 adsorption compared with pristine TAPB-DMPTA-COF. At 1 bar, the CO_2 uptake capacity of TEPA@TAPB-DMPTA-COF was further enhanced at all tested temperatures when the TEPA content increased from 0 to 52wt%. However, the CO_2 adsorption capacity will decrease when the TEPA content was further increased

to 65wt%. As aforementioned, the surface areas and pore volume of 65wt%TEPA@ TAPB-DMPTA-COF is only 50 m^2 g^{-1} and 0.12 cm^3 g^{-1}, which is not accessible to CO_2 molecules completely. Therefore, further increasing TEPA content is negative to improve the CO_2 capture capacity.

The incorporation of TEPA amine source in TAPB-DMPTA-COF pore channels resulted in materials with excellent CO_2 adsorption characteristics at 273 K, 298 K, 323 K and low pressures, 0.15 bar (Figure 6a, b, c). Coal-fired power plants emit flue gas that contains approximately 15% CO_2 at total pressures of around 1 bar. Thus, CO_2 uptake capacity at around 0.15 bar (similar CO_2 pressure in flue gas), which is similar to the practical post-combustion CO_2 capture applications. Firstly, I measured the CO_2 capture properties of original TAPB-DMPTA-COF under pressures to 1 bar and different temperatures at 273 K, 298 K, and 323 K. TAPB-DMPTA-COF only takes up 11, 6.6, and 3.9 mg g^{-1} CO_2 at 0.15 bar and 273 K, 298 K, and 323 K, respectively. Unlike the pristine COFs, TEPA@TAPB-DMPTA-COF showed dramatically increment in CO_2 adsorption capacities under the same conditions. Especially, 52wt%TEPA@TAPB-DMPTA-COF takes up 122.8, 111.4, and 111.1 mg g^{-1} of CO_2 at 0.15 bar and at 273K, 298K, and 323K, respectively. These capacities are 11.2-, 16.9- and 28.5-fold higher than TAPB-DMPTA-COF's. These values are the highest CO_2 capture performance for reported 2D and 3D COFs so far. In addition, these CO_2 capture performances are similar to the reported top-performing materials, such as PPN-6-CH_2DETA (11.8 wt% at 295 K and 0.15 bar) and mmen-CuBTTri (9.5 wt% at 298 K). [30] To investigated the CO_2/N_2 selectivity of the 52wt%TEPA@TAPB-DMPTA-COF under flue-gas conditions with single-gas isotherms, I used the ideal adsorbed solution theory (IAST) model of Myers and Prausnitz[31] along with the pure component isotherm fits to determine the molar loadings in the mixture for specified partial pressures in the bulk gas phase. Based on the pure-component isotherm fits and I investigated the adsorption selectivity. According to the IAST method (SI), the selectivity, S_{ads} was defined as $(q_1/q_2)/(p_1/p_2)$. Configurational-bias Monte Carlo (CBMC) was compared with mixture adsorption' simulating method. Using IAST calculations method for evaluating the gas molecule

component loadings for different mixtures for widely porous organic materials built. I utilized TAPB-DMPTA-COF and 52wt%TEPA@TAPB-DMPTA-COF materials for separating CO_2/N_2 mixture, which is similar with CO_2 removing from flue gases. According to the earlier research work of Mason et al, the CO_2/N_2 mixtures containing 15% CO_2 and 85% N_2 were assumed [32] The CO_2 and N_2 capture properties' IAST method simulation for 15/85 CO_2/ N_2 gas molecule mixture at 298K was shown in the Figure 4d. It is worthy to point out that 52wt%TEPA@TAPB-DMPTA-COF could capture 2.62 mol kg^{-1} CO_2 at 100 kPa (= 1 bar) while DMPTA-TAPB-COF could only adsorb 0.11 mol kg^{-1} (Figure 6d). By contrast, DMPTA-TAPB-COF could capture 0.118 mol $kg^{-1}N_2$, which is higher than that of 52wt%TEPA@TAPB-DMPTA-COF (0.038 mol kg^{-1}, Figure 6d). The CO_2/N_2 selectivities of 52wt%TEPA@TAPB-DMPTA-COF can be compared to any reported materials (Figure 6e).

In order To better understand the properties of CO_2 gas molecule adsorption properties, the CO_2 adsorption curves measured at pressures up to 1 bar and different temperatures at 273 and 298 K were used to calculate the isosteric heat of adsorption (Q_{st}). Figure 5a exhibited the adsorption enthalpies as a function of CO_2 loading. Figure 5a exhibited that 52wt%TEPA@TAPB-DMPTA-COF retained its strong CO_2 interactions to a relatively high CO_2 loading amount due to the amino functionalization, which is consistent with its high CO_2 uptake capacity at low pressure. The Q_{st} is decreasing with CO_2 loading amount further increased higher than 2.5 mol kg^{-1}, which indicates that most CO_2 was captured at low pressure (Figure 7a). In addition, the preservation of high isosteric heats of adsorption is important for solid adsorbents so as to maintain high CO_2-uptake capacity at elevated temperatures. From 298 K to 323 K, the CO_2 adsorption capacity of 52wt%TEPA@TAPB-DMPTA-COF at 0.15 bar only dropped slightly from 111.4 to 111.1 mg g^{-1} (Figure 6c). Therefore, 52wt%TEPA@TAPB-DMPTA-COF has potential application for realistic post-combustion CO_2 capture and separation.

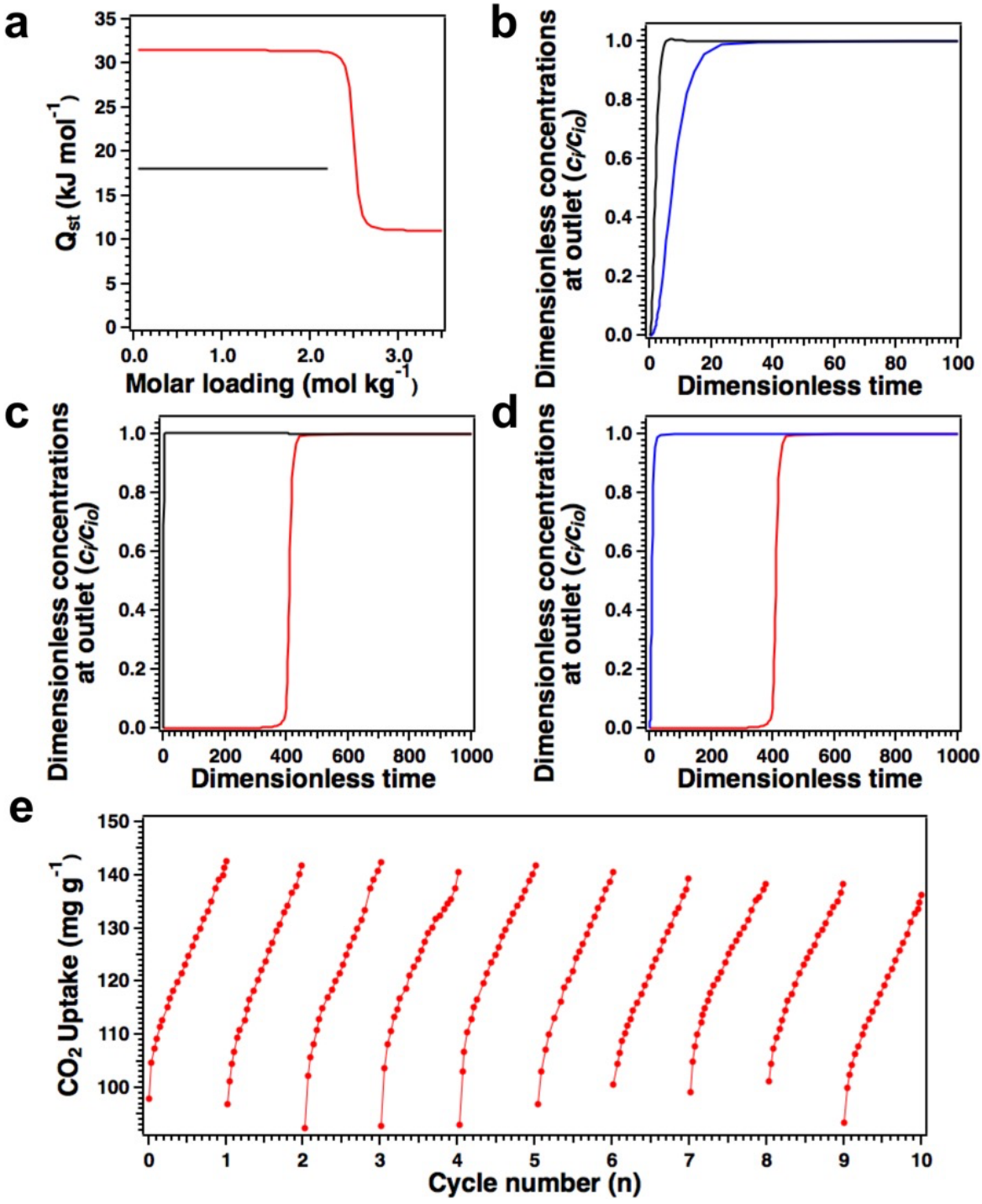

Figure 7. Transient breakthrough simulations and cycle performance. a) Isosteric heats of adsorption Q_{st} for the adsorption of CO_2. **b)** Flue gas breakthrough profiles of TAPB-DMPTA-COF. **c)** Flue gas breakthrough profiles of TAPB-DMPTA-COF-52wt%TEPA. **d)** Comparison of $\%CO_2$ at the adsorber outlet at 298 K (blue curve: TAPB-DMPTA-COF, red curve: 52wt%TEPA@TAPB-DMPTA-COF). **e)** Cycle performance of 52wt%TEPA@TAPB-DMPTA-COF at 298 K.

Breakthrough simulations were conducted with a finely method, which was explored by Krishna and Long to investigate the gas molecule separation capacity of adsorbents materials in the condition of kinetic flowing gas conditions. As for a pressure-swing adsorption (PAS) process, these simulations could exhibit the separation properties. This method is an energy- efficient strategy for industrial-scale adsorption. Selectivity and capacity factors determine the performance of a COF material within a PSA unit. The typical breakthrough curves for TAPB-DMPTA-COF and 52wt%TEPA@TAPB-DMPTA-COF were shown in the Figure 7b and c. The dimensionless time is the x-axis (t) defined to be dividing the actual time (t) defined to be the characteristic time, Le/m (SI). Obviously, the breakthrough time of 52wt%TEPA@TAPB-DMPTA-COF is 400. The breakthrough time is much longer than TAPB-DMPTA-COF' breakthrough time (20). In terms of mol% CO_2 at the outlet, the breakthrough properties of TAPB-DMPTA-COF and 52wt%TEPA@TAPB-DMPTA-COF based on a function of dimensionless time for operating at a total pressure of 100 kPa were compared. The breakthrough time of 52wt%TEPA@TAPB-DMPTA-COF (red curve) is much longer than TAPB-DMPTA-COF' breakthrough time (blue curve). Longer breakthrough times are essential and key point for enhanced CO_2 capture. In order to evaluate COFs materials, outlet gas purity to be < 0.05 mol% CO_2 were chosed. I evaluated the breakthrough times, t_{break}, for each COF material according to the purity specification. According to the material balance on the absorber, I measured CO_2 captured amount during the time interval 0–t_{break}.

These results exhibited that loading amino source into COFs pore channels is an efficient way to change a common COFs materials into an outstanding CO_2 adsorption materials. The effects of amino source on CO_2 capture properties are positive and profound for both capacity and selectivity. In order to evaluate the CO_2 adsorption cycling performance of 52wt%TEPA@TAPB-DMPTA-COF, vacuum and temperature swings were conducted using a belsorp mini II analyzer. Firstly, the COFs samples were saturated with CO_2 up to 1.0 bar at 298K. And then place the COFs samples under high oil vacuum for 180 min heating at 353K to remove the

adsorbed CO_2 gas molecule. Notably, there is no obvious decrease observed in capture capacity over ten cycles. These reveal that COFs materials could be complete desorption during each regeneration cycle and excellent cycling performance of COFs materials. Through 52wt%TEPA@TAPB-DMPTA-COF has high adsorption enthalpies, the regeneration energies is still lower than that of amine solutions (ca. 50-100 kJ mol^{-1}). Therefore, the energy consumption of regeneration for 52wt%TEPA@TAPB-DMPTA-COF is still lower than amine solutions.

4.4. Conclusion

In summary, I have developed a new mesoporous COF with good crystallinity, porosity and stability. The layered and open porous structure of COF material can be retained after loading amine source. The amine functionalized COFs exhibited high CO_2 uptake capacity and CO_2/N_2 selectivities at low pressure and high temperature, which is useful for directly capturing CO_2 from flue gas. The present amino functionalized COFs method would be important to explore 2D COFs materials for high-performance CO_2 capture and separation.

4.5. Methods

Synthesis of TAPB-DMPTA-COF

A 10-ml Pyrex tube was filled with monomer DMPTA (22.8 mg, 0.141 mmol), TAPB (32.7 mg, 0.094 mmol), 0.5 ml *o*-DCB, 0.5 ml BuOH and 0.1 ml AcOH (6 M) as catalyst. Three freeze-pump-thaw cycles was used to remove the oxygen in the reaction tube. The reaction mixture tube was sealed by flame gun under vacuum and heated at 120 °C for 3 days. The reaction mixture system was cooled to room temperature using water and the yellow COF solid was collected by centrifugation, and washed with THF five times (each time 2 ml). The COFs powders were dried at 120 °C under oil vacuum overnight to yield the DMPTA-TAPB-COF in an isolated yield of 89%.

Preparation of TEPA@TAPB-DMPTA-COF

The TEPA@TAPB-DMPTA-COF adsorbents were prepared by wet impregnation method. The detailed process was as follows. First, before the impregnation, the

TAPB-DMPTA-COF powders were heated at 120 °C under oil vacuum condition for 12 h, removing the adsorbed water. Second, the 0.8 ml TEPA was dissolved in 1 mL anhydrous CH_3CN under stirring for 30 min. Also, 15mg TAPB-DMPTA-COF powders were distributed into 3 ml anhydrous CH_3CN solution under stirring for 24 hours. Thirdly, 0.1, 0.3, 0.5, 0.7, and 0.9 ml were added into TAPB-DMPTA-COF solution under stirring for 1 hour to obtain desired TEPA loading amount, respectively. Finally, the resulting TEPA@TAPB-DMPTA-COF sample was obtained through filtration and dried over night at room temperature for 12 hours.

Stability test

The COF samples (30 mg) were kept in 2 ml of THF, MeOH, CH_3CN, HCl (12M), NaOH (14M), water (25 °C) and boiling water (100 °C) for seven days. The samples were washed with THF or water, dried under vacuum at 120 °C for 12 hours. Then, the COFs samples were investigated using PXRD, infrared spectroscopy (IR) and nitrogen-sorption isotherm measurements.

4.6. Fitting of Pure Component Isotherms

The experimentally measured CO_2 isotherms at 273K, 298 K, and 323 K in TEPA@TAPB-DMPTA-COF and pristine TAPB-DMPTA-COF samples were calculated with good accuracy with the dual-site Langmuir model

$$q = q_{A,sat}\frac{b_A p}{1+b_A p} + q_{B,sat}\frac{b_B p}{1+b_B p} \tag{1}$$

with (b_A, and b_B) T-dependent parameters

$$b_A = b_{A0}\exp\left(\frac{E_A}{RT}\right); \quad b_B = b_{B0}\exp\left(\frac{E_B}{RT}\right) \tag{2}$$

The experimentally measured CO_2 isotherms at 273K, 298 K, and 323 K in pristine TAPB-DMPTA-COF were fitted with good accuracy with the 1-site Langmuir model

$$q = q_{sat}\frac{bp}{1+bp} \tag{3}$$

with T-dependent parameter b

$$b = b_0 \exp\left(\frac{E}{RT}\right)$$

The experimentally measured N_2 isotherms at 273K, 298 K, and 323 K in both TEPA@TAPB-DMPTA-COF and pristine TAPB-DMPTA-COF were fitted with good accuracy with the 1-site Langmuir model.

The isotherm fit parameters for the two COFs are provided in Table 3 and Table 4.

Table 3. Isotherm fits parameters for CO_2 and N_2 in 52wt%TEPA@TAPB-DMPTA-COF.

	Site A			Site B		
	$q_{A,sat}$ mol kg^{-1}	b_{A0} Pa^{-1}	E_A kJ mol^{-1}	$q_{B,sat}$ mol kg^{-1}	b_{B0} Pa^{-1}	E_B kJ mol^{-1}
CO_2	2.5	6×10^{-8}	31.5	1.9	5.8×10^{-8}	11
N_2	20	1.19×10^{-14}	33			

Table 4. Isotherm fits parameters for CO_2 and N_2 in pristine TAPB-DMPTA-COF

	q_{sat} mol kg^{-1}	b_0 Pa^{-1}	E kJ mol^{-1}
CO_2	22	2.55×10^{-10}	18
N_2	0.7	1.05×10^{-14}	47

Isosteric heat of adsorption

The binding energies between CO_2 and TEPA@TAPB-DMPTA-COF or pristine TAPB-DMPTA-COF are calculated according to the isosteric heat of adsorption(Q_{st})

$$Q_{st} = RT^2\left(\frac{\partial \ln p}{\partial T}\right)_q$$

These Q_{st} values were calculated according to the pure gas molecule component isotherm fits' analytic differentiation

IAST calculations of adsorption selectivities

To build the feasibility of CO_2/N_2 separations, the Ideal Adsorbed Solution Theory (IAST) established by Myers and Prausnitz wer used for calculations.[4] The adsorption selectivities and uptake capacities were determined for 15/85 CO_2/N_2 mixtures at 298 K. Due to amine functionality the CO_2/N_2 adsorption selectivity increases by more than 3 orders of magnitude.

Transient breakthrough simulations

COFs samples' adsorption selectivity and uptake capacity exhibited the industrial performance fixed bed adsorbers. In order to compare various MOFs materials, I performed transient breakthrough simulations according to the simulation method in the literature.[5] As for the breakthrough simulations, the below parameters were applied: voidage of packed bed ($\varepsilon = 0.4$); superficial gas velocity at inlet; $u = 0.04$ m/s length of packed bed, L = 0.3 m. The framework densities of TEPA@TAPB-DMPTA-COF and pristine TAPB-DMPTA-COF are 240 kg m^{-3}, and 630 kg m^{-3}, respectively. Transient breakthroughs were determined for both 15/85 CO_2/N_2 mixtures in fixed beds operating at 298 K and total pressure of 100 kPa.

Supplementary Notation

b	Langmuir constant, Pa^{-1}
L	length of packed bed adsorber, m
p_i	partial pressure of species *i* in mixture, Pa
p_t	total system pressure, Pa
q_i	component molar loading of species *i*, mol kg^{-1}
q_t	total molar loading in mixture, mol kg^{-1}
q_{sat}	saturation loading, mol kg^{-1}
R	gas constant, 8.314 J mol^{-1} K^{-1}
t	time, s
T	absolute temperature, K
u	superficial gas velocity in packed bed, m s^{-1}
z	distance along the adsorber, and along membrane layer, m

Greek letters

ε	voidage of packed bed, dimensionless
τ	time, dimensionless

Subscripts

i	referring to component *i*
t	referring to total mixture

Table 5. Atomistic coordinates for the AA-stacking mode of TAPB-DMPTA-COF optimized by using DFTB$^+$ method (space group *P6*, a = b = 36.9127 Å; c = 4.1241 Å, $\alpha = \beta = 90^o$ and $\gamma = 120^o$.

Atom	***x/a***	***y/b***	***z/c***
C1	0.28976	0.64139	0.55868
C2	0.31518	0.62343	0.55861
C3	0.24365	0.61467	0.56057
C4	0.37304	0.5916	0.39498
C5	0.39771	0.57323	0.39744
C6	0.43546	0.5919	0.56888
C7	0.44834	0.62976	0.72965
C8	0.4234	0.6478	0.7269
N9	0.46243	0.57524	0.57192
C10	0.44612	0.53497	0.57207
C11	0.47306	0.51647	0.56812
C12	0.45639	0.47284	0.56762
C13	0.48356	0.45722	0.56726
H14	0.30091	0.58941	0.55889
H15	0.34391	0.57707	0.25659
H16	0.38812	0.54461	0.25932
H17	0.4777	0.64432	0.86445
H18	0.43332	0.67687	0.85963
H19	0.41162	0.51332	0.58125
H20	0.4713	0.42344	0.5676
C21	0.58995	0.55686	0.56749
H22	0.60476	0.55232	0.35371
H23	0.60478	0.55238	0.78144
H24	0.59664	0.58914	0.56721

Table 6. Atomistic coordinates for the refined unit cell parameters for TAPB-DMPTA-COF via Pawley refinement (space group *P6*, a = b = 36.5281 Å; c = 3.41249 Å, $\alpha = \beta = 90^{o}$ and $\gamma = 120^{o}$.

Atom	***x/a***	***y/b***	***z/c***
C1	0.29278	0.64806	0.55868
C2	0.31846	0.62991	0.55861
C3	0.24618	0.62106	0.56057
C4	0.37692	0.59776	0.39498
C5	0.40185	0.57919	0.39744
C6	0.43999	0.59806	0.56888
C7	0.453	0.63631	0.72965
C8	0.4278	0.65454	0.7269
N9	0.46724	0.58122	0.57192
C10	0.45077	0.54054	0.57207
C11	0.47798	0.52185	0.56812
C12	0.46114	0.47776	0.56762
C13	0.48859	0.46198	0.56726
H14	0.30404	0.59554	0.55889
H15	0.34749	0.58307	0.25659
H16	0.39216	0.55027	0.25932
H17	0.48267	0.65102	0.86445
H18	0.43783	0.68392	0.85963
H19	0.4159	0.51866	0.58125
H20	0.4762	0.42785	0.5676
C21	0.59609	0.56265	0.56749
H22	0.61105	0.55806	0.35371
H23	0.61107	0.55812	0.78144
H24	0.60285	0.59527	0.56721

Table 7. Atomistic coordinates for the refined unit cell parameters for TAPB-DMPTA-COF via Rietveld refinement (space group *P6*, a = b = 37.64976 Å; c = 4.1249 Å, $\alpha = \beta = 90^{o}$ and $\gamma = 120^{o}$.

Atom	***x/a***	***y/b***	***z/c***
C1	0.29302	0.6486	0.55868
C2	0.31873	0.63044	0.55861
C3	0.24639	0.62158	0.56057
C4	0.37723	0.59826	0.39498
C5	0.40218	0.57967	0.39744
C6	0.44036	0.59856	0.56888
C7	0.45338	0.63684	0.72965
C8	0.42816	0.65509	0.7269
N9	0.46763	0.58171	0.57192
C10	0.45114	0.54099	0.57207
C11	0.47838	0.52228	0.56812
C12	0.46152	0.47816	0.56762
C13	0.489	0.46236	0.56726
H14	0.30429	0.59604	0.55889
H15	0.34778	0.58356	0.25659
H16	0.39249	0.55073	0.25932
H17	0.48307	0.65157	0.86445
H18	0.4382	0.68449	0.85963
H19	0.41625	0.51909	0.58125
H20	0.4766	0.42821	0.5676
C21	0.59659	0.56312	0.56749
H22	0.61156	0.55853	0.35371
H23	0.61158	0.55859	0.78144
H24	0.60335	0.59577	0.56721

Table 8. Atomistic coordinates for the AB-stacking mode of TAPB-DMPTA-COF optimized by using DFTB+ (space group *P3*, a = b = 37.1423 Å; c = 6.7783 Å, α = β = 90° and γ = 120°.

Atom	*x/a*	*y/b*	*z/c*
C1	-0.0243	1.01933	0.24802
C2	-0.04388	0.97556	0.24805
H3	-0.0434	1.03453	0.24838
C4	0.36068	0.6508	0.45455
C5	0.37682	0.6942	0.45425
H6	0.3822	0.63834	0.45271
C7	0.05029	0.95998	0.2507
C8	0.08931	0.97836	0.14996
C9	0.11368	0.95941	0.15587
C10	0.09927	0.92122	0.26096
C11	0.06046	0.90291	0.36412
C12	0.0363	0.92208	0.3578
H13	0.1005	1.00783	0.06419
H14	0.14392	0.97366	0.07502
H15	0.04964	0.87398	0.45383
H16	0.00633	0.90786	0.44154
C17	0.21436	0.7912	0.36616
N18	0.19737	0.75077	0.38514
C19	0.10854	0.86318	0.27576
N20	0.12578	0.90381	0.27052
H21	0.24916	0.81245	0.36229
H22	0.07386	0.84189	0.26295
C23	0.27693	0.69975	0.44525
C24	0.23925	0.67871	0.33345
C25	0.2131	0.69554	0.31651
C26	0.22455	0.73433	0.40875
C27	0.2615	0.75486	0.52697
C28	0.28736	0.73768	0.54402
H29	0.23077	0.64905	0.25522
H30	0.18416	0.67945	0.22511
H31	0.26966	0.78418	0.60792
H32	0.31607	0.75378	0.63736
C33	0.18787	0.81018	0.34359
C34	0.14421	0.78403	0.33454
C35	0.1174	0.80012	0.31127
C36	0.13491	0.84404	0.29756
C37	0.17858	0.87018	0.30695

C38	0.20539	0.8541	0.32908
H39	0.13144	0.75004	0.3459
H40	0.19133	0.90419	0.29603
C41	0.1165	0.36857	0.33823
C42	0.22925	0.29997	0.30205
H43	0.08392	0.34327	0.32483
H44	0.12274	0.39094	0.21153
H45	0.1198	0.38504	0.48548
H46	0.22577	0.28331	0.15524
H47	0.22313	0.27776	0.42934
H48	0.26185	0.32528	0.31437

4.7. References

(1) Sanz-Pérez, E. S. Murdock, C. R. Dias, S. A. Jones, C. W. Direct capture of CO_2 from ambient air. *Chem. Rev.* 2016, **116**, 11840-11876.

(2) Hansen, J. Ruedy, R. Sato, M. Lo, K. Global surface temperature change. *Rev. Geophys*. 2010, **48**, RG4004.

(3) Lewis, T. Faubel, M. Winter, B. Hemminger, J. C. CO_2 capture in amine-based aqueous solution: Role of the gas-solution interface. *Angew. Chem. Int. Ed*. 2011, **50**, 10178-10181.

(4) MacDowell, N. Florin, N. Buchard, A. Hallett, J. Galindo, A. Jacson, G. Adjiman, C. S. Williams, C. K. Shah, N. Fennell, P. An overview of CO_2 captures technologies. *Energy. Environ. Sci.* 2010, **3**, 1645-1669.

(5) Feng, X. Ding, X. S. Jiang, D. L. Covalent organic frameworks. *Chem. Soc. Rev*, 2012, **41**, 6010-6022.

(6) Huang, N. Zhai, L. P. Coupry, D. E. Addicoat, M. A. Okushaita, K. Nishimura, K. Heine, T. Jiang, D. L. Multiple-component covalent organic frameworks. *Nature. Commun*. 2016, **7**. 12325. DOI: 10.1038/ncomms12325.

(7) Huang, N. Wang, P. Jiang, D. L. Covalent organic frameworks: A materials platform for structural and functional designs. *Nat. Rev. Mat*, 2016, **1**, 16068. DOI: 10. 1038/natrevmats.2016.68.

(8) Dalapati, S. Jin, E. Q. Addicoat, M. Heine, T. Jiang, D. L. Highly emissive covalent organic frameworks. *J. Am. Chem. Soc*. 2016, **138**, 5797-5800.

(9) Ascherl, L. Sick, T. Margraf, J. T. Lapidus, S. H. Calik, M. Hettstedt, C. Karaghiosoff, K. Döblinger, M. Clark, T. Chapman, K. W. Auras, F. Bein, T. Molecular docking sites designed for the generation of highly crystalline covalent organic frameworks. *Nat. Chem*. 2016, **8**, 310-316. Doi: 10.1038/nchem.2444.

(10) Diercks, C. S. Yaghi, O. M. The atom, the molecule, and the covalent organic framework. *Science*, 2017, **355**, 923.

(11) Waller, P. J. Gándara, F. Yaghi, O. M. Chemistry of Covalent Organic Frameworks. *Acc. Chem. Res.* 2015, **48**, 3053-3063.

(12) Cote, A. P. El-Kaderi, H. M. Furukawa, H. Hunt, J. R. Yaghi, O. M. Reticular synthesis of microporous and mesoporous 2D covalent organic frameworks. *J. Am. Chem. Soc.* 2007, **129**, 12914–12915.

(13) Wan, S. Guo, J. Kim, J. Ihee. H. Jiang, D. L. A belt-shaped, blue luminescent, and semiconducting covalent organic framework. *Angew. Chem. Int. Ed.* 2008, **47**, 8826–8830.

(14) Tilford, R. W. Mugavero, S. J. Pellechia, P. J. Lavigne, J. J. Tailoring microporosity in covalent organic frameworks. *Adv. Mater.* 2008, **20**, 2741–2746.

(15) Wan, S. Guo, J. Kim, J. Ihee, H. Jiang, D. L. A photoconductive covalent organic framework: self-condensed arene cubes composed of eclipsed 2D polypyrene sheets for photocurrent generation. *Angew. Chem. Int. Ed.* 2009, **48**, 5439–5442.

(16) Crowe, J. W. Baldwin, L. A. Mcgrier, P. L. Luminescent covalent organic frameworks containing a homogeneous and heterogeneous distribution of dehydrobenzoannulene vertex units. *J. Am. Chem. Soc*. 2016, **138**, 10120–10123.

(17) Spitler, E. L. Dichtel, W. R. Lewis acid-catalysed formation of two-dimensional phthalocyanine covalent organic frameworks. *Nat. Chem. 2010,* **2**, 672–677.

(18) Zhu, Y. L. Wan, S. Jin, Y. H. Zhang, W. Desymmertrized vertex design for the synthesis of covalent organic frameworks with periodically heterogeneous pore structures. *J. Am. Chem. Soc*. 2015, **137**, 13772–13775.

(19) Uribe-Romo, F. J. Doonan, C. J. Furukawa, H. Oisaki, K.s Yaghi, O. M. Crystalline covalent organic frameworks with hydrazone linkages. *J. Am. Chem. Soc*. 2011, **133**, 11478–11481.

(20) Kandambeth, S. Mallick, A. Lukose, B. Mane, M. V. Heine, T. Banerjee, R. Construction of crystalline 2D covalent organic frameworks with remarkable chemical (acid/base) stability via a combined reversible and irreversible route. *J. Am. Chem. Soc.* 2012, **134**, 19524–19527.

(21) Dalapati, S. Jin, S. B. Gao, J. Xu, Y. H. Nagai, A. Jiang, D. L. An azine-linked

covalent organic framework. *J. Am. Chem. Soc.* 2013, **135**, 17310–17313.

(22) Kuhn, P. Antonietti, M. Thomas, A. Porous, covalent triazine-based frameworks prepared by ionothermal synthesis. *Angew. Chem. Int. Ed.* 2008, **47**, 3450–3453.

(23) Huang, N. Zhai, L. P. Xu, H. Jiang, D. L. Stable covalent organic frameworks for exceptional mercury removal from aqueous solutions. *J. Am. Chem. Soc*. 2017, **139**, 2428–2434.

(24) Xu, H. Gao, J. Jiang, D. L. Stable, crystalline, porous, covalent organic frameworks as a platform for chiral organicatalysts. *Nat. Chem.* 2015, **7**, 905–912.

(25) Huang, N. Chen, X. Krishna, R. Jiang, D. L. Two-dimensional covalent organic frameworks for carbon dioxide capture through channel-wall functionalization. *Angew. Chem. Int. Ed.* 2015, **54**, 2986–2990.

(26) Huang, N. Krishna, R. Jiang, D. L. Tailor-Made Pore Surface Engineering in Covalent Organic Frameworks: Systematic Functionalization for Performance Screening. *J. Am. Chem. Soc.* 2015, **137**, 7079–7082.

(27) Li, Z. P. Feng, X. Zou, Y. C, Zhang, Y. W. Xia, H. Liu, X. M. Mu, Y. A 2D azine-linked covalent organic framework for gas storage applications. *Chem. Commun*. 2014, **50**, 13825-13828.

(28) Alahakoon, S. B. Thompson, C. M. Nguyen, A. X. Occhialini, G. McCandless, G. T. Smaldone, R. A. An azine-linked hexaphenylbenzene based covalent organic framework. *Chem. Commun.* 2016, **52**, 2843-2845.

(29) Kang, Z. X. Peng, Y. W. Qian, Y. H. Yuan, D. Q. Addicoat, M. A. Heine, T. Hu, Z. G. Tee, L. Guo, Z. G. Zhao, D. Mixed matrix membranes (MMMs) comprising exfoliated 2D covalent organic frameworks (COFs) for efficient CO_2 separation. *Chem. Mater*, 2016, **28**, 1277-1285.

(30) Lu, W. G. Sculley, J. P. Yuan, D. Q. Krishna, R. Wei, Z. W. Zhou, H. C. Polyamine-tethered porous polymer networks for carbon dioxide capture from flue gas. *Angew. Chem. Int. Ed.* 2012, **51**, 7480–7484.

(31) Myers, A. L. Prausnitz, J. M. Thermodynamics of mixed-gas adsorption. *AIChE J.* 1965, **11**, 121-127.

(32) Mason, J. A. Sumida, K. J. Herm, Z. R. Krishna, R. Long, J. R. Evaluating metal–organic frameworks for post-combustion carbon dioxide capture via temperature swing adsorption. *Energy. Environ. Sci.* 2011, **4**, 3030-3040.

Chapter 5
Summary and perspectives

In summary, COFs materials represent a new synthetic era in the filed of organic materials. COFs are a new class of porous architectures that allow the precisely integration of organic units with atomic precision into long-range-ordered two (2D) and three-dimensional (3D) networks. From a synthetic point of view, COFs are intriguing scaffolds since they allow a new degree of control of porosity, composition and component positions. These promising features such as highly flexible molecular design, permanent porosity, controllable pore size and the diversity of building units have stimulated the progress of functional application exploration such as catalyst, energy storage and gas adsorption and separation.

CO_2 is the primary greenhouse gas whose release amount and concentration in atmosphere are continuously increasing due to the increasing population and industrial development. Considering the detrimental effects including global climate warming, rising sea level and anthropogenic climate change, developing effective technologies and new materials for CO_2 capture and sequestration is urgent and essential.

Despite the recent advances in chemistry of COFs, a principle for the backbone design of COFs targeting for CO_2 adsorption remains to be explored. In chapter 2 and 3, I succeeded in disclosing such a principle by integrating triarylamine that has very weak basicity in attracting CO_2 as a building block to the backbone of COFs and elucidated its prominent impact on CO_2 adsorption. Our results reveal that the backbone of COFs plays a key role in CO_2 uptake. The collective effect of thetriarylamine backbone is prominent and could not be underestimated. Given with the availability of organic units with strong basicity, our results reveal a general principle for the backbone design of COFs targeting for CO_2 uptake and separation.

In addition, pore-wall surface engineering of conventional COFs has been proved as an effective strategy for enhancing the adsorption capacity by introducing functional groups such as carboxylic acid and alkyl amine units to the pore walls that trigger strong interactions with CO_2. Among various linkages reported, only azine linkage has shown a potential for increasing the

CO_2 adsorption capacity. However, the CO_2 adsorption capacities of most COFs are unsatisfying at low pressures and high temperature, especially below 0.15 bar under 25 and 50 °C, which is relevant to practical applications. Moreover, selective capture of CO_2 from flue gas emissions still remains challenging to date for researchers. Because of the CO_2 low concentration in the atmosphere (ca. 400ppm), effective and economical direct air capture requires a sorbent that optimally combines a number of attributes such as strong CO_2-binding affinity, high capacity, good selectivity against other gas components in the air. To solve this issue, I present a easy way that functionalize the pore channels through introducing CO_2-philic functional groups into the pore channels and introduce its importance and efficiency in changing 2D COFs into outstanding CO_2 capture and separation materials at low pressure and high temperature. I have developed a new mesoporous COF with good crystallinity, porosity and stability. The layered and open porous structure of COF material can be retained after loading amine source. Moreover, the amine functionalized COFs exhibited high CO_2 uptake capacity and CO_2/N_2 selectivities at low pressure and high temperature, which is useful for directly capturing CO_2 from flue gas. The present amino functionalized COFs method would generate a powerful way to construct 2D COFs for high-performance CO_2 storage and separation.

As described in these chapters, this thesis focuses on the design, synthesis, and functional exploration of a series of new COFs. Through the three-year work, the author unambiguously demonstrated the highly flexibility of COFs synthesis and showed new strategy for functionalizing COFs materials for CO_2 capture and separation. These novel COFs and functionalised COFs not only allow for the ordering of the building blocks into periodic layered structures, but also enable the functional design through introducing functional group into pore channels for highly selective CO_2 capture materials.

List of Publications

発表論文リスト

1. **Zhai. L. P**.; Huang. N.; Xu. H.; Chen. Q. H.; Jiang. D. A backbone design principle for covalent organic frameworks: the impact of weakly interacting units on CO_2 adsorption. *Chem. Commun*. **2017**, 53, 4242-4245.
2. Huang. N.; **Zhai. L. P.;** Xu. H.; Jiang. D. Stable Covalent Organic Frameworks for Exceptional Mercury Removal from Aqueous Solutions. *J. Am. Chem. Soc.* **2017**, 139(6), 2428. (Huang. N and **Zhai. L. P** contributed equally)
3. Huang. N.; **Zhai. L. P.**; Coupry. D. E.; Addicoat. M. A.; Okushita. K.; Nishimura. K.; Heine. T.; Jiang. D. Multiple-component covalent organic frameworks. *Nat. Commun.* **2016**, DOI: 10.1038/ncomms12325.
4. Chen. X.; Addicoat. M.; Jin. E. Q.; **Zhai. L. P.**; Xu. H.; Huang. N.; Guo. Z. Q.; Liu. L. L.; Irle. S.; Jiang. D. Locking Covalent Organic Frameworks with Hydrogen Bonds: General and Remarkable Effects on Crystalline Structure, Physical Properties, and Photochemical Activity. *J. Am. Chem. Soc.* **2015**, 137(9), 3241.

学会発表リスト

1. The international chemical congress of pacific basin societies 2015 (Pacifichem 2015)，December. **2015** Honolulu, Unite States. "*Functionalized 2D Covalent Organic Frameworks for Enhanced CO_2 Uptake*" (Poster presentation)
2. 9th Japan-China Joint Symposium on Functional Supramolecular Architecture, February. **2016** Okazaki, Japan. *"Covalent Organic Frameworks for Carbon Dioxide Capture"* (Poster presentation)
3. The 96th Annual Meeting of CSJ, Mar. **2016**, Kyoto, Japan. *"Covalent Organic Frameworks for Carbon Dioxide Uptake"* (Oral presentation)
4. The 97th Annual Meeting of CSJ, Mar. **2017**, Yokohama, Japan. *"Covalent Organic Frameworks for Carbon Dioxide Uptake"* (Oral presentation)
5. The 66th SPSJ International Polymer Conference, May. **2017**, Chiba, Japan *"Covalent Organic Frameworks for Carbon Dioxide Uptake"* (Oral presentation)

Acknowledgements

I would like to express my warmest gratitude to all those who helped me in the completion of this thesis and those who became a big part of my college life during the last three years at IMS.

Firstly, I would like to express deepest appreciation to my supervisors, Prof. Toshiyasu Suzuki and Prof. Donglin Jiang, for their productive advice, encouragement and kind help in the three years. From them, I saw the attributes of a great scientist, and learned a lot that can never be obtained in classrooms. I was extremely fortunate to get trained under their supervision. Their insight, attitude and enthusiasm have been a never-ending source of inspiration and support for me. Their encouragement and patience have made my time working here so enjoyable and comfortable, even in difficulties and failures. I know I can never repay them for what I have received, and I hope I can pass these qualities on when I have opportunities to help others.

The interdisciplinary work presented in this thesis would have not been possible without close collaborations and interactions with experts from various fields, and from different departments and universities. In particular, we collaborate very closely with Prof. Rajamani Krishna form University of Amsterdam, who simulates the properties of all the materials for carbon dioxide capture and separation presented in this thesis. I would like to give my thankfulness for this wonderful work. Moreover, Dr. Qiuhong Chen and Dr. Hong Xu in our group contributed significantly to my research efforts. It would be not possible to finish our research projects without their

insight on PXRD simulation.

The work in this thesis could not be done without the help from the people at the Instrument Center in IMS. I'm especially thankful to Dr. Motoyasu Fujiwara, Dr. Satoru Nakao, Ms. Midori Saito, Mr. Seiji Makita and Ms. Sayuri Suzuki and, for their kind helps in PXRD, FE-SEM, HR-TEM, EA and NMR measurements.

I also owe my sincere gratitude to my friends and my lab mates Dr. Qiuhong Chen, Dr. Ning Huang, Dr. Sasanka Dalapati, Dr. Hong Xu, Dr. Cheng Gu, Dr.Yang Wu, Dr. Enquan Jin, Miss. Shanshan Tao, Miss. Ping Wang, Mr. Qing Xu and our secretary Ms. Sayuri Suzuki and Ms. Watanabe Yoko, who gave me their help and encouragements in not only research but also everyday life.

I was fortunate to receive the financial supporting as research assistant from IMS for these three years.

Last but not least, I would like to thank my family, father, mother, brother, wife, son and my dear friends in china for all their love, supports and encouragements in my life.

Lipeng Zhai

June 21, 2017